

Experimental Characterization and Numerical Modelling of the Interfacial Heat Transfer Coefficient in Hot Stamping of Al-Si Coated 22MnB5 Steel

by

Arpan Raj Singh

A thesis
presented to the University of Waterloo
in fulfillment of the
thesis requirement for the degree of
Master of Applied Science
in
Mechanical and Mechatronics Engineering

Waterloo, Ontario, Canada, 2023

© Arpan Raj Singh 2023

Author's Declaration

This thesis consists of material all of which I authored or co-authored: see Statement of Contributions included in the thesis. This is a true copy of the thesis, including any required final revisions, as accepted by my examiners.

I understand that my thesis may be made electronically available to the public.

Statement of Contributions

The author acknowledges the contributions of others to the work done in this thesis as listed below:

1. Ryan George from the Forming and Crash Laboratory at the University of Waterloo provided the force output history from load cell tests found in Figure [3.9](#).

Abstract

In automotive hot stamping of Al-Si coated 22MnB5 steel, the heat transfer coefficient (HTC) between the blank and die is crucial for predicting the mechanical properties of the as-formed part. While average HTCs associated to a range of interfacial pressures are used in hot stamping operations design, in reality the HTC varies during quenching and depends on many other process parameters in addition to interfacial pressure. An improved understanding of the transient behavior of the HTC is the overarching focus here.

This work involves an experimental investigation to study the effects of pressure, coating weight, and surface roughness on the HTC evolution. Flat dies were mounted on a hydraulic press to obtain the temperature history within the blank and die. The data was analyzed using an inverse heat conduction algorithm to infer the time-resolved HTC. The HTC increases in two stages with the first being attributed to press tonnage ramp-up that gradually increases interfacial pressure. The second stage is attributed to an increase in the thermal conductivity and volume of the blank as its microstructure transforms from austenite to martensite. The experimental work also highlights how seemingly subtle aspects of this experiment, like the positioning and time-constant of the thermocouples, may impact the inferred HTC. Furthermore, nonuniformity of the interfacial pressure appears to lower the target pressure at which the HTC saturates, and diminish the time-averaged HTC with increasing target pressures.

This work also presents a physics-based model that explains and predicts the HTC evolution. The model simulates imperfect contact using the measured blank surface topography, an explicit finite difference scheme to solve the transient heat conduction, and a nonlinear mechanical submodel to solve the microscale displacement of the die due to uniaxial compression of surface asperities. The predicted HTC history is in fair agreement with the experimental result. The model suggests that the evolving thermal conductivity of 22MnB5 does not affect the HTC due to the shielding behavior of the resolidified Al-Fe-Si coating layer at the interface. The model also explains how all hot stamping process parameters influence the HTC and lays the groundwork for a unified model that captures the physics of the entire hot stamping process.

Acknowledgements

I would like to express my deepest gratitude to my supervisor and fellow Winnipegger, Dr. Kyle Daun. I remember being uncertain about what to do after undergrad, but that changed immediately once we connected. Thank you for the opportunity, encouragement, mentorship, and support over the past few years. I would also like to thank Dr. Cliff Butcher for giving me guidance on the solid mechanics aspect of my project, and Ardhendu for assisting me with some of my experiments. It was a pleasure working with you all, and I am so proud of how our journal paper turned out.

I would like to acknowledge the help provided by several individuals in our department: Dr. Michael Worswick for letting me use the equipment in the Crash and Forming Laboratory, Ryan George for operating the hydraulic press, Neil Griffet for troubleshooting instrumentation, and Eckhard Budziarek for helping with sample preparation.

I am so grateful for all the amazing members of the WatLIT research group: Nishant (always a pleasure geeking out about cars with you), Al (I appreciate the unique perspectives you passionately share with me; it has really opened my world view), Halil (thank you for bringing back peace when Al and I argue), Horace, Jun, Paule, Stephen, Fatima, Kaihsiang, Daniel, Tom, Cam, Michael, Kyu Min, Rodrigo, Stas, Sina, Matthias, and Ned. Being surrounded by such brilliant and kind peers was such an inspiration to me. It is unfortunate that COVID lockdowns limited the time we got to spend together, but I will cherish whatever time I got and will never forget our Friday night Teams activities. Congratulations to everyone who completed their degree, and I wish each of you a happy, healthy and prosperous life!

On a personal note, I would like to thank my friends for the good company in-person and online. To my housemates, Braeden, and Sai, thank you for all the interesting discussions in the kitchen, stick and puck sessions, and movie nights. To my friends from Winnipeg, thank you for staying connected with me during my time away from home. Some of my favorite memories were defending Hangar 6 with Frank, Henry, Jimmy, Matt, Joe, Aviskar, and Himesh in *WZone*, and surviving intense drops with Charle and Dabe in *Apex*. Along with Charle and Dabe, I would like to thank Gympson and John. The four of you are always ready to meet regardless of the time whenever I am visiting back home in Winnipeg and even came to visit me in Waterloo, so I cannot help but feel grateful to be able to call you guys my friends. I would also like to give my thanks to the Gartula Family for inviting me over on many occasions and making me feel at home. And a special shout out to fellow CHS² conference presenters, RJ and Pedram – I had a lot of fun exploring Sagrada Família and Camp Nou in Barcelona with you guys!

I would also like to thank my family for their blessings and support. Bivek and Pallavi, thank you for the great memories in Alberta and Manitoba. Ayush, I appreciate you for agreeing to watch all the random shows and movies I voted for during my visits back home. And thank you Mom and Dad (Mrs. Archana Singh and Dr. Purushottam Raj Singh) for all you have sacrificed. All my accomplishments are yours to celebrate.

Last but not least, I would like to thank Prasansa for being such a loving, supporting, and perfect partner. I wasn't quite sure what I was living for Until I Found Her ♡

Table of Contents

Author's Declaration	ii
Statement of Contributions	iii
Abstract	iv
Acknowledgements	v
List of Figures	x
List of Tables	xv
List of Abbreviations	xvi
List of Symbols	xvii
1 Introduction	1
1.1 Relevance of HTC in automotive hot stamping	1
1.2 Al-Si coated 22MnB5 steel	4
1.3 Review of experimental characterization of HTC	7
1.4 Review of HTC modelling	10
1.5 Research motivation and objectives	13
1.6 Overview of thesis	15

2	Experimental Methods	16
2.1	Measuring temperature during quenching	16
2.2	Inferring surface heat flux from temperature	20
2.3	Correcting measured temperatures	25
2.3.1	Experimental procedure for correcting the measured die subsurface temperature	25
2.3.2	Numerical procedure for correcting the measured blank temperature	28
2.4	Measuring surface roughness	29
3	Discussion of Experimental Results	33
3.1	Effect of thermocouple probe response delay	33
3.2	Effect of overestimating blank surface temperature	37
3.3	Effect of pressure on HTC	38
3.4	Effect of Al-Si coating on HTC	42
4	Description of Preliminary HTC Model	45
4.1	Computational domain	46
4.2	Heat transfer submodel	47
4.3	Mechanical submodel	51
5	Discussion of Model Predictions	54
5.1	Evaluation of model accuracy	54
5.2	Effect of intermetallic coating on HTC	57
5.3	Effect of martensite formation	61
5.4	Effect of hot stamping process parameters	62
6	Conclusions	67
6.1	Summary of thesis	67
6.2	Future work and recommendations	69
6.2.1	Improving experimental apparatus	69
6.2.2	Model development	70

References	72
APPENDICES	80
A Design of Experimental Apparatus	81
A.1 Die Features for Fastening on Large Macrodyne Press	81
A.2 Spring Lifter Slots on Lower Die	82
A.3 Determining Die Thickness via Finite Element Simulations	83
A.4 Finite Element Verification	87
A.5 Thermocouple Probe	87
A.6 Infrared Thermometer	92
B Derivation and Verification of Experimental Analyses	100
B.1 Deriving the Volterra Integral Equation of the First-Kind	100
B.2 Verifying Inverse Heat Conduction Analysis on the Die	101
B.3 Deriving Heat Flux Equation for a Thermally Lumped Blank	104
B.4 Verifying Energy Balance Analysis on the Blank	105
C Verification of HTC Model	108
C.1 Verification of heat transfer submodel	108
C.2 Verification of mechanical submodel	108

List of Figures

1.1	Typical hot stamped automotive components.	2
1.2	Schematic of direct hot stamping process.	2
1.3	A visualization of contact conductance between two rough surfaces and the resulting temperature field.	3
1.4	Continuous cooling transformation diagram for 22MnB5 steel.	5
1.5	Back-scattered SEM cross-sections showing the diffusion of solid Al-Fe-Si intermetallic layer over time.	6
1.6	Comparison of experimentally measured HTC for Al-Si coated and uncoated 22MnB5 steel blanks.	9
1.7	Comparison of surface heat flux histories between the blank and die under 1 MPa analyzed from temperature measurements of Chang et al. and Li et al.	10
1.8	Schematic of an abutting cylinder pair from which the conduction shape factor is derived for analytical HTC models.	11
1.9	CMY model adopted by Caron et al. compared against experimentally measured HTC for Al-Si coated 22MnB5 steel blanks.	13
2.1	Custom, industrial grade hydraulic press used for hot stamping experiments.	17
2.2	Schematic of flat dies and instrumentation.	18
2.3	Top and side view of Al-Si coated 22MnB5 blank.	19
2.4	IR thermometer verified for calibration against blackbody cavity and compared against welded thermocouple wire for air-quenched 22MnB5 coupon.	20
2.5	Temperature history of AS80-coated blank being quenched at a nominal interfacial pressure of 4.5 MPa.	21

2.6	Nomenclature for inverse analysis on the die modelled as a semi-infinite solid.	22
2.7	Modified quenching experiment for characterizing the time constant of the die subsurface temperature.	26
2.8	Heat flux leaving the blank (q_b'') and entering the die (q_d'') from the modified quenching experiment shown in Figure 2.7, where an oscillating force was applied manually on the blank.	26
2.9	Measured and calculated temperature histories for (a) 6-minute heated, AS150 blank quenched at 0.2 MPa and (b) 6-minute heated, AS80 blank quenched at 40 MPa. The two red circles in (a) highlight inflections in the blank temperature history as a result of martensite formation.	28
2.10	Low-density speckle pattern of a quenched blank measured by an optical profilometer.	30
2.11	Digital microscope measurement sites on an AS80 blank heated for 6 minutes then quenched at 40 MPa, where the circle beside the label “unpressed region” indicates the area on the blank that does not contact the upper die.	31
2.12	Convergence study for (a) magnification with 50 images in the vertical pitch, and (b) vertical pitch distance with magnification fixed to 3000x. The selected microscope settings are displayed in red.	32
3.1	Measured (T_{TC}) and corrected (T_D via Eq. (2.10) with $\tau = 0.15$ s) die subsurface temperatures for a 6-minute heated, AS80 blank quenched at 8 MPa.	34
3.2	Die surface heat flux histories obtained by deconvolving Eq. (2.1) for a 6-minute heated AS80 blank quenched at 8 MPa.	35
3.3	(a) Blank surface temperatures from Eq. (2.11) and (b) die surface temperatures from Eq. (2.1) for 6-minute heated, AS80 blank quenched at 8 MPa.	36
3.4	HTCs from Eq. (1.1) plotted against (a) quenching time and (b) blank temperature for a 6-minute heated, AS80 blank quenched at 8 MPa.	36
3.5	Blank temperatures from Eq. (2.11) along with their corresponding midplane-to-surface differences for a 6-minute heated, AS150 blank quenched at 8 MPa.	37
3.6	HTC from Eq. (1.1) plotted against blank temperature for a 6-minute heated, AS150 blank quenched at 8 MPa.	38

3.7	[(a), (c), (e)] HTC plotted against blank temperature and [(b), (d), (f)] time-averaged HTCs before the blank reaches 400°C for [(a), (b)] AS80/6-minute heated blank, [(c), (d)] AS80/12-minute heated blank, and [(e), (f)] AS150/6-minute heated blank.	40
3.8	(a) Pressure-sensitive film (sensitive from 10 to 50 MPa) placed on lower die and (b) von Mises stress contour of die surface from complementary FE simulation.	41
3.9	Ex-situ press output histories measured by load cells.	41
3.10	S_a of (a) AS80/6-minute heated blanks, (b) AS80/12-minuted heated blanks, and (c) AS150/6-minuted heated blanks. Each bar and vertical line represents average and max/min values of S_a from the nine surface patches shown in Figure 2.11. Dashed lines represent average height of the bars.	43
3.11	Typical micrographs in the unpressed regions of (a) AS150-coated blank heated for 6 minutes, and (b) AS80-coated blank heated for 6 minutes.	44
4.1	Schematic of three-dimensional computational domain.	46
4.2	Comparison of (a) raw and (b) down-sampled blank surface topography, in which the latter is used in the model.	47
4.3	Schematic of three-dimensional computational domain.	50
4.4	Procedure of transitioning from a three-dimensional (3D) conduction analysis to a one-dimensional (1D) conduction analysis in the blank.	50
4.5	Extrapolated surface temperatures from polynomial curve fits of the predicted temperature distribution.	51
4.6	Comparison of true stress-true strain curves for a strain rate of 0.1 s ⁻¹ between isothermal compression tests and curve fits via Norton-Hoff constitutive law.	52
5.1	Comparison of model predicted and experimentally measured (a) blank surface temperature history and (b) HTC history for a 0.825 mm half-thick blank quenched at 4.5 MPa.	55

5.2	Comparison of model predicted and experimentally measured time-averaged HTCs between blank temperatures of 750°C and 400°C for AS80 blanks. Pressure ramp up durations of 0, 0.125, 0.125, 0.17, 0.7, and 0.8 s were specified in the model for the nominal pressures labelled from left to right, and the durations were based on the time it takes the press load to stabilize in Figure 3.9.	56
5.3	(a) Model predicted HTC histories for coated (intermetallic coating) and uncoated (bare 22MnB5) blank surfaces and (b) thermal conductivity evolution of FeAl and 22MnB5 during quenching.	58
5.4	Comparison of model predicted HTC evolution for two different surface topographies measured from the same blank.	59
5.5	Histogram of surface deviations from the mean plane in the unpressed intermetallic coating (i.e., austenitized AS150-coated 22MnB5) and corresponding schematic of surface profile.	60
5.6	Effect of specific heat capacity and latent heat release during martensite formation on (a) the HTC and (b) blank surface temperature history ($L_b = 0.825$ mm, $p = 4.5$ MPa).	62
5.7	Effect of (a) increasing thermal conductivity and (b) thickness of 22MnB5 from martensite formation on the HTC ($L_b = 0.825$ mm, $p = 4.5$ MPa).	63
5.8	(a) Effect of press tonnage ramp up duration on predicted HTC history and (b) true stress vs true strain of uniaxially compressed 22MnB5 at the end of ramp up phase for the two compared cases.	64
5.9	(a) Effect of blank half-thickness (L_b) on predicted HTC history and (b) deformation history of the maximum element height (H_{max}) for the two compared cases.	65
5.10	Effect of (a) initial blank temperature and (b) initial die temperature on predicted HTC history.	66
6.1	(a) Experimental apparatus for inferring transient HTC between two medium carbon steel specimens and (b) temperature field at the interface measured by the IR camera.	70
A.1	View of upper die from perspective of blank and shoulder screw (McMaster-Carr M10×1.5×90 91290A546) used to secure dies to aluminum cooling plate.	82

A.2	(a) View of lower die from perspective of blank and (b) spring lifter assembly.	83
A.3	Domain of blank (grey) and die (green).	84
A.4	Mesh used for thermal FE simulations.	85
A.5	Contact modelling between the blank and die.	86
A.6	Temperature field of die at (a) $t = 0$ s and (b) $t = 20$ s.	87
A.7	Lifting ring for manually handling dies.	88
A.8	(a) FE predicted surface heat flux compared to measurements by Caron et al. and (b) FE predicted surface temperatures compared to measurements by Hu et al.	89
A.9	Section view of lower die showing arrangement and mounting of thermocouple probe via compression fittings (arrangement mirrored in the upper die).	90
A.10	Section view of upper die showing mounting of IR thermometer tip.	94
B.1	FE domain of blank and die in contact with each other.	102
B.2	Die subsurface temperature ($D = 1.5$ mm below quenching surface) predicted by FE analysis, in addition to the contaminated dataset.	103
B.3	Comparison between FE and inverse heat conduction analysis of (a) HTC and (b) die surface temperature.	103
B.4	Average blank temperature predicted by the FE model when the surface heat flux is a constant value of 0.5 MW/m^2 .	106
B.5	Comparison between FE input and energy balance estimate (Eq. (B.21)) of heat flux leaving one surface of the blank.	107
C.1	Comparison of maximum blank temperature predicted by the present and FE model for perfect contact.	109
C.2	(a) Initial condition of mechanical verification problem, and (b) comparison of predicted deformation history from present and FE model.	110

List of Tables

1.1	Alloying element composition (wt.%) and mechanical properties of 22MnB5.	4
2.1	Thermophysical properties of die and blank (T in °C).	24
2.2	Summary of time constants for various thermocouple probes.	27
4.1	Thermophysical properties of FeAl (40 at.% Al) used to model Al-Fe-Si intermetallic.	48
4.2	Statistically determined Norton-Hoff model parameters for 22MnB5.	52
5.1	CMY model parameters used by Caron et al. along with recommended settings.	60
5.2	Reference case for studying effects of martensite formation on the HTC.	61
5.3	Base case definition for the parametric study using the HTC model.	63
A.1	Thermocouple probe specifications.	91
A.2	Compression fitting specifications.	92
A.3	IR thermometer and ceramic tip specifications.	93

List of Abbreviations

1D	One-dimensional
22MnB5	A particular grade of boron-manganese steel
3D	Three-dimensional
Al-Si	Aluminum-silicon
APDL	ANSYS Parametric Design Language
AS80	Aluminum-silicon coating weight of 80 g/m ²
AS150	Aluminum-silicon coating weight of 150 g/m ²
BCT	Body-centered tetragonal
CMY	Cooper-Mikić-Yovanovich analytical model
FE	Finite element
FCC	Face-centered cubic
GD&T	Geometric dimensioning and tolerancing
HSLA	High-strength low alloy
HTC	Interfacial heat transfer coefficient
IR	Infrared
NPT	National pipe thread
RMS	Root mean square
SEM	Scanning electron microscope

List of Symbols

a	Material strength constant in Norton-Hoff law [MPa s ^m]
A	Cross-sectional area of element representing asperity [m ²]
A_a	Apparent contact area [m ²]
A_r	Real contact area [m ²]
Ac_1	Austenitization onset temperature (non-isothermal heating) [°C]
Ac_3	Austenitization completion temperature (non-isothermal heating) [°C]
α	Thermal diffusivity [m ² /s]
β	Material strength constant in Norton-Hoff law [K]
c_b	Specific heat capacity of 22MnB5 blank [J/(kg K)]
c_d	Specific heat capacity of AISI 4140 tool steel die [J/(kg K)]
c_p	Specific heat capacity [J/(kg K)]
D	Thermocouple depth position relative to die surface [mm]
ϵ	True strain
$\dot{\epsilon}$	Rate of true strain [s ⁻¹]
f_m	Martensite phase fraction
F	Applied force [N]
Δh_m	Latent heat of martensite formation of 22MnB5 [J/kg]
H	Height of asperity in the HTC model [μm]
H_{\max}	Height of tallest asperity in the HTC model [μm]
HV	Surface hardness [MPa]
i	Time step counter
k	Thermal conductivity [W/(m K)]
k_b	Thermal conductivity of 22MnB5 blank [W/(m K)]
k_d	Thermal conductivity of AISI 4140 tool steel die [W/(m K)]
k_m	Harmonic mean thermal conductivity of two materials [W/(m K)]
L_b	Half-thickness of blank [m]

L_x	Micrograph dimensions in the x direction [μm]
L_y	Micrograph dimensions in the y direction [μm]
m	Strain hardening exponent in Norton-Hoff law
M_f	Finishing temperature of martensite formation [$^{\circ}\text{C}$]
M_s	Starting temperature of martensite formation [$^{\circ}\text{C}$]
ω	Conduction shape factor
n	Strain hardening exponent in Norton-Hoff law
N	Number of contact spots
$N_{b,z}$	Number of nodes/elements in the blank across the z direction
p	Interfacial pressure [MPa]
ψ	Heuristic press controller latency factor ($0 \leq \psi \leq 1$)
ϕ	Sensitivity of measured temperature to imposed heat flux [$(^{\circ}\text{C m}^2)/\text{W}$]
q	Heat transfer rate [W]
q''	Heat flux [W/m^2]
q''_b	Heat flux leaving the blank [W/m^2]
q''_d	Heat flux leaving the die [W/m^2]
r_1	Radius of circular contact spot in analytical HTC models [m]
r_2	Radius of abutting cylinders in analytical HTC models [m]
R_a	Arithmetic roughness average about the mean line [μm]
R_q	Standard deviation of the surface profile heights [μm]
ρ	Density [kg/m^3]
ρ_b	Density of 22MnB5 blank [kg/m^3]
ρ_d	Density of AISI 4140 tool steel die [kg/m^3]
S_a	Arithmetic roughness average about the mean plane [μm]
σ	True stress [MPa]
t	Time [s]
Δt	Time step size [s]
T	Temperature [$^{\circ}\text{C}$]
T_{abs}	Absolute temperature [K]
T_b	Blank surface temperature [$^{\circ}\text{C}$]
T_d	Die surface temperature [$^{\circ}\text{C}$]
T_D	Actual die subsurface temperature (corrected from T_{TC}) [$^{\circ}\text{C}$]
T_i	Initial die temperature [$^{\circ}\text{C}$]
T_{TC}	Measured die subsurface temperature [$^{\circ}\text{C}$]
ΔT_c	Temperature jump across blank-die contact interface ($\Delta T_c = T_b - T_d$) [K]
τ	Thermal time constant of die subsurface thermocouple probe [s]
θ	Absolute mean angle of the surface profile [rad]

Δx	Nodal spacing in the x direction of HTC model [μm]
Δy	Nodal spacing in the y direction of HTC model [μm]
Δz	Nodal spacing in the z direction of HTC model [μm]
z	Surface height [μm]
\bar{z}	Mean surface height [μm]
Δz_{blank}	Blank nodal spacing in the z direction
Δz_{die}	Die nodal spacing in the z direction

Chapter 1

Introduction

This chapter provides an overview of automotive hot stamping and the widely used 22MnB5 steel protected with an aluminum-silicon (Al-Si) coating. Experimental and theoretical investigations of the interfacial heat transfer coefficient (HTC) that is critical to hot stamping design are reviewed. An outline of the thesis is given at the end of this chapter.

1.1 Relevance of HTC in automotive hot stamping

With vehicle production rates approaching 100 million per year amid a global climate crisis [1], stricter laws are being imposed to enhance fuel efficiency and reduce CO₂ emissions. In response, automotive manufacturers are transitioning from cold forming to the direct hot stamping of press hardenable steel to produce lightweight body-in-white components [2]. Hot stamping reduces weight by improving the strength-to-weight ratio of as-formed parts, while enhancing formability, maintaining production flow, and improving vehicle crashworthiness [3]. From its inception in lawn mower blade production in the 1970's [4], hot stamping made its debut in automotive manufacturing in 1984 for the side impact door beams of the Saab 9000 passenger sedan [5]. Recent examples of hot stamped parts can be seen in Figure 1.1, which amounted to about 300 million parts in 2015 and more than 500 million parts in 2018 [6].

Referring to Figure 1.2, the direct hot stamping process typically begins by uniformly austenitizing a 22MnB5 steel blank in a roller hearth furnace at approximately 950°C for 5 minutes [7]. A robot then quickly transfers the blank to a press fitted with a pair of water-cooled forming tools (e.g., die and punch) [8], within which the blank is formed into the

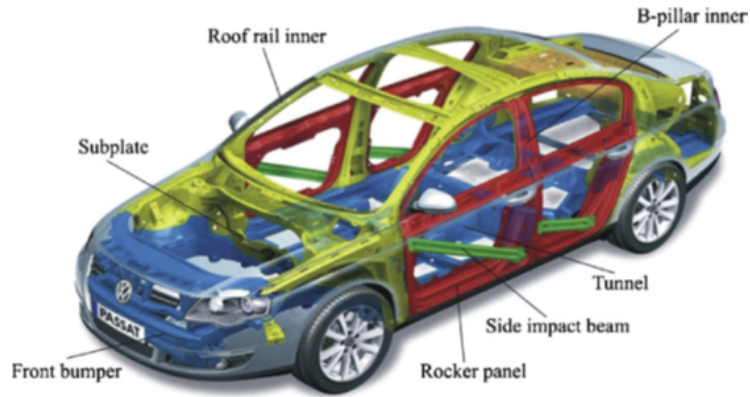


Figure 1.1: Typical hot stamped automotive components [4].

desired shape and quenched simultaneously. The improved formability of austenitic blanks reduces tool wear, and prevents spring back and fracture within the final part, allowing geometrically-complex parts to be formed [9]. The alternative to direct hot stamping is indirect hot stamping, which adds a cold forming step prior to austenitization to bring the shape of the blank near its final specification. In pursuit of cutting costs, indirect hot stamping is not as prevalent in the automotive industry [10]. Therefore, this thesis focuses on direct hot stamping.

If the quenching rate during forming is maintained above the critical value of $27^{\circ}\text{C}/\text{s}$ for 22MnB5 blanks, the austenitic microstructure transforms into martensite, offering a very high ultimate tensile strength of 1500 MPa and microhardness on the order of 470 HV₁₀ [7]. This fully martensitic steel is ideal for downgauging the thickness of anti-intrusion

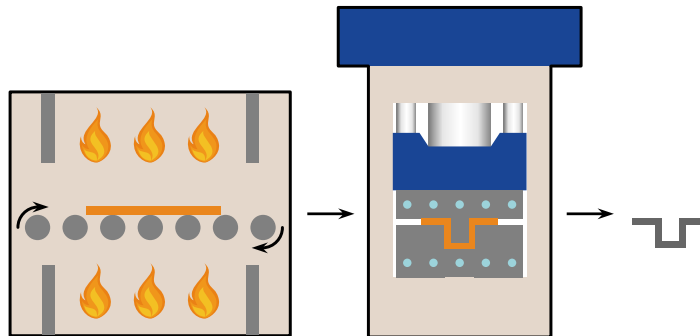


Figure 1.2: Schematic of direct hot stamping process.

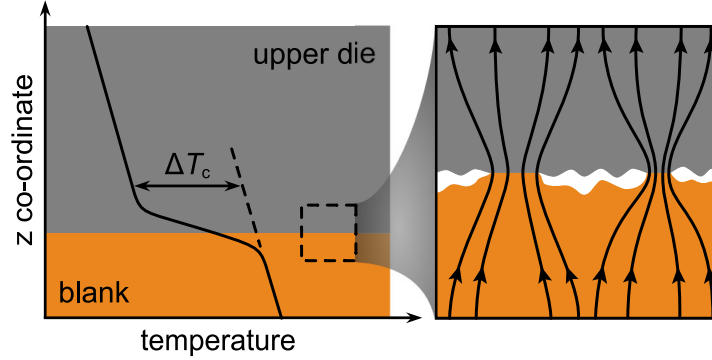


Figure 1.3: A visualization of contact conductance between two rough surfaces and the resulting temperature field.

components that make up the passenger safety cell to reduce vehicle weight. In components designed for crash energy absorption such as the rear rails and the lower B-pillar section [11], regions of lower strength and higher ductility may be realized by maintaining the quenching rate below $27^\circ\text{C}/\text{s}$.

The quenching rate of the blank depends on the initial blank and die temperatures, as well as the HTC between the blank and die, defined from Newton's Law of Cooling as

$$\text{HTC}(t) = \frac{q''(t)}{T_b(t) - T_d(t)} \quad (1.1)$$

where q'' is the surface heat flux, t is the time, and T_b and T_d are the blank and die surface temperatures, respectively. The HTC is a measure of contact conductance that depends on the thermal conductivities and imperfect thermal contact due to the microscale topology of the conforming surfaces. As shown in Figure 1.3, the interfacial heat transfer is primarily due to conduction through pairs of microasperities connecting the two surfaces. Increasing the interfacial pressure increases the HTC because the number of contact spots and real contact area increase as the microasperities of the blank deform. Linking the interfacial pressure and HTC is of primary interest among hot stamping practitioners because finite element (FE) simulations of hot stamping, which depend on accurate HTC data, are often used to determine process parameters like interfacial pressure that produce the desired quenching rate and as-formed mechanical properties [4, 12, 13].

Table 1.1: Alloying element composition (wt.%) and mechanical properties of 22MnB5 [7, 14].

		NOMINAL MECHANICAL PROPERTIES	
C	0.23	As-received 22MnB5	
Si	0.22		
Mn	1.18	Yield strength	505 MPa
Cr	0.16	Ultimate tensile strength	637 MPa
Ni	0.12	Microhardness	214 HV ₁₀
		Fully martensitic 22MnB5	
Ti	0.040	Yield strength	1000 MPa
B	0.002	Ultimate tensile strength	1500 MPa
N	0.005	Microhardness	470 HV ₁₀

1.2 Al-Si coated 22MnB5 steel

The 22MnB5 grade of steel equipped with an Al-Si coating was developed in the late 1990's by ArcelorMittal (a French steel manufacturer formally known as Usinor) and was first adopted in the early 2000's by Citroën and Renault [6]. While zinc-based coatings have also been developed, the Al-Si coated 22MnB5 steel is currently the dominant variant in automotive hot stamping across the world [4], and is therefore the subject of this thesis.

As-received 22MnB5 has ferritic (75%) and pearlitic (25%) microstructures, resulting in nominal yield and ultimate tensile strengths of 505 and 637 MPa, and microhardness on the order of 214 HV₁₀ [14]. Along with carbon atoms, 22MnB5 contains boron and manganese to promote hardenability during hot stamping. Boron influences hardenability by slowing down the conversion of austenite into softer microstructures, promoting the formation of martensite at lower quenching rates. In addition to improving hardenability, manganese lowers the austenitizing end temperature (A_{c3}), thus reducing production costs [3]. Table 1.1 summarizes the alloying element composition and strength of as-received and martensitic 22MnB5.

The transformation of austenite to martensite is an exothermic process that starts once the blank cools to 400°C (M_s), and gradually continues until the temperature reaches 250°C (M_f). As shown in the continuous cooling transformation diagram in Figure 1.4, complete formation of martensite is guaranteed if the quenching rate is maintained above 27°C/s

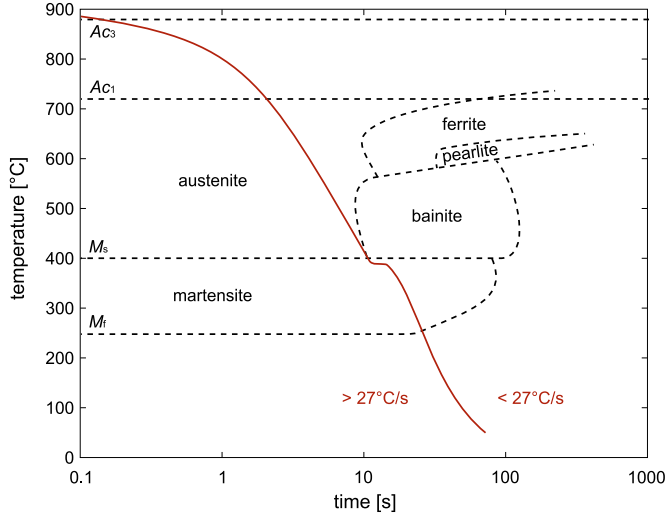


Figure 1.4: Continuous cooling transformation diagram for 22MnB5 steel [14].

prior to the blank reaching M_s because rapid quenching eliminates the time that is required for carbon atoms to diffuse out of their interstitial position [15]. In this diffusionless transformation, the face-centered cubic (FCC) lattice of austenite is converted into the body-centered tetragonal (BCT) lattice of martensite [4], which leads to an overall volume increase of 2% [16] and the release of 135 kJ/kg of latent heat [17]. However, if the quenching rate falls below 27°C/s prior to M_s , softer phases like bainite, pearlite, and ferrite form instead of martensite due to carbon diffusion. This results in a component with less strength, but improved ductility. With such knowledge, it is possible to mechanically tailor a component by adjusting the local quenching rate throughout the geometry. This is achieved in practice by controlling the local temperature of the tool surface and the gap size between the blank and tool surface [18].

Prior to austenitization, an Al-Si coating of 88 wt.% aluminum, 9 wt.% silicon, and 3 wt.% iron is applied to the surface of the 22MnB5 steel blank using a hot dipping process [19]. At room temperature, the newly applied coating contains silicon aggregates within the aluminum matrix near the surface, while the interface between the coating and steel substrate is made up of an Al-Fe-Si system [20]. The coating prevents the blank from oxidizing and decarburizing in the roller hearth furnace, which occurs if the bare metal surface is exposed to air at high temperatures. Preventing oxidation prolongs tool life by reducing friction and wear [21]. The coating also provides the blank with long-term corrosion resistance [22], and prevents surface contamination after hot stamping such that

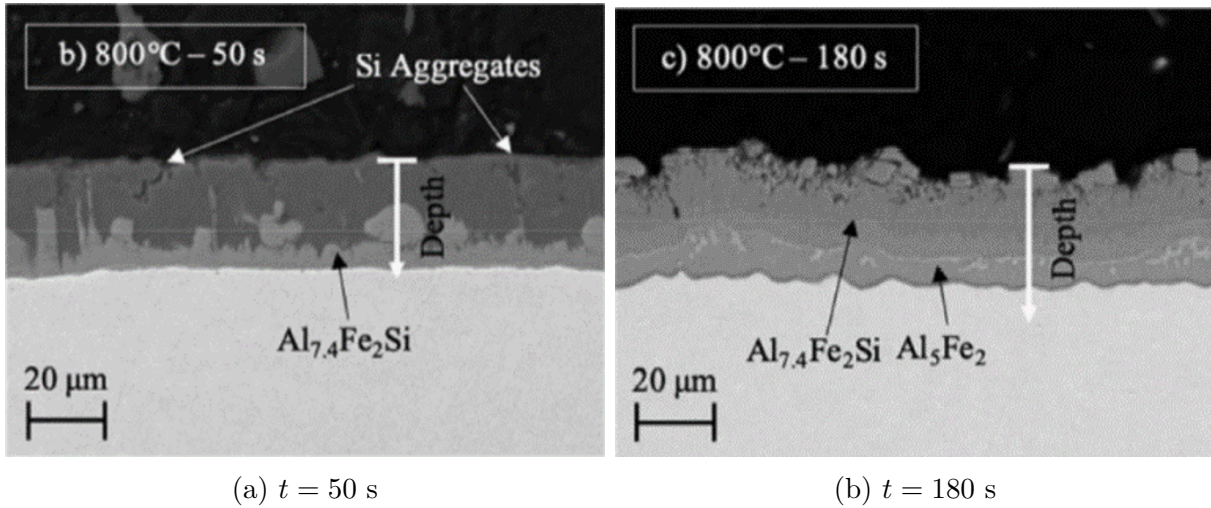


Figure 1.5: Back-scattered SEM cross-sections showing the diffusion of solid Al-Fe-Si intermetallic layer over time [24].

shot blasting is unnecessary [23].

The complex evolution of Al-Si coating during austenitization must be understood to control its formability and the formed part's weldability. Moreover, the coating phase must be related to furnace process parameters because coating liquification shortens the lifespan of ceramic rollers and disrupts the furnace-to-press transfer [24]. Coating evolution also controls the blank's radiative properties, which must be known to model the heating process [25, 26].

The Al-Si coating initially melts at about 577°C, regardless of the heating rate, and is followed by a second melting reaction that depends on the furnace set-point temperature [24]. The higher austenitizing temperatures allow the iron from the 22MnB5 steel to continuously diffuse into the liquefied coating. This leads to the formation of Al-Fe-Si intermetallic layers (e.g., $\text{Al}_{7.4}\text{Fe}_2\text{Si}$ and $\text{Al}_2\text{Fe}_3\text{Si}_3$) that solidify due to their higher melting temperature, and gradually build their way up to the surface. Once the 22MnB5 steel reaches austenitization temperatures, the coating consists of layers of alternating weight fractions of Al and Fe [20]. The development of the intermetallic multi-layers is shown by the back-scattered scanning electron microscope (SEM) images in Figure 1.5.

The Al-Si coating may be responsible for two competing phenomena that affect the HTC. According to experiments, thinner coatings, oils, and lubricants generally result in higher HTCs because of their lower thermal resistance for conduction [16]. On the

other hand, thinner Al-Si coatings lead to increased surface roughness after austenitization because of the shorter distance for the Al-Fe-Si intermetallic layers to diffuse from the iron substrate to the surface [27], which may result in lower HTC. The diffusion of intermetallic layers is also related to the furnace dwell time, where a novel in-situ roughness analysis showed that longer dwell times allow more diffusion, which leads to a rougher surface [27]. Therefore, it is important to characterize the effect of the Al-Si coating thickness and furnace dwell time on the HTC.

1.3 Review of experimental characterization of HTC

While hot stamping experiments have focused primarily on characterizing the HTC as a function of interfacial pressure, many have also examined the influence of other process parameters and experimental artefacts. Chang et al. [16], Hamasaiid et al. [28], and Liu et al. [29] studied the effect of lubricants like oil, graphite, and TiO₂-based coatings, and observed that increased coating thicknesses generally decrease the HTC. Caron et al. [30], Merklein et al. [31] and Omer et al. [32] attached cartridge heaters on the dies and found that elevated die temperatures lead to larger HTCs. Abdulhay et al. [17, 33, 34] studied thermal contact resistance in hot stamping of B-pillers (parts with “Ω”-shaped cross-sections), and found that local HTCs at the vertical interfaces were up to three times smaller compared to HTCs at the horizontal interfaces due to thinning in the sidewalls and loss of contact with the die [17]. The effect of air gaps on the HTC was also studied by Salomonsson and Oldenburg [35]. Parts that are formed into non-planar geometries also experience complex tribological behaviors at the interface due to relative motion between the blank and die/punch [36], leading to additional artefacts in the measured HTC.

In obtaining the HTC via Eq. (1.1), measuring the blank and die surface temperatures (i.e., T_b and T_d) at the interface is virtually impossible due to inadequate space for the measuring sensor (e.g., a thermocouple), and a probe located at the interface will inevitably perturb the HTC. Instead, sensors are typically inserted within the blank and die, but at some distance from the interface. Models are then applied to relate these subsurface measurements to the quantities in Eq. (1.1).

Various methods have been used to characterize the HTC from experimentally measured temperature, including inverse heat conduction analysis [16, 17, 30, 37, 38], calorimetry [7, 32, 39, 40, 41], or inverse FE analysis [21, 23, 42, 43, 44]. The FE method uses nonlinear regression to identify the HTC that produces the best agreement between modelled and measured blank temperature histories. A major drawback of this approach is that the HTC must be modelled as time-invariant, which is far from the case due to the progressive

flattening of the microasperities with quenching time. In calorimetry, the time-resolved HTC is calculated from balancing the heat leaving the blank to its change in sensible energy over a finite time step. This calculation requires the interfacial temperatures of the blank and die; while the blank may be modelled as thermally lumped, the die surface temperature must be measured from sensors installed either below the surface [40], or on the surface that is made accessible by cutting a slot in the blank [32]. Both scenarios introduce a positioning error in the temperature, and consequently an error in the inferred HTC. The shortcomings of inverse FE analysis and calorimetry are absent in inverse heat conduction analysis, which is used in the present study [45, 46].

In the inverse heat conduction technique, the blank is usually modelled as thermally-lumped, meaning that, e.g., a temperature measured using a thermocouple at the blank midplane is taken to be the same as the blank surface temperature at any instant [16, 38, 45], while the die temperature at a defined depth and time is taken to be that indicated by the subsurface thermocouple. However, the process of inferring the HTC is mathematically ill-posed, so seemingly small errors introduced by modelling assumptions may lead to significant errors in the recovered HTC. For example, the thermocouple hole within the die may produce a thermal shadowing effect [47], while the finite thermal contact between the thermocouple and the die becomes important given the rapid variation of temperature during the hot stamping process.

A further question concerns the interfacial pressure, which, as highlighted above, plays a key role in the HTC through the deformation of the microasperities during forming. As shown in Figure 1.6, there is little consensus in the literature on how the HTC varies with interfacial pressure for 22MnB5 steel. This has been attributed in part to the variety of temperature measurement and analysis methods used to infer the HTC [45], uncertainty in the true interfacial pressure [48], and variations in the interfacial condition between experiments. In terms of the interfacial condition, some studies have characterized the HTC for uncoated blanks [16, 40], while others have tested blanks with Al-Si coating [30, 32, 38] or oil lubrication [16]. Another example is variation in surface roughness, where some experiments have been performed by grinding the surface of both the blank and die to a roughness average of only 0.2 μm [40], while most retain the as-received surface condition of the blank and opt for a ground finish for the die surface. Moreover, some studies report HTCs averaged from the transient regime [7], while others report steady state values [17], which tend to be larger. Consequently, the state-of-knowledge of the HTC is mostly empirical in nature with little insight into how it evolves with time under a given nominal pressure. This uncertainty represents a major impediment in the hot stamping of complex geometries where the interfacial pressure and resultant mechanical properties can significantly vary over the as-formed part.

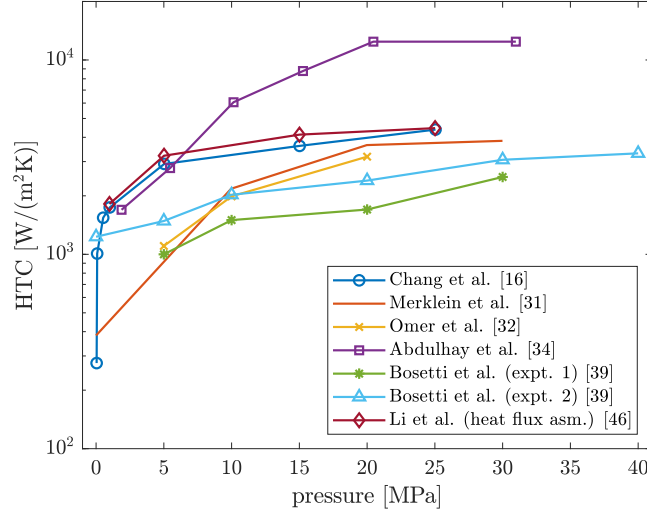


Figure 1.6: Comparison of experimentally measured HTC's for Al-Si coated [31, 32, 34, 39] and uncoated [16, 46] 22MnB5 steel blanks.

In lieu of verifying and improving the accuracy of the inferred HTC, one approach for assessing the reliability of measured temperatures is to compare the surface heat flux histories of the blank and die derived from their respective subsurface temperature since energy conservation demands the two heat flux histories to be equivalent [30]. This procedure is exemplified using data reported in hot stamping experiments by Chang et al. [16] and Li et al. [46], and the resulting surface heat flux histories are compared in Figure 1.7. In the case of the data from Chang et al. [16], the heat flux leaving the blank and entering the die were temporally aligned with similar magnitudes, albeit with a discrepancy at 4 s. Li et al.'s measurements [46], in contrast, show the heat flux entering the die was temporally delayed and initially smaller than the heat flux leaving the blank, revealing a potential delayed response with the measured die subsurface temperature and an error in the inferred HTC.

The process of comparing surface heat flux exchange between the blank and die in confirming satisfaction of the first law of thermodynamics is an easy way to verify the measured temperatures, and is used in the present experiment. However, it is worth noting that this technique does not verify the actual magnitude of the derived heat flux since a comparison is being drawn between two experimentally derived quantities. For example, even if the blank surface and die surface heat fluxes appear identical (satisfying first law), the thermocouples in the blank and die may both be experiencing a delayed response.

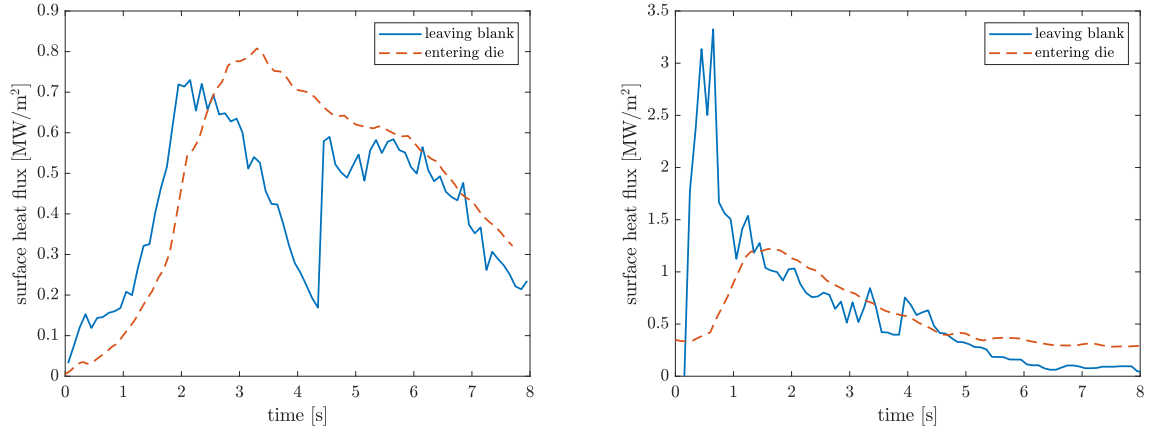


Figure 1.7: Comparison of surface heat flux histories between the blank and die under 1 MPa analyzed from temperature measurements of (a) Chang et al. [16] and (b) Li et al. [46].

1.4 Review of HTC modelling

Given how important the HTC is for relating process parameters with quenching rate, studies have primarily utilized hot stamping experiments to characterize the HTC for a wide range of interfacial pressures, blank and die temperatures, and interfacial materials (e.g., die lubricants). However, because of the coupled effects of thermal, mechanical, and metallurgical properties of the blank, very few of these studies have undertaken to explain experimentally characterized HTCs using physics-based models.

Nevertheless, general-use analytical models for predicting heat flow across a rough interface have been developed over the past century [49, 50]. While development was mainly motivated by applications in aerospace, nuclear, and microelectronics industries [49, 51], these models are generally applicable for predicting the HTC in many scenarios. As shown in Figure 1.8, most analytical models are derived from the conduction shape factor for a single-contact spot of radius r_1 between two abutting cylinders of radii r_2 where the annulus surrounding the contact spot is modelled as adiabatic [51, 52, 53]. If there are N uniformly distributed contact spots, each with an average radius of \bar{r}_1 , then the steady state HTC is given by

$$\text{HTC} = 2k_m \frac{\sum_N \bar{r}_1}{A_a \omega} \quad (1.2)$$

Here, A_a is the apparent contact area, ω is the conduction shape factor that depends on

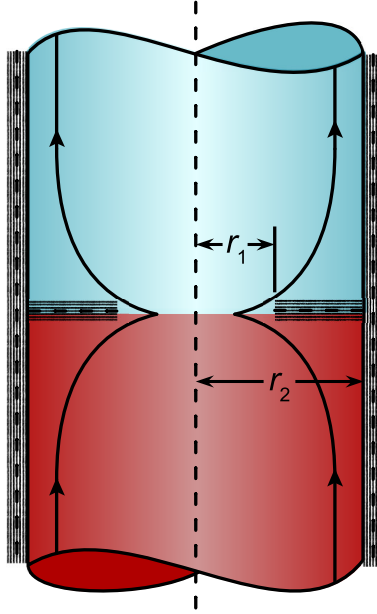


Figure 1.8: Schematic of an abutting cylinder pair from which the conduction shape factor is derived for analytical HTC models.

r_1/r_2 , and k_m is the harmonic mean thermal conductivity of the material pair defined as

$$k_m = \left(\frac{1}{k_1} + \frac{1}{k_2} \right)^{-1} \quad (1.3)$$

The effect of interfacial pressure (p) and surface hardness (HV) on the HTC are derived from a static force balance. Assuming pure plasticity as done by Cooper et al. [51], the applied force ($p \cdot A_a$) is equal to the reaction force of the softer material ($HV \cdot A_r$), where A_r is the real contact area. Rearranging the static force balance leads to

$$\frac{p}{HV} = \frac{A_r}{A_a} \quad (1.4)$$

Eqs. (1.2) and (1.4) are linked by an empirical surface profile analysis for a single surface with Gaussian height distribution. For the interface between a flat surface and a rough surface, Cooper et al. [51] propose the Cooper-Mikić-Yovanovich (CMY) model

$$\text{HTC} = 1.45k_m \frac{|\tan \theta|}{R_q} \left(\frac{p}{HV} \right)^{0.985} \quad (1.5)$$

where $|\tan \theta|$ is the absolute mean slope of the rough surface profile, and R_q is the standard deviation of the rough surface profile heights. If both conforming surfaces are rough, their effective values $\theta = \sqrt{\theta_1^2 + \theta_2^2}$ and $R_q = \sqrt{R_{q,1}^2 + R_{q,2}^2}$ may be used. Like other analytical models, Eq. (1.5) clearly illustrates how the thermal, mechanical, and roughness parameters influence the HTC, and is easier to implement and computationally inexpensive compared to numerical simulations.

Caron et al. [30] adopted the CMY model to estimate the HTC between an Al-Si coated 22MnB5 blank and AISI 4140 tool steel die during the quenching phase of hot stamping. The interface of the as-received blank and die was characterized by their effective surface roughness ($\theta = 0.059$ rad, $R_q = 1.18$ μm). The surface hardness was set to 400 HV ($HV = 3.922$ GPa), which was measured from a pre-austenitized blank at 600°C. The harmonic mean thermal conductivity of 22MnB5 at 400°C and AISI 4140 tool steel was calculated as $k_m = 29.9$ W/(m K). The model predicted HTCs were uniformly inflated by 4,960 W/(m² K) for all interfacial pressures to account for interstitial convection. However, as shown in Figure 1.9, recent hot stamping experiments reveal that the CMY model seemingly over-predicts the HTC. Moreover, the predicted HTC does not become insensitive to pressure at higher interfacial pressures as observed in experiments. While experimentally determined HTCs have been accounted for to adjust the magnitudes [54, 55, 56], analytical models are still limited to predicting a single HTC value as opposed to the evolving characteristics that are necessary for accurate FE simulations of the hot stamping process.

Recent development for predicting contact conductance has mainly revolved around numerical simulations; these techniques can capture the full effect of three-dimensional heat conduction in both sides of the contact interface, whereas analytical models assume two-dimensional heat conduction near the contact interface, and one-dimensional heat conduction further away (see adiabats in Figure 1.8). Numerical simulations can also model non-isotropic rough surfaces directly measured from optical profilometry and can capture deformation of microasperities of both surfaces independently to further improve accuracy [57]. These benefits, however, come at the expense of computational time and cumbersome setup.

The HTC between two aluminum microscale columns was predicted numerically by Murashov and Panin [58] using commercial FE software. High-fidelity surface models were used to capture the roughness of both contacting surfaces. For a given pressure, the deformed contact region was determined by a mechanical submodel that considered work hardening, surface layer hardening due to asperity interaction, and indentation size effect. Then, a steady-state thermal submodel was invoked to solve the three-dimensional thermal field within the columns. The HTCs were derived from the predicted temperature profile

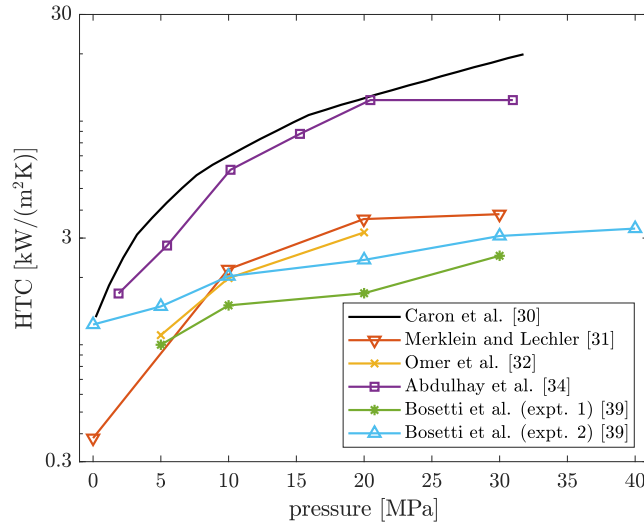


Figure 1.9: CMY [51] model adopted by Caron et al. [30] compared against experimentally measured HTC for Al-Si coated 22MnB5 steel blanks.

and agreed with Shlykov’s analytical model [56] for pressures less than 3 MPa, which is the maximum pressure that maintains one asperity pair in contact. The numerical model predicted higher HTCs than the analytical model as the contact pair count exceeded beyond one at higher pressures.

A similar scheme was developed by Frekers et al. [57] and later adapted by Vu et al. [59] to predict the steady state HTC in non-isothermal glass molding process. The mold surface was modelled to deform elasto-plastically, while the plasticity component was neglected for the glass. At medium pressures, the model predictions agreed with HTCs inferred from glass molding experiments using infrared thermography. Discrepancies in the predicted HTC at higher pressures were attributed to underlying assumptions within the mechanical submodel.

1.5 Research motivation and objectives

In the case of hot stamping, neither analytical nor numerical modelling has been used to explain the transient behavior of the HTC during the forming process. Such a model would be invaluable given the increasing complexity of part geometries and growing range of coating weights available to manufacturers. Instead, existing models have primarily focused

on predicting the steady state HTC for a given set of time-invariant process parameters. Therefore, the main objective of this work is to lay the foundation for a numerical model that can predict and explain the time-resolved HTC based on physics and experimental observations.

As seen in Figure 1.9 the HTCs predicted from analytical models are inconsistent with those that are inferred experimentally. In addition to its tendency to overpredict, the analytical CMY model does not predict the “saturation” behavior observed in experiments. Understanding the factors for these discrepancies is another source of motivation for the present study. Model overprediction was hypothesized to be a result of incorrect selection of independent model parameters. The insensitivity of HTC in response to pressure was hypothesized to be a result of work hardening experienced by the deforming microasperities. The present experiment and proposed numerical model will add insights to this topic.

A deeper issue that must be resolved is the wide discrepancy in experimentally measured HTCs, as seen in Figure 1.6, because model development requires guidance from accurate experimental findings. Therefore, another objective of this work is to assess how experimentally inferred HTCs are influenced by unreliable temperature measurements caused by the delayed response of thermocouple probes inserted within the die and the assumption that the blank is thermally lumped in hot stamping of an Al-Si coated 22MnB5 steel, and nonuniform pressure across the blank-die interface. Hot stamping experiments were performed to collect the internal temperatures of the blank and die during quenching. The measured temperatures were analyzed to infer the surface heat flux leaving the blank and entering the die, and the heat flux comparison method demonstrated in Figure 1.7 was used to assess measurement reliability.

In parallel, a process will be developed to account for the biases in the measured blank and die temperatures. The contributions in this work will help reduce the variation in HTC results in future experimental studies, and the HTCs reported in this work may be incorporated into multi-physics simulations that determine hot stamping parameters resulting in automotive components with desirable mechanical properties.

Lastly, Klassen et al. [27] found that thicker Al-Si coatings led to smoother surfaces after austenitization, which motivated a follow-up investigation for the HTC. A potential result based on this new finding is that thicker coatings may lead to higher HTCs, which is surprising because it is contrary to the consensus of past experimental studies. Hence another objective of this work is to investigate the effect of Al-Si coating thickness on the HTC.

1.6 Overview of thesis

This work investigates the HTC evolution from experimental and theoretical perspectives. Chapter 1 covers the background of automotive hot stamping. A literature review of experimental and theoretical studies regarding the HTC is also provided in Chapter 1.

Chapter 2 introduces the experimental methods that were used to characterize the HTC. Details are given about the hot stamping apparatus and measurement principles. Inverse heat conduction and energy balance analyses for inferring the surface temperatures and heat flux from subsurface temperature measurements are described. A strategy for correcting the measured temperatures to account for experimental artefacts is discussed. The chapter closes on the process of obtaining the surface roughness of quenched samples using an optical microscope to study the effect of coating thickness on the HTC.

Chapter 3 discusses the results from the experiment. A general description of how the HTC evolves during quenching is given. The error induced on the HTC by the response delay of the die subsurface thermocouple probe and the common assumption that the blank is thermally lumped are discussed. The effect of nominal interfacial pressure and its spatial distribution on the HTC are also discussed and correlated to the measured surface roughness.

Chapter 4 uses the experimental findings as a foundation to describe the theoretical aspects that are required to model the evolving HTC during quenching. The computational domain, heat transfer submodel, and mechanical submodels of the overall model are explained.

Chapter 5 discusses model accuracy by drawing comparisons between the predicted and measured HTC histories. The effect of intermetallic coating on the HTC is investigated to explain why the analytical model tends to overpredict the HTC in hot stamping. The effect of martensite formation on the HTC is also discussed. The chapter closes on a parametric study to investigate the effect of secondary hot stamping parameters on the HTC.

Finally, Chapter 6 summarizes the results of this work with insight on how the scope of the work may evolve in the future.

Chapter 2

Experimental Methods

The methodology of the hot stamping experiments that were used to infer and characterize the HTC is discussed in this chapter. Content from two conference papers [60, 61] and one journal article [48] are reprised here.

In typical calculations of the HTC from Eq. (1.1), where quantities on the right hand side are inferred experimentally, the measured die subsurface temperature is directly substituted into an inverse heat conduction algorithm. This leads to the surface heat flux (q'') and die surface temperature (T_d). Meanwhile, the blank surface temperature (T_b) is typically assumed to be equal to its measured internal temperature. Due to experimental artefacts, as demonstrated in this chapter and the following chapter, it is proposed that the die subsurface temperature must be corrected to account for the response delay of the thermocouple before it is analyzed by the inverse heat conduction algorithm. Further, the heat flux obtained from analyzing the corrected temperature must then be used to estimate the true blank surface temperature, since the measured blank temperature may be prone to errors arising from welding a thermocouple to a blank. Along with various hot stamping processing parameters, the HTC was characterized against the surface roughness of fully quenched blanks, which were processed from surface topographies measured with an optical microscope.

2.1 Measuring temperature during quenching

Hot stamping experiments were performed using the custom, industrial-grade hydraulic press shown in Figure 2.1. The upper slide comprises an inner punch and outer binder,

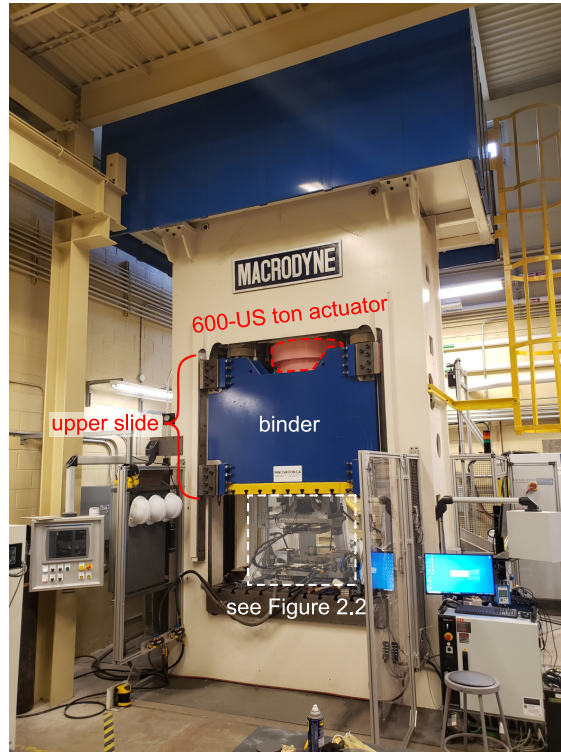


Figure 2.1: Custom, industrial grade hydraulic press used for hot stamping experiments.

each of which are controlled independently [62]. The punch is operated by either a single 5,340-kN (600-US ton) actuator, or two smaller actuators with a combined output of 534 kN (60 US ton) for increased sliding speed. The binder is operated by four actuators that provide a total of 2,670 kN (300 US tons). The position of the upper slide can be monitored at up to 1,000 kHz. The press offers open-loop and closed-loop capabilities for course and fine force control, respectively. In course control, the input force corresponds to a pre-defined control valve setting, while in fine control, an independent controller monitors the hydraulic pressure to actively adjust the control valves, which improves the accuracy of the force output. In the present experiment, the punch was exclusively used to quench the austenitized blanks for 20 s, while the controller was set to fine control mode. Nominal interfacial pressures of 0.2, 4.5, 8, 15, 25, and 40 MPa were tested. The lowest interfacial pressure was achieved by using only the weight of the upper die and its mounting cage. The highest listed interfacial pressure required the slower 5,340-kN actuator, while the remaining interfacial pressures were achieved using the two smaller actuators to minimize the approach phase duration and pre-mature air quenching of the blank.

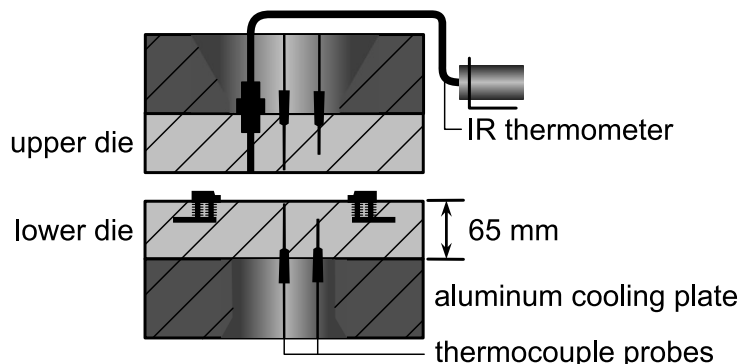


Figure 2.2: Schematic of flat dies and instrumentation.

The press was fitted with a pair of custom designed flat dies machined from AISI 4140 tool steel, each sized to 304.8 mm \times 304.8 mm \times 65 mm. The quenching surfaces were ground to an arithmetic roughness average of 0.5 μm about the mean line (R_a). As shown in Figure 2.2, the dies were instrumented with 1.57 mm-diameter K-type thermocouple probes (OmegaTM KMQSS-062E-12) using compression fittings to ensure good thermal contact between the thermocouple junction and measurement site. In each die, the probes were located 1.5 and 20 mm below the quenching surface to measure the “subsurface” and “far-field” temperatures, respectively. The subsurface measurement was used to infer the surface heat flux while the far-field temperature was used to validate the inferred quantity.¹ An additional 6.7 mm access port was milled through the upper die to accommodate an infrared (IR) thermometer (OmegaTM OS4001-V2) for measuring the surface temperature of the blank. To maintain the die temperature over multiple quenching cycles, each die was fixed to an aluminum cooling plate, which transfers heat from the die to a water-cooled steel plate. A detailed design report of the flat dies can be found in Appendix A.

The quenching blanks were made of Al-Si coated 22MnB5 steel with an as-received R_a of 1.5 μm . As shown in Figure 2.3, an open slot was milled to accommodate a K-type thermocouple (OmegaTM XR-K-20-100). The two 0.8 mm-diameter thermocouple wires, which came pre-wrapped in a protective glass sheath, were individually spot welded to the root of the slot to create an intrinsic junction.² The slot was narrowed near the root to

¹The inferred surface heat flux was validated by comparing the far-field temperature measurements against far-field temperatures calculated from a forward heat conduction analysis of the die in which the inferred heat flux was specified as a surface boundary condition on the die.

²The intrinsic junction was favoured over the extrinsic variant because the former integrates the blank surface between the two wires into the junction, resulting in a more precise temperature measurement compared to the latter type, which measures the wire temperature only at the initial point of wire-to-wire

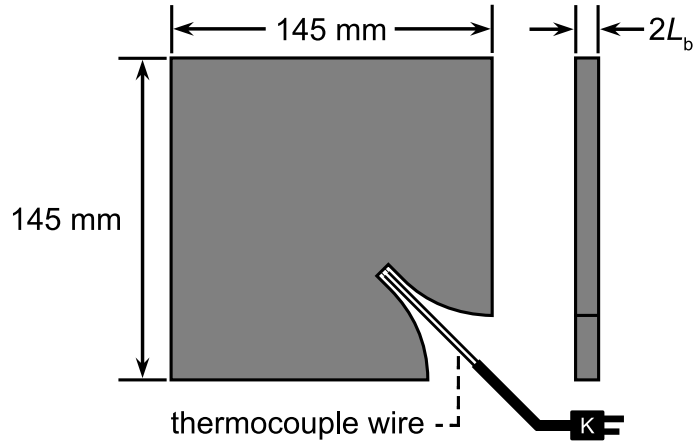


Figure 2.3: Top and side view of Al-Si coated 22MnB5 blank.

minimize measurement error caused by a lack of heat transfer into the die where the slot resides, and gradually widened to prevent the thermocouple from becoming caught in the blank-die interface.

Blanks with coating weights of 80 g/m^2 (AS80) and 150 g/m^2 (AS150), which have an as-received coating thickness of 14 and $25 \text{ }\mu\text{m}$ per side, were used to study the effect of the Al-Si coating on the HTC. The overall thickness ($2L_b$ in Figure 2.3) of as-received AS80 and AS150 blanks were 1.65 and 1.77 mm, respectively. The blanks were heated in a laboratory scale, electric muffle furnace (Lindberg Blue M BF51866A-1) at 930°C for 6 and 12 minutes to study the influence of furnace dwell times on the HTC, since the Al-Si coating thickness increases with dwell time. After being austenitized, the blanks were manually removed from the furnace and placed on four spring lifters fixed to the lower die, two of which are shown in Figure 2.2. The spring lifters minimize premature heat transfer between the blank and the lower die during the approach phase of the upper die. All measured temperatures were sampled at 100 Hz using a data acquisition system.

The calibration and performance of the IR thermometer was confirmed prior to conducting the hot stamping experiments. A blackbody cavity was used to verify the calibration and is shown in Figure 2.4a. The coefficient of determination (R^2) of a line representing theoretically perfect measurements against the actual measurements was 0.9977, indicating that the IR thermometer was well calibrated. Furthermore, the IR thermometer was used to measure the temperature history of an AS150-coated 22MnB5 coupon (single plate, 5 contact.

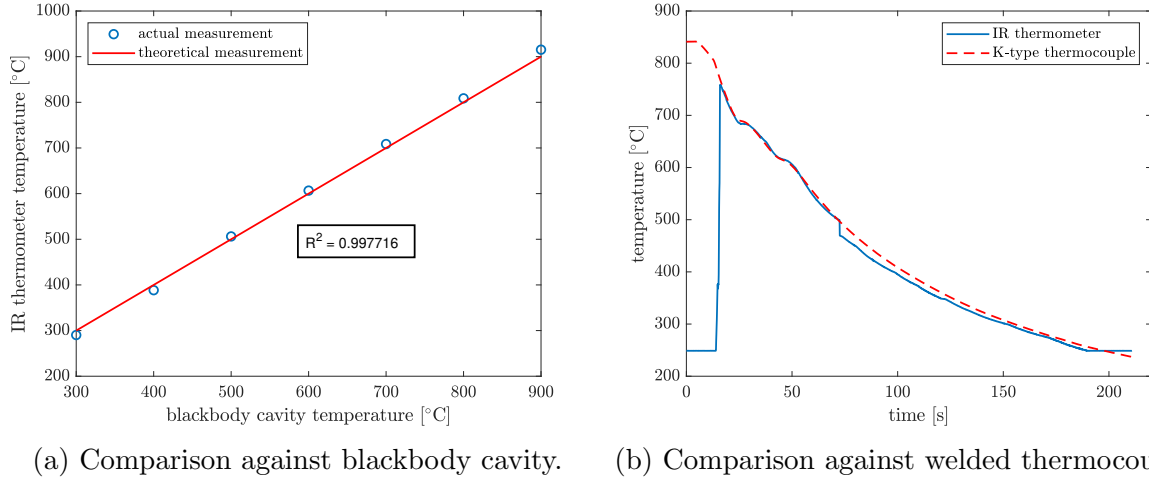


Figure 2.4: IR thermometer verified for calibration against blackbody cavity and compared against welded thermocouple wire for air-quenched 22MnB5 coupon.

$\times 5 \text{ cm}^2$) undergoing air-quenching. The coupon was instrumented with a K-type thermocouple. Figure 2.4b shows that the temperature history measured by the IR thermometer and K-type thermocouple are in good agreement. These preliminary tests suggested that the IR thermometer was suitable for measuring the surface temperature of the blank during hot stamping, which would have made the K-type thermocouple and the milling of an open slot in the blank unnecessary.

However, as shown in Figure 2.5, the IR thermometer suggested the blank surface temperature was greater than its internal temperature measured by the K-type thermocouple. In actuality, the surface temperature of an object being quenched is expected to be less than its internal temperature. The overestimation from the IR thermometer was attributed to a decrease in local cooling rate because of the lack of contact between the blank and die across the 6.7 mm access port. Therefore, measurements from the IR thermometer have been omitted from further analysis and discussion.

2.2 Inferring surface heat flux from temperature

Estimating the HTC using Eq. (1.1) requires knowledge of the time-resolved surface heat flux; by energy conservation, the heat flux entering the die (q_d'') equals the heat flux leaving the blank (q_b''). While q_d'' was inferred through inverse heat conduction analysis using

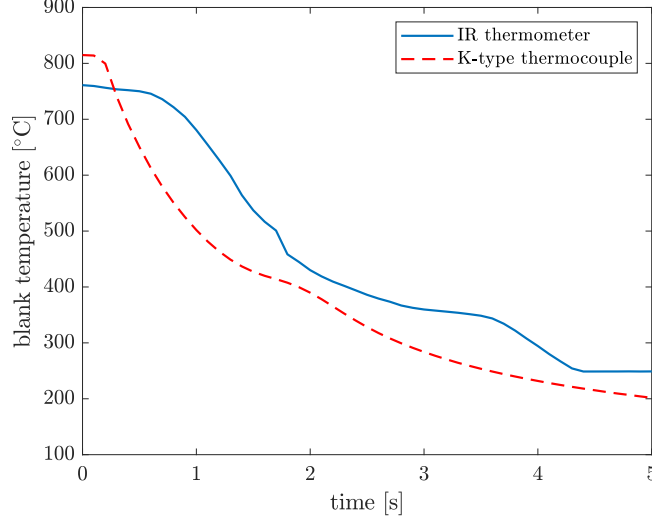


Figure 2.5: Temperature history of AS80-coated blank being quenched at a nominal interfacial pressure of 4.5 MPa.

measurements from the die subsurface thermocouple probe, q_b'' was obtained through energy balance analysis using measurements from the thermocouple wires welded to the blank. Both methods are described below, along with a justification for using q_d'' from inverse heat conduction analysis in Eq. (1.1).

In the inverse heat conduction analysis for the die, the subsurface temperature response, T_D , caused by a transient surface heat flux is governed by the Volterra integral equation of the first kind, which is derived in Appendix B and expressed as

$$T_D(t) - T_i = \int_0^t q_d''(t^*) \cdot \frac{d\phi}{dt}(t - t^*) dt^* \quad (2.1)$$

where T_i is the initial die temperature. The temperatures T_D and T_i , and the heat flux q_d'' are depicted in Figure 2.6 for a die modelled as a semi-infinite solid. The quantity ϕ is the so-called “sensitivity” of the measured subsurface temperature to the imposed surface heat flux, and is mathematically defined as

$$\phi(t) = \frac{\partial T_D}{\partial q_d''} \quad (2.2)$$

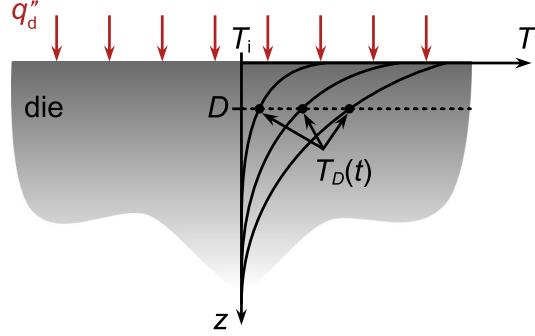


Figure 2.6: Nomenclature for inverse analysis on the die modelled as a semi-infinite solid.

Determining ϕ from Eq. (2.2) requires a conduction model that relates T_D and q''_d for the die. This was obtained by deriving the solution to a one-dimensional, transient heat diffusion equation for a semi-infinite die with a constant surface heat flux boundary condition. The solution to this forward problem at the measurement site is [63]

$$T_D(t) - T_i = \frac{2q''_d}{k_d} \sqrt{\frac{\alpha_d t}{\pi}} \exp\left(\frac{-D^2}{4\alpha_d t}\right) - \frac{q''_d D}{k_d} \operatorname{erfc}\left(\frac{D}{2\sqrt{\alpha_d t}}\right) \quad (2.3)$$

which by Eq. (2.2) leads to

$$\phi(t) = \frac{2}{k_d} \sqrt{\frac{\alpha_d t}{\pi}} \exp\left(\frac{-D^2}{4\alpha_d t}\right) - \frac{D}{k_d} \operatorname{erfc}\left(\frac{D}{2\sqrt{\alpha_d t}}\right) \quad (2.4)$$

where α_d and k_d are the thermal diffusivity and conductivity of the die, respectively, and D is the depth from the quenching surface (i.e., $D = 1.5$ mm corresponds to the subsurface measurement site).

With ϕ known, one may discretize Eq. (2.1) with respect to time to form the Stolz matrix equation

$$\begin{bmatrix} \Delta\phi_0 & 0 & \cdots & 0 \\ \Delta\phi_1 & \Delta\phi_0 & \cdots & 0 \\ \vdots & \vdots & \ddots & \vdots \\ \Delta\phi_{n-1} & \Delta\phi_{n-2} & \cdots & \Delta\phi_0 \end{bmatrix} \begin{bmatrix} q''_{d,1} \\ q''_{d,2} \\ \vdots \\ q''_{d,n} \end{bmatrix} = \begin{bmatrix} T_{D,1} - T_i \\ T_{D,2} - T_i \\ \vdots \\ T_{D,n} - T_i \end{bmatrix} \quad (2.5)$$

where $q''_{d,j}$ is the surface heat flux at the j^{th} time step, $T_{D,i}$ is the measured temperature at the i^{th} time step, and $\Delta\phi_{i-j}$ is the sensitivity coefficient representing the sensitivity of

$T_{D,i}$ to $q''_{d,j}$ and is evaluated using

$$\Delta\phi_{i-j} = \phi((i-j+1) \cdot \Delta t) - \phi((i-j) \cdot \Delta t) \quad (2.6)$$

Here, Δt is a time step between adjacent data points of temperature and correspond to its sampling frequency. Because the Stolz matrix is ill-posed, inverting Eq. (2.5) directly to obtain the time-resolved surface heat flux amplifies the measurement noise and model error (e.g., from temporal discretization), leading to a non-physical solution. Accordingly, inversion of Eq. (2.5) typically requires a combination of down-sampling the measured temperatures and regularizing the solution. In this work, temperatures sampled at 100 Hz were down-sampled to 20 Hz, which was sufficiently high to resolve the transient features of q''_d , while preventing the need for overregularization. Regularization was achieved using Beck's future time step method [64], in which the predicted surface heat flux for a given time step is assumed to be constant over the subsequent future time steps. Noise suppression in the inferred surface heat flux is improved by increasing the number of future time steps; however, an excessively large number of future time steps (i.e., overregularization) will also suppress physical aspects of the inferred surface heat flux. One future time step was used in this work.

The inferred surface heat flux regularized via Beck's method was substituted into a modified version of Eq. (2.5) to calculate the vector on the right-hand side containing the time-resolved die-surface temperature (T_d). This is a forward well-posed problem. The surface temperature sensitivity to the imposed surface heat flux is given by

$$\phi(t) = \frac{2}{k_d} \sqrt{\frac{\alpha_d t}{\pi}} \quad (2.7)$$

which resembles Eq. (2.4) except all instances of D were replaced with zero to represent the die-surface. The sensitivity coefficients ($\Delta\phi_{i-j}$) in the Stolz matrix equation were updated accordingly using Eq. (2.6). Then, the left-hand side of the modified Stolz matrix equation was computed to evaluate T_d .

To infer the heat flux leaving the blank (q''_b) from the midplane temperature measured by the thermocouple wires in Figure 2.3, an energy balance analysis was performed in which the blank was modelled as a thermally lumped mass. By equating the energy leaving the blank to its change in sensible energy, the outgoing heat flux at either one of its quenching surfaces is approximately

$$q''_b(t) = \begin{cases} -\rho_b L_b c_b(T) \frac{\partial T}{\partial t} & \text{if } T > M_s \\ -\rho_b L_b \left(c_b(T) + \Delta h_m \frac{\partial f_m}{\partial T} \right) \frac{\partial T}{\partial t} & \text{if } T \leq M_s \end{cases} \quad (2.8)$$

Table 2.1: Thermophysical properties of die [30] and blank [17] (T in $^{\circ}\text{C}$).

Thermophysical properties	AISI 4140 (die)	22MnB5 – austenite ($T > 400^{\circ}\text{C}$)	22MnB5 – martensite ($T \leq 400^{\circ}\text{C}$)
Density [kg/m ³]	$\rho_d = 7800$	$\rho_b = 7830$	$\rho_b = 7830$
Thermal conductivity [W/(m K)]	$k_d = 42.7$	$k_b = 19 + 0.01T$	$k_b = 49.35 - 0.045T + 1.55 \times 10^{-4}T^2 - 5.18 \times 10^{-7}T^3$
Specific heat [J/(kg K)]	$c_d = 473$	$c_b = 468 + 0.1538T$	$c_b = (1 - f_m)(468 + 0.1538T) + f_m(431 + 0.439T)$

where ρ_b and c_b are the density and specific heat capacity of 22MnB5, $\Delta h_m = 135$ kJ/kg is the latent heat release of austenite-to-martensite transformation, $M_s = 400^{\circ}\text{C}$ is the starting temperature of martensite formation, and f_m is the martensite phase fraction given by [65]

$$f_m = 1 - \exp[-0.011(M_s - T)] \quad (2.9)$$

The derivation of Eq. (2.8) can be found in Appendix B.

The thermophysical properties used in the inverse heat conduction analysis of the AISI 4140 tool steel die and energy balance analysis of the 22MnB5 blank are summarized in Table 2.1. The properties of the die were assumed to be constant since the die experiences a relatively small temperature change during the quenching process. Verification of both analyses involved conducting a set of FE simulations that are described in Appendix B.

Between the two analyses, q_d'' from inverse heat conduction analysis was substituted into Eq. (1.1) to estimate the HTC. Inverse heat conduction analysis accounts for the spatial variation of temperature within the die whereas the energy balance analysis is based on a lumped approximation that loses its validity at higher HTCs and thicker blanks. Furthermore, inverse heat conduction analysis can be independently executed on the upper and lower dies, whereas the energy balance analysis assumes q_b'' for the upper and lower quenching surfaces are equal, which is not the case due to the initial heat transfer between the blank and lower die during the approach phase of the upper die. Despite the inaccuracies in the energy balance analysis, q_b'' contained temporal information that was used to

adjust the temperatures measured within the dies, and provided a sense of whether the measured blank temperatures are representative of the overall blank.

2.3 Correcting measured temperatures

The methodology to infer the HTC based on Eq. (1.1) hinges upon the accuracy of the die subsurface and blank temperatures. However, as discussed by Caron et al. [30], the die subsurface thermocouple probe is prone to a response delay due to the thermal inertia of its junction and contact resistance between the junction and measurement site. The blank temperature measured by the welded thermocouple must be corrected if the blank-die interface condition near the measurement site is significantly different from the rest of the interface. This section shows how comparisons between q''_d and q''_b can help evaluate measurement accuracy and proposes a correction methodology.

2.3.1 Experimental procedure for correcting the measured die subsurface temperature

Accuracy of the die subsurface temperature measurement was investigated using a modified quenching experiment that involved manually pressing an austenitized blank against the lower die using two concrete trowels as shown in Figure 2.7. Absence of the upper die allowed the thermocouple wires to be welded on the blank's upper surface to ensure the measured temperature was representative of the entire blank since slots/holes were not involved. Each trowel was equipped with a layer of mineral wool to make the upper surface of the blank adiabatic and enforce $q''_d = q''_b$. The measured die subsurface and blank temperatures from the modified quenching experiment were analyzed to estimate q''_d and q''_b , respectively, and are plotted against time in Figure 2.8. The lagging history and smaller amplitudes of q''_d in comparison to q''_b suggest that the measured die subsurface temperature (T_{TC}) is temporally delayed relative to the actual die subsurface temperature (T_D). Conceivably, ignoring the effect of thermocouple response time (i.e., incorrectly assuming $T_{TC} = T_D$) would cause the HTCs to be underestimated.

The actual die subsurface temperature was approximated by performing an energy balance over the exposed junction of the thermocouple probe

$$T_D = \tau \frac{dT_{TC}}{dt} + T_{TC} \quad (2.10)$$

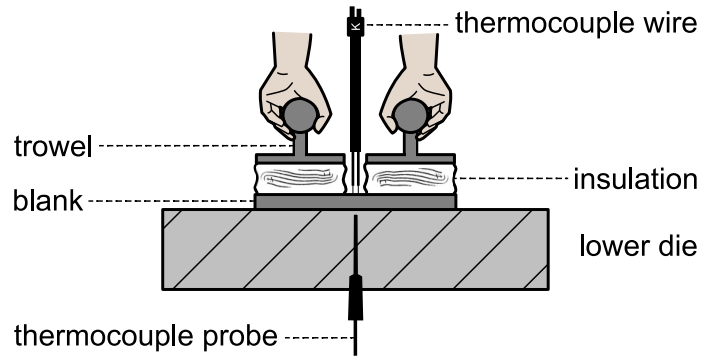


Figure 2.7: Modified quenching experiment for characterizing the time constant of the die subsurface temperature.

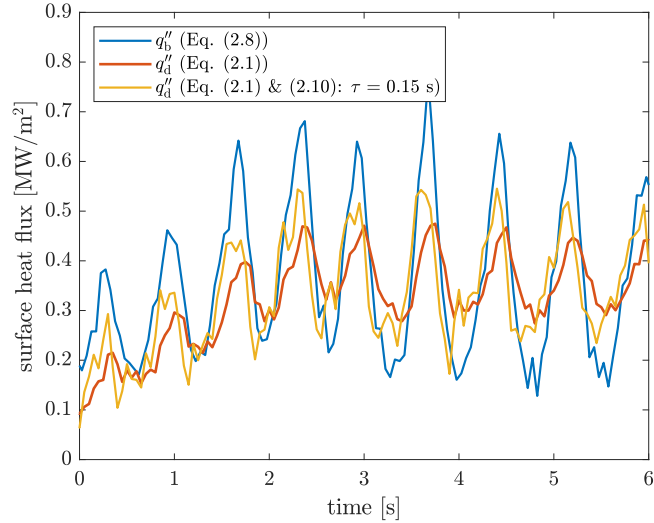
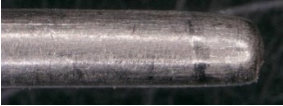
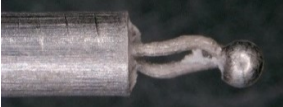



Figure 2.8: Heat flux leaving the blank (q_b'') and entering the die (q_d'') from the modified quenching experiment shown in Figure 2.7, where an oscillating force was applied manually on the blank.

Table 2.2: Summary of time constants for various thermocouple probes.

Junction Image	Omega TM Item No.	Junction Type	Time Constant, τ [s]
	TJ1-CAXL- IM15G-150	Grounded	0.7
	SCASS-062E-12- SHX	Exposed	0.35
	KMQSS-062E-12	Exposed	0.15

where τ is the thermal time constant representing the time required for a thermocouple to sense 63% of a step change in temperature. The thermal time constant is proportional to the thermocouple junction's total heat capacity and inversely proportional to conductance and contact area between the junction and measurement site. A time constant of $\tau = 0.15$ s resulted in time-resolved values of T_D that, when used in the inverse heat conduction analysis, led to temporal agreement between q''_d and q''_b as shown in Figure 2.8. The modified experiment was performed three times with the same time constant being recovered in each trial. Therefore, instead of using T_{TC} , the corrected temperature T_D evaluated from Eq. (2.10) with $\tau = 0.15$ s was used to infer q''_d in the main hot stamping tests involving both upper and lower dies.

The experimental method shown in Figure 2.7 was performed for two additional thermocouple probes, each with unique junctions, and the resulting time constants are summarized in Table 2.2. Compared to the two exposed variants, the grounded thermocouple had the highest time constant because the protective sheath increased the thermal resistance for conduction. Between the two thermocouple probes with exposed junctions, the variant with the thinner wires and smaller bead had the smaller time constant because of its lower thermal inertia. Using thermocouples with a smaller time constant is advantageous because the corrected temperature is less reliant on dT_{TC}/dt in Eq. (2.10), which minimizes noise amplification in the corrected temperature.

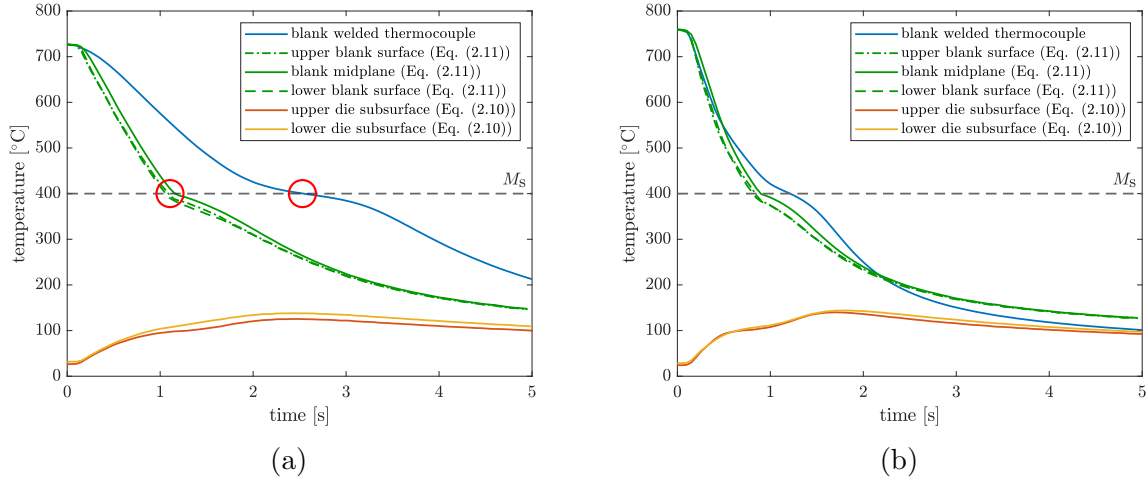


Figure 2.9: Measured and calculated temperature histories for (a) 6-minute heated, AS150 blank quenched at 0.2 MPa and (b) 6-minute heated, AS80 blank quenched at 40 MPa. The two red circles in (a) highlight inflections in the blank temperature history as a result of martensite formation.

2.3.2 Numerical procedure for correcting the measured blank temperature

In many of the present hot stamping experiments, there was evidence of temporal lagging in the measured blank temperature. This scenario is shown in Figure 2.9a for an AS150 blank heated for 6 minutes and then quenched at a target pressure of 0.2 MPa. As indicated by the two red circles in the figure, the measured blank temperature reached M_s after 2.5 s of quenching, yet the corresponding inflection in the die subsurface temperature from latent heat of transformation of austenite to martensite occurred only after 1.2 s. The temporal misalignment of the indicated and true temperatures was attributed to poor interfacial contact near the measurement site because of the surface grinding that was performed to remove protrusions created from welding the thermocouples. A slight concavity near the measurement site was preferred to ensure the blank and die made good overall contact, and that the inflection associated with martensite formation in the die subsurface measurements were consistent with those observed in the blank temperature measurements.

Instead of using the measured blank temperature, HTCs from Eq. (1.1) were estimated using blank surface temperatures predicted from the transient, one-dimensional heat dif-

fusion equation,

$$\begin{cases} \frac{\partial}{\partial z} \left(k_b(T) \frac{\partial T}{\partial z} \right) = \rho_b c_b(T) \frac{\partial T}{\partial t} & \text{if } T > M_s \\ \frac{\partial}{\partial z} \left(k_b(T) \frac{\partial T}{\partial z} \right) = \rho_b \left(c_b(T) + \Delta h_m \frac{\partial f_m}{\partial T} \right) \frac{\partial T}{\partial t} & \text{if } T \leq M_s \end{cases} \quad (2.11)$$

where k_b is the thermal conductivity of 22MnB5. The time-resolved values of q_d'' for the upper and lower die surfaces were imposed as boundary conditions on the blank. The initial temperature was set as the measured blank temperature at the onset of quenching. The process of solving the direct nonlinear heat conduction problem to estimate the blank surface temperature was demonstrated by Abdulhay et al. [17]. Eq. (2.11) was solved using an implicit finite difference method with 500 grid points to predict the nodal temperatures at each time step. As seen in Figures 2.9a and 2.9b, the predicted blank surface temperatures reached M_s at the same time when the inflection in the die subsurface measurement occurred. In addition, Figure 2.9b shows the predicted blank temperatures were in good agreement with the temperature measured from an AS80 blank that did not require any grinding near the measurement site. Temporal alignment with the die subsurface temperature and agreement with welded thermocouple measurement demonstrate the reliability of the predicted surface temperatures via Eq. (2.11).

2.4 Measuring surface roughness

Although the IR thermometer did not contribute to measuring temperature, its access port in the upper die introduced an unpressed, circular region on fully quenched blanks. The surface roughness of the resolidified Al-Si coating in the unpressed and pressed regions were compared on the same blank after quenching, uncovering the extent of plastic deformation experienced by the microasperities. The roughness of the quenched blanks in the unpressed region were also compared between blanks with unique coating weights to investigate the effect of coating weight on the roughness and HTC.

Initial attempts at measuring the surface roughness were conducted using a Wyko NT1100 optical profilometer, which utilizes white-light interferometry [66]. As shown in Figure 2.10, the resulting image for the unpressed region contained a low-density speckle pattern with excessive portions of black regions indicating unresolved areas. This occurred because the blank surface was optically rough, for which white-light interferometry is unable to resolve lateral surface structures [67]. Therefore, it was decided that optical profilometer was unsuitable for the present investigation.

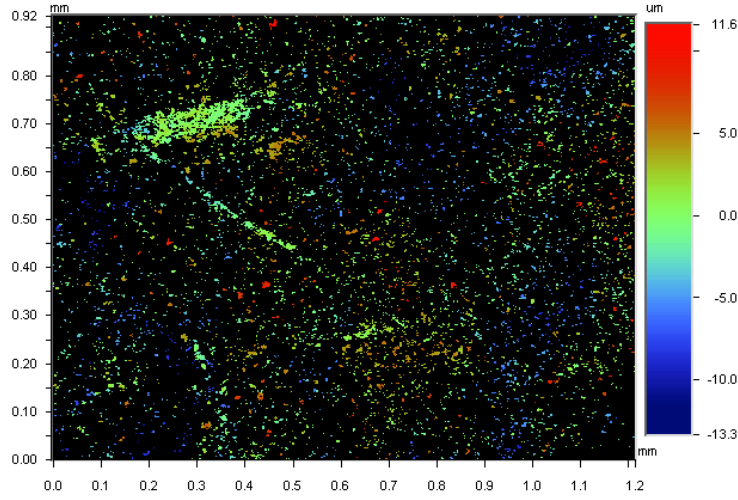


Figure 2.10: Low-density speckle pattern of a quenched blank measured by an optical profilometer.

Instead, high-resolution micrographs and areal surface height distributions from patches depicted in Figure 2.11 were obtained using a Keyence VHX-5000 optical microscope. The surface height data, which is digitally compiled from the microscope by recognizing the pixels that are in focus from multiple images evenly separated by a specified vertical pitch distance [68], was post-processed to obtain the arithmetic roughness average about the mean plane

$$S_a = \frac{1}{L_x L_y} \int_0^{L_y} \int_0^{L_x} |z(x, y) - \bar{z}| dx dy \quad (2.12)$$

where L_x and L_y are the micrograph dimensions (referring to Figure 2.11, $L_x = 270 \mu\text{m}$ and $L_y = 200 \mu\text{m}$), $z(x, y)$ is the surface height at x and y , and \bar{z} is the height of the mean plane [69]. As shown in Figure 2.11, nine patches were imaged in each region as opposed to taking one large image to minimize errors arising from the surface being tilted slightly, while ensuring that the inhomogeneous nature of the resolidified Al-Si coated surface was adequately captured.

To verify the accuracy of the optical microscope and the post-processing methodology, the surface roughness of a Mitutoyo Precision Reference Specimen with a roughness of $R_a = 3.10 \mu\text{m}$ was analyzed using the outlined procedure. With magnification levels of 2000x and 5000x and 50 images distributed over the vertical pitch, the resulting roughness were calculated to be $S_a = 2.91 \mu\text{m}$ and $S_a = 3.04 \mu\text{m}$, respectively. The error in S_a relative to the reference R_a from the higher magnification of 5000x was just 1.9% compared to 6.1%

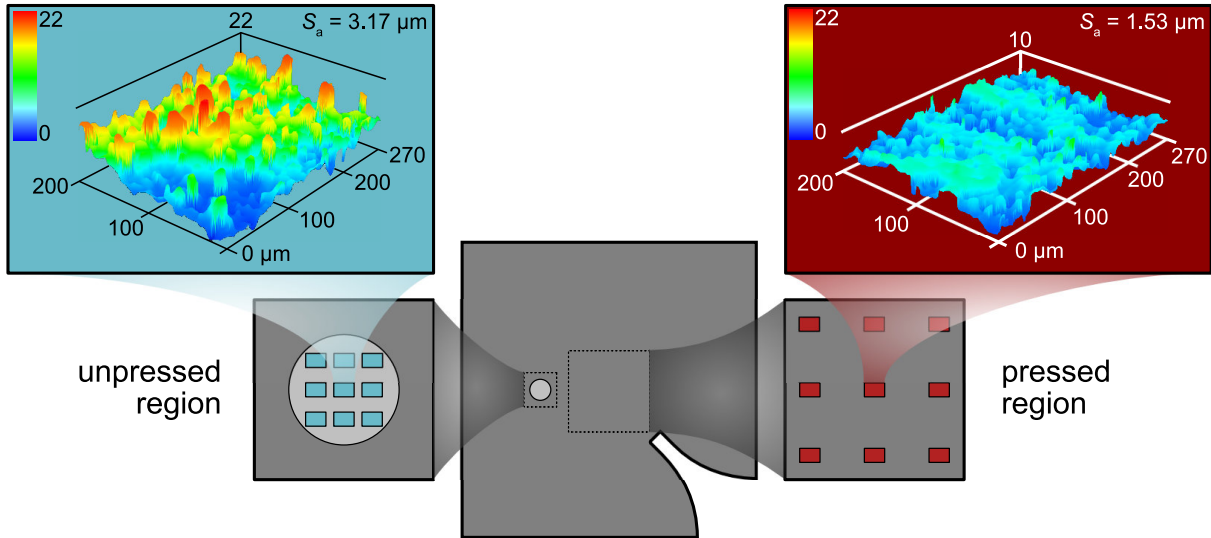
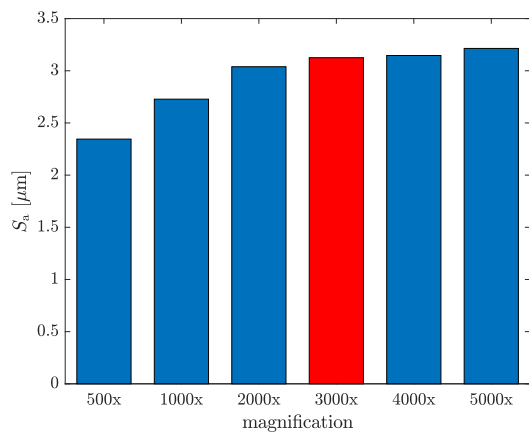


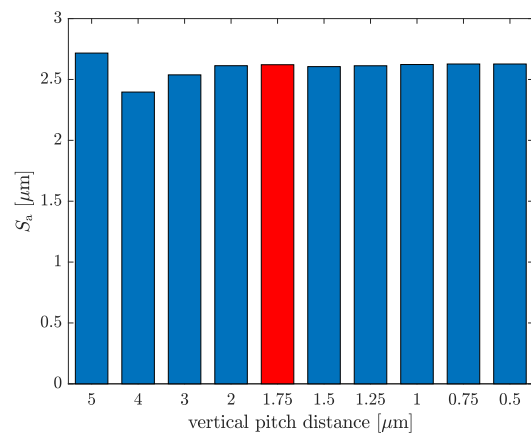
Figure 2.11: Digital microscope measurement sites on an AS80 blank heated for 6 minutes then quenched at 40 MPa, where the circle beside the label “unpressed region” indicates the area on the blank that does not contact the upper die.

for the lower magnification. The higher magnification led to a smaller error because higher frequency waves of the reference specimen were resolved better.

A series of measurements were conducted on a patch of the unpressed region of an AS80-coated blank (10-minute heated, quenched at 4.5 MPa) to select the optimal magnification and vertical pitch distance. As seen in Figure 2.12a, the value of S_a approached a steady value of approximately 3.1 μm starting at 2000x, so a magnification of 3000x was selected for the study. Then, with the magnification set to 3000x and the vertical pitch distance adjusted from 5 μm to 0.5 μm , the value of S_a converged to approximately 2.6 μm starting at a vertical pitch distance of 2 μm as seen in Figure 2.12b. A vertical pitch distance of 1.75 μm was selected for the present study.



(a)



(b)

Figure 2.12: Convergence study for (a) magnification with 50 images in the vertical pitch, and (b) vertical pitch distance with magnification fixed to 3000x. The selected microscope settings are displayed in red.

Chapter 3

Discussion of Experimental Results

The techniques developed in Chapter 2 are deployed on data collected at a range of interfacial pressures and furnace dwell times to understand the fundamental aspects of thermal contact resistance in automotive hot stamping, and to highlight the impact of the corrections on the recovered HTC. The surface roughness in the unpressed and pressed regions of fully-quenched blanks were investigated to relate the surface topography of the blank with the corrected HTCs.

3.1 Effect of thermocouple probe response delay

Figure 3.1 compares the measured die subsurface temperature against the corrected temperature that accounts for the time constant of the thermocouple probe in the case of an AS80 blank heated for 6 minutes and then quenched at 8 MPa. In general, the die subsurface temperature increases quickly at the onset of blank quenching, and then gradually decreases as the temperature field within the die becomes more uniform. However, the peak of the corrected temperature occurred 0.25 and 0.2 s earlier for the upper and lower die compared to the measured temperature. An inflection in the temperature history occurred at about 0.7 s due to the die absorbing the latent heat released by the blank. While the resolution of abrupt features in the transient regime improved, the corrected temperature was slightly noisier, particularly in the tail end of the temperature history. In reference to Eq. (2.10), measurement noise is scaled proportionally with the thermal time constant of the thermocouple probe.

Both measured and corrected subsurface temperatures were analyzed using inverse heat conduction analysis (i.e., deconvolving Eq. (2.1)) to infer the heat flux going into the upper

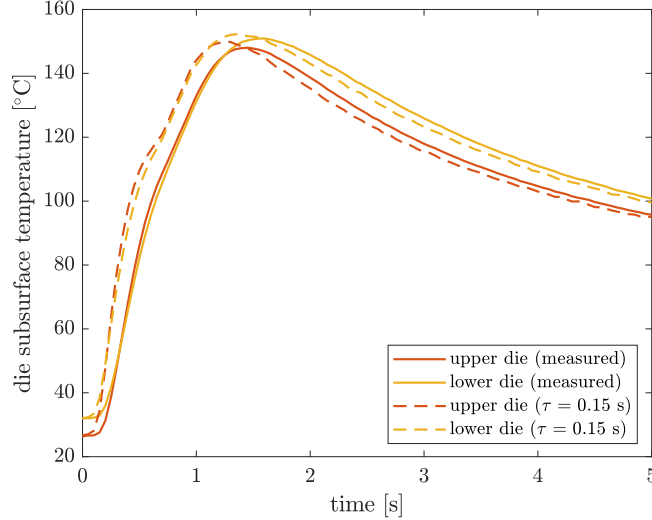


Figure 3.1: Measured (T_{TC}) and corrected (T_D via Eq. (2.10) with $\tau = 0.15$ s) die subsurface temperatures for a 6-minute heated, AS80 blank quenched at 8 MPa.

and lower dies, which are compared in Figure 3.2. The heat flux estimated from Eq. (2.8) is also shown for comparison. The heat flux entering the dies, in general, abruptly increases to its peak value due to the initially high thermal potential between the blank and die, and gradually decays as the blank and die approach thermal equilibrium. A momentary increase occurred during the decay due to the latent heat released by the austenite-to-martensite transformation of the blank, creating a secondary peak in the heat flux history. When accounting for the time constant ($\tau = 0.15$ s) of the thermocouple probes, the magnitude of the first heat flux peak was 37% higher in the upper die and 27% higher in the lower die. Additionally, the first peak occurred in almost half the time relative to the onset of quenching. As a result, the heat flux entering the upper and lower dies were more consistent with the heat flux leaving the blank prior to martensite formation. Accounting for the time constant also made the secondary peak in the heat flux histories more pronounced.

The inferred die surface heat flux histories in Figure 3.2 were used as boundary conditions to calculate the blank and die surface temperatures using Eqs. (2.11) and (2.1), respectively, and are plotted in Figure 3.3. In addition to the calculated blank surface temperatures, Figure 3.3a also shows the blank temperature measured by the welded thermocouple. In this specific quenching trial, grinding the blank surface near the thermocouple was not necessary, so good contact was made between the blank and die near the measure-

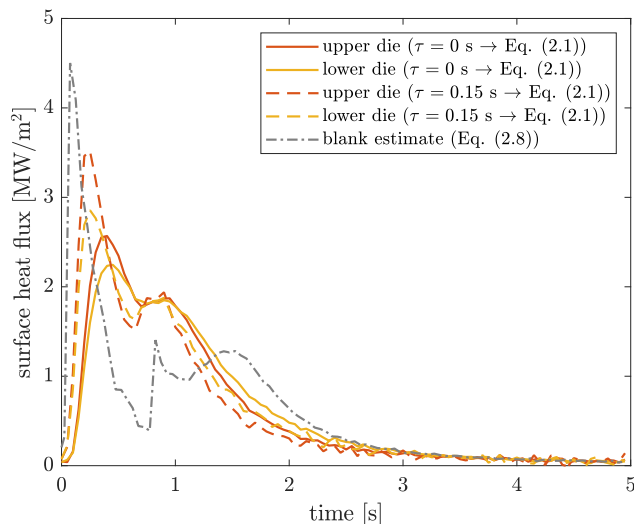


Figure 3.2: Die surface heat flux histories obtained by deconvolving Eq. (2.1) for a 6-minute heated AS80 blank quenched at 8 MPa.

ment site. The blank surface temperature predicted via Eq. (2.11) was in good agreement with the measured blank temperature above 400°C when the heat flux inferred from the corrected die subsurface temperature was used. Without the time constant correction, the predicted blank surface temperature was temporally delayed and overestimated. Excluding the thermal time constant correction also led to die surface temperatures in Figure 3.3b that appeared to increase continuously to its peak and missed the momentary surface cooling observed just before austenite-to-martensite transformation.

The HTCs derived from the raw and temporally-corrected die subsurface temperatures are plotted against the time and blank surface temperature in Figure 3.4. The plots show two distinct stages over which the HTC increases. The first stage was partially a result of the press tonnage ramping up, which gradually deformed the microasperities of the blank and improved the thermal contact. The second stage resulted from the austenite-to-martensite transformation, during which both the thermal conductivity and volume of the steel substrate increase. While the influence of the former effect on the HTC is obvious, the increasing blank volume occurs faster than can be compensated for using the press controls, causing an increase in interfacial pressure and further deformation in the microasperities.

As shown in Figure 3.4a, correcting the die subsurface temperature removes the delayed history and refines the sharp features of the estimated HTC history. As a result, the horizontal lines in Figure 3.4b that represent the time-averaged HTC between the onset of

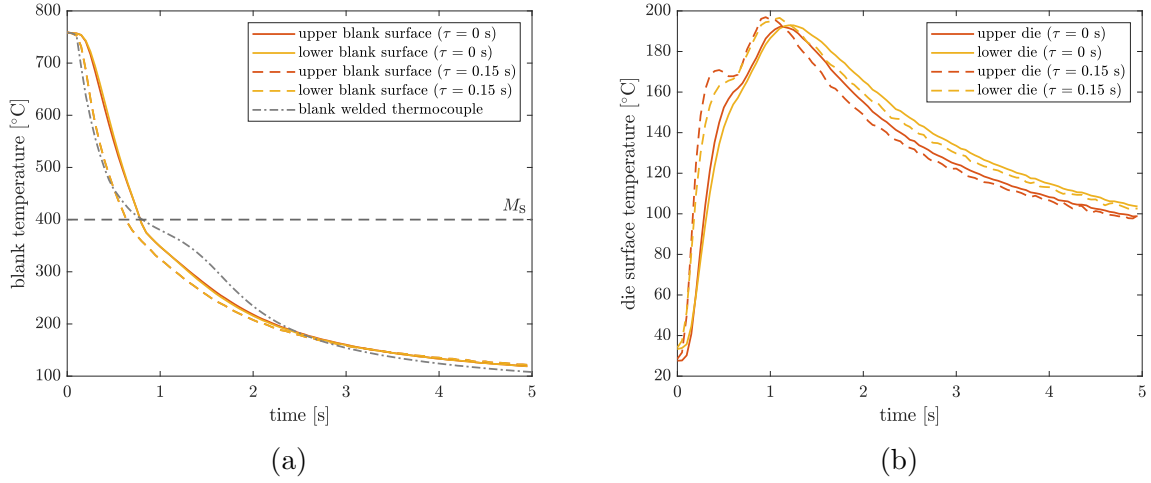


Figure 3.3: (a) Blank surface temperatures from Eq. (2.11) and (b) die surface temperatures from Eq. (2.1) for 6-minute heated, AS80 blank quenched at 8 MPa.

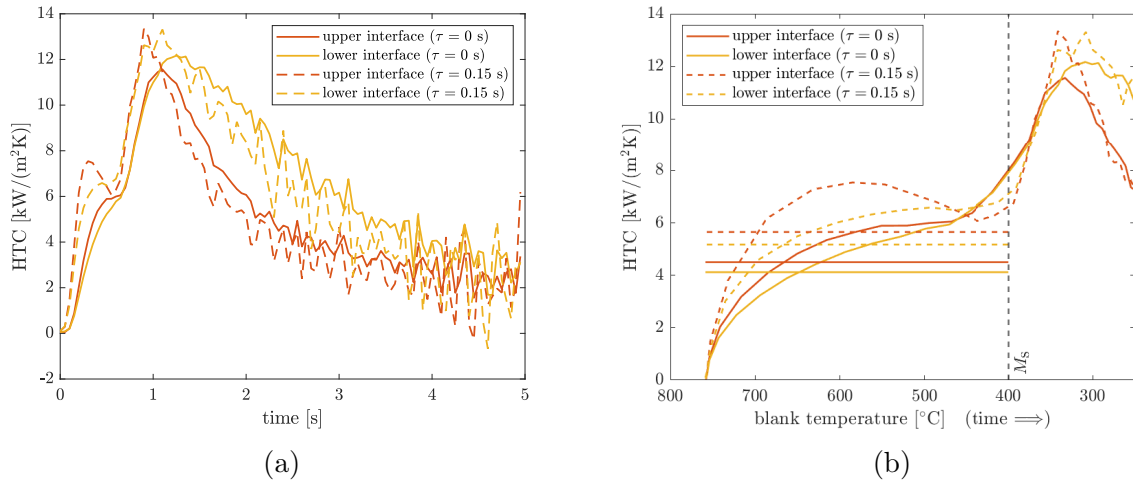


Figure 3.4: HTCs from Eq. (1.1) plotted against (a) quenching time and (b) blank temperature for a 6-minute heated, AS80 blank quenched at 8 MPa.

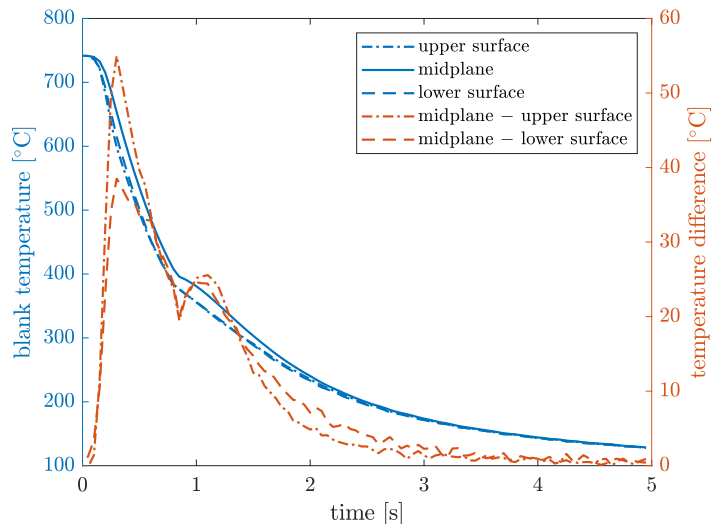


Figure 3.5: Blank temperatures from Eq. (2.11) along with their corresponding midplane-to-surface differences for a 6-minute heated, AS150 blank quenched at 8 MPa.

quenching to when the blank reaches M_s increased from 4.5 to 5.65 kW/(m²K) at the upper interface, and 4.12 to 5.17 kW/(m²K) at the lower interface, representing a 25% increase at both interfaces. Among all quenching tests involving AS80 and AS150, 6- and 12-minute furnace dwell times, and 0.2 to 40 MPa pressures, accounting for the thermocouple time constant increased the HTC by 11% to 31% compared to the uncorrected values.

3.2 Effect of overestimating blank surface temperature

The impact of treating the blank as thermally-lumped, and using the midplane temperature to approximate the surface temperature is summarized in Figure 3.5, which shows the blank temperature history and temperature difference between the surface and midplane of an AS150 blank heated for 6 minutes and then quenched at 8 MPa. The peak error/difference from assuming the midplane temperature is equal to the upper and lower surface temperatures were 55 and 39 K, respectively, which occurred near the beginning of quenching. This discrepancy decays gradually as the blank moves to thermal equilibrium, but temporally increases again at the onset at martensite formation.

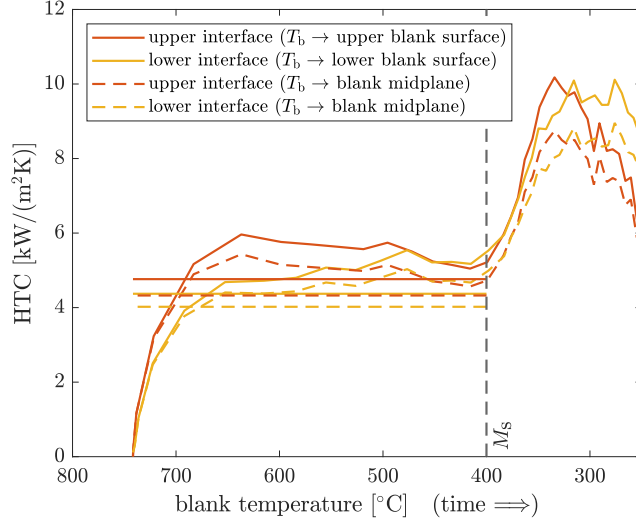


Figure 3.6: HTC from Eq. (1.1) plotted against blank temperature for a 6-minute heated, AS150 blank quenched at 8 MPa.

The results in Figure 3.5 were used to estimate the HTC at the upper and lower interfaces, which are plotted against the blank temperature in Figure 3.6. Using the midplane temperature of the blank appeared to scale down the magnitude of the overall HTC history at the upper and lower interface by about 9% in comparison to using the respective surface temperatures. As a result, Figure 3.6 shows the time-averaged HTCs prior to the onset of martensite formation went from 4.76 to 4.32 kW/(m²K) at the upper interface, and 4.37 to 4.02 kW/(m²K) at the lower interface, representing a 9% and 8% underestimation, respectively. Among all tested quenching conditions, the extent of underestimating the time-averaged HTC by using the midplane temperature ranged from 4% to 16%, with higher degrees of underestimation being observed in cases where the time-averaged HTCs were higher.

3.3 Effect of pressure on HTC

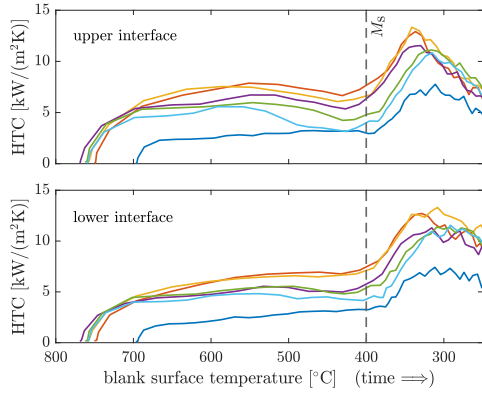
In most HTC experiments, the interfacial pressure is calculated from the imposed press loading divided by the surface area of the blank, and, most often, it is taken to be uniform over the blank surface area. From the present work, the impact of interfacial pressure on the HTC history and time-averaged HTC prior to the blank reaching the M_s temperature

are shown in Figure 3.7 for AS80 blanks heated for 6 and 12 minutes, and AS150 blanks heated for 6 minutes. As expected, the HTC at 0.2 MPa was consistently lower during quenching compared to higher pressures. However, blanks quenched at an intermediate pressure of 4.5 MPa consistently exhibited the highest average HTCs. While this result conflicts with results reported elsewhere in the literature (see Figure 1.6), Wen et al. [38] recently found that, in their experiments, the HTC was insensitive to interfacial pressures above 1 MPa, and noted that this value may depend on blank warping, thickness, and size.

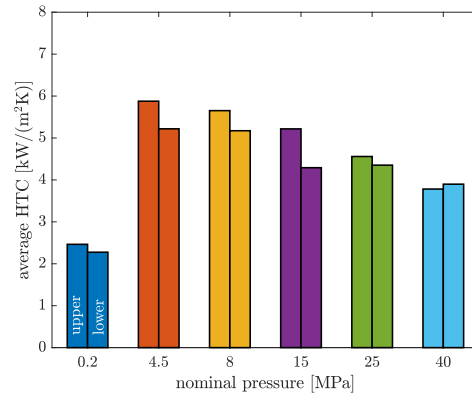
The minimum apparent pressure at which the HTC saturates may also depend on the distribution of interfacial pressure. To investigate this, a pressure-sensitive film was placed between an unheated blank and the lower die. Under a nominal pressure of 40 MPa, Figure 3.8a reveals higher pressures near the blank periphery. A complementary FE simulation was carried out on the die by specifying a roller constraint on the blank-die interface and a uniform external load on the opposing side. The resulting von Mises stress contour on the quenching surface, shown in Figure 3.8b, indicates that the die behaves like an elastic cantilever beam, deforming slightly and causing the interfacial pressure to increase near the blank edges. This qualitative analysis suggests that a nonuniform interfacial pressure is expected regardless of the flatness and parallelism of the blank and die surfaces. The higher local pressure at the blank edges, which exceed the desired pressure, explains why the HTCs appear insensitive at desired pressures lower than the commonly observed 10 MPa. The cantilever effect also explains the decreasing trend of the average HTC from 4.5 to 40 MPa, as shown in Figure 3.7, since higher press loads will increase deflection of the die and reduce the effective contact area. To maintain a uniform pressure, a common footprint between the blank and die is recommended.

Furthermore, in many cases the interfacial pressure is calculated assuming that the press reaches its set-point loading instantaneously. In view of the short timescales involved in forming, however, this assumption may be dubious, particularly at high interfacial pressures. Figure 3.9 shows ex-situ pressure histories measured using load cells substituted in place of the lower die. Three trials were performed for each target pressure to confirm the consistency and repeatability of the press load output. At the 40 MPa target, a steady state load of 38 MPa was achieved within 0.75 s, while the 4.5 MPa target was achieved in under 0.15 s. Despite the longer time to reach 40 MPa, the load remained consistently higher throughout the history compared to the lower target loads. Consequently, the diminishing time-averaged HTCs from 4.5 to 40 MPa in Figure 3.7 cannot be attributed to the longer ramp up period, although it should certainly be considered when calculating time-resolved HTCs.

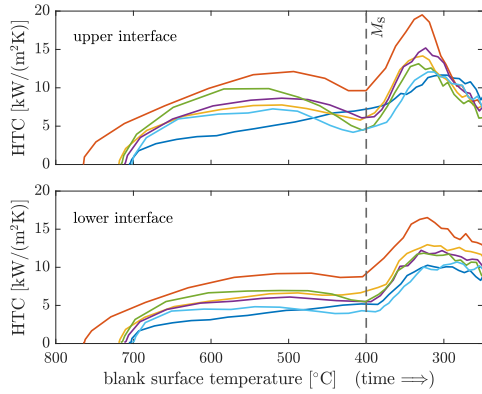
The effect of pressure on the HTC was reflected in the surface roughness of fully-quenched blanks. In Figure 3.10, the height of each bar represents the average S_a from



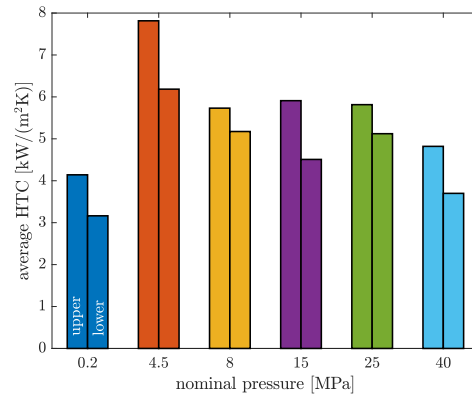
(a)



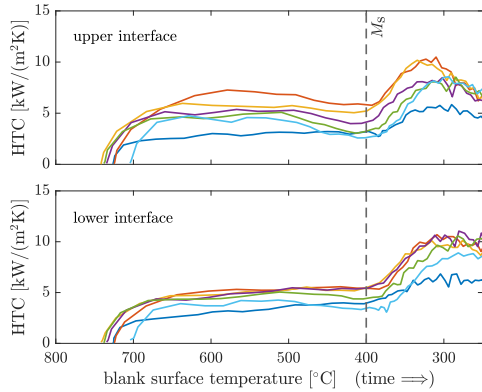
(b)



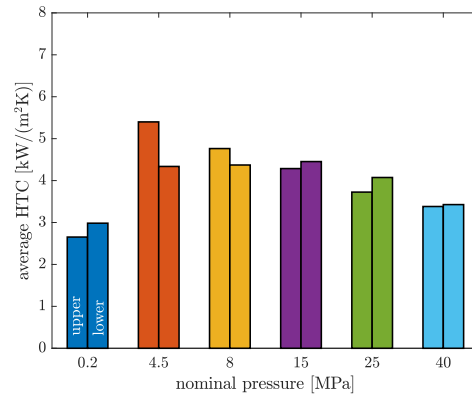
(c)



(d)



(e)



(f)

Figure 3.7: [(a), (c), (e)] HTC plotted against blank temperature and [(b), (d), (f)] time-averaged HTCs before the blank reaches 400°C for [(a), (b)] AS80/6-minute heated blank, [(c), (d)] AS80/12-minute heated blank, and [(e), (f)] AS150/6-minute heated blank.

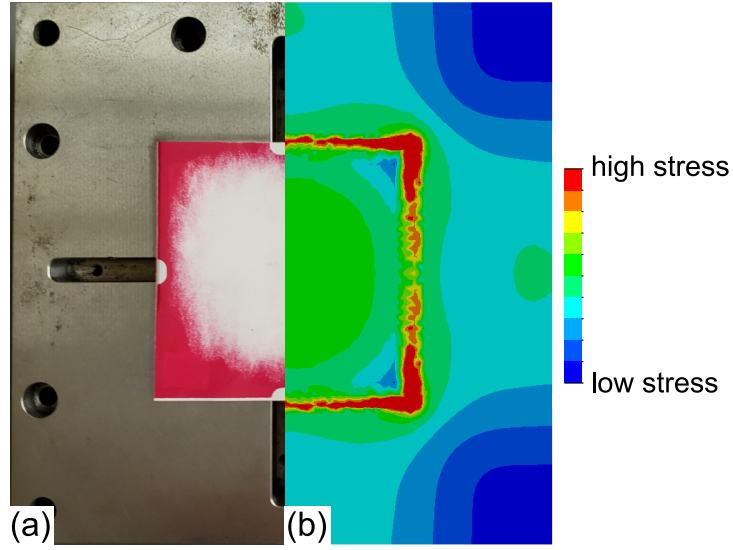


Figure 3.8: (a) Pressure-sensitive film (sensitive from 10 to 50 MPa) placed on lower die and (b) von Mises stress contour of die surface from complementary FE simulation.

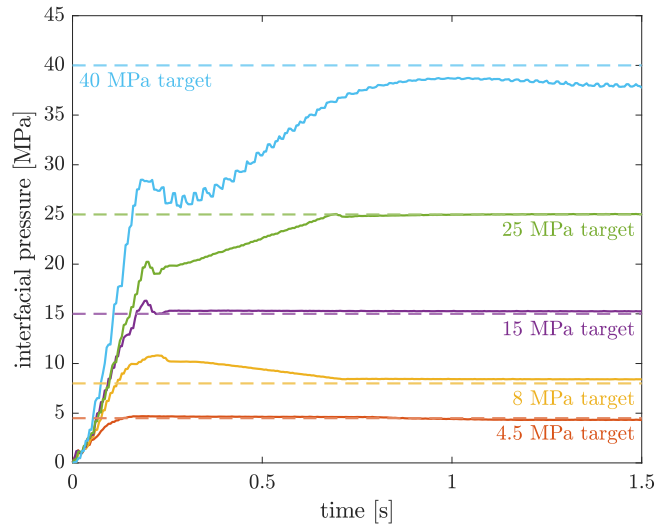


Figure 3.9: Ex-situ press output histories measured by load cells.

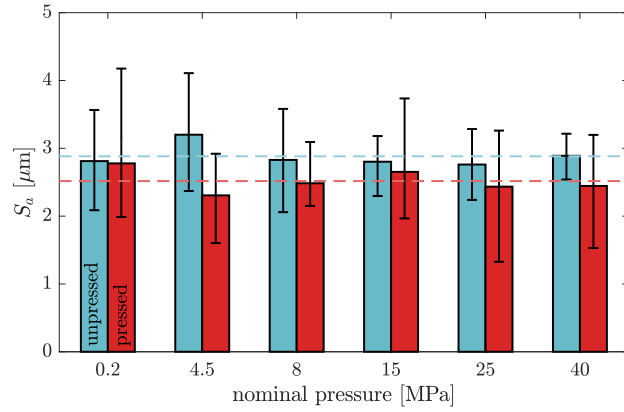
the nine surface patches measured with a digital microscope in the unpressed (blue bars) and pressed (red bars) regions indicated in Figure 2.11. The extremities of the vertical lines for each bar represent the maximum and minimum S_a from the nine patches. The average S_a values from the unpressed regions of AS80 blanks (i.e., blue bars in Figures 3.10a and 3.10b) were narrowly distributed about a mean of 2.88 μm (i.e., blue dashed horizontal line), and were always greater than the average S_a values of the corresponding pressed region, suggesting that the microasperities experience plastic deformation during quenching. In contrast, Figure 3.10c presents average S_a values in the unpressed and pressed regions of AS150 blanks that are distributed over a wider range, and the average S_a in the pressed region under the 25 MPa target was higher than the corresponding unpressed region. These observations suggest that AS150 blanks exhibit more surface inhomogeneity than their AS80 counterpart due to the thicker layer of Al-Si on the steel substrate.

3.4 Effect of Al-Si coating on HTC

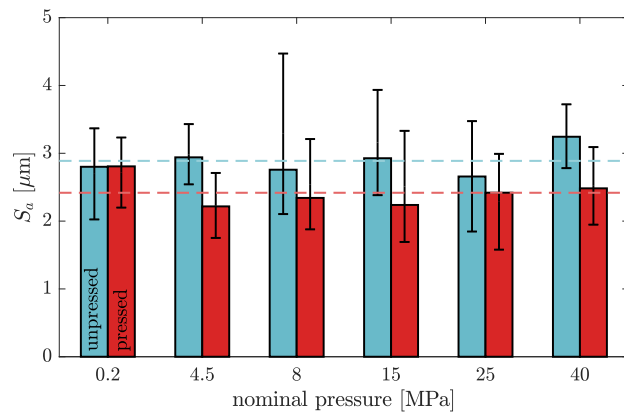
Increasing the furnace dwell time of AS80 blanks from 6 to 12 minutes generally increased the time-averaged HTC (Figure 3.7b and 3.7d). The average S_a in the unpressed regions was 2.88 μm for both dwell times, aligning with in-situ roughness measurements by Klassen et al. [27] that showed the S_a stabilized after approximately 4 minutes of furnace heating. However, the red dashed lines in Figure 3.10a and 3.10b reveal the average S_a over all tested pressures in the pressed region was 2.52 μm for 6-minute heated blanks, and 2.42 μm for 12-minute heated blanks. The smoother pressed region of 12-minute heated blanks corroborated with the higher HTCs.

Increasing coating thickness from AS80 to AS150 generally decreased the time-averaged HTC (Figure 3.7b and 3.7f), which correlates with the increased roughness of the AS150 blanks. In the unpressed regions, the average S_a was 2.88 μm for AS80 and 3.06 μm for AS150, while in the pressed regions, the average S_a was 2.52 μm for AS80 and 2.86 μm for AS150 (Figure 3.10a and 3.10c). Additionally, Figure 3.11 shows the surface topology of AS150 blanks exhibited larger uniformly higher areas in the unpressed region, potentially enhancing the structural integrity of its surface compared to the localized high spots on AS80 blanks. The reduced HTCs in AS150 blanks may also be attributed to the increased thermal resistance of the thicker coating.

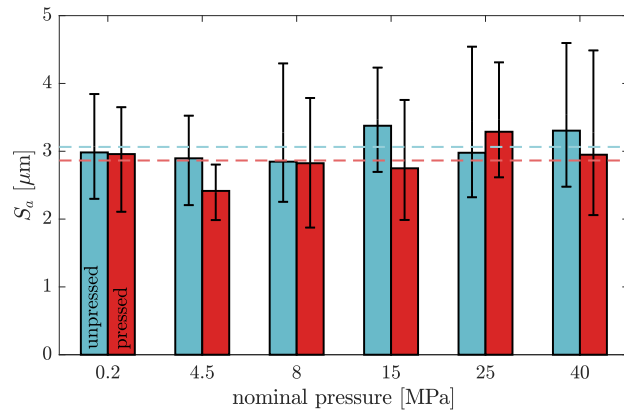
In contrast to the present study, Klassen et al. [27] found that the S_a for fully austenitized AS80 blanks were slightly higher at 2.75 μm compared to 2.65 μm for AS150 blanks,



(a)



(b)



(c)

Figure 3.10: S_a of (a) AS80/6-minute heated blanks, (b) AS80/12-minute heated blanks, and (c) AS150/6-minute heated blanks. Each bar and vertical line represents average and max/min values of S_a from the nine surface patches shown in Figure 2.11. Dashed lines represent average height of the bars.

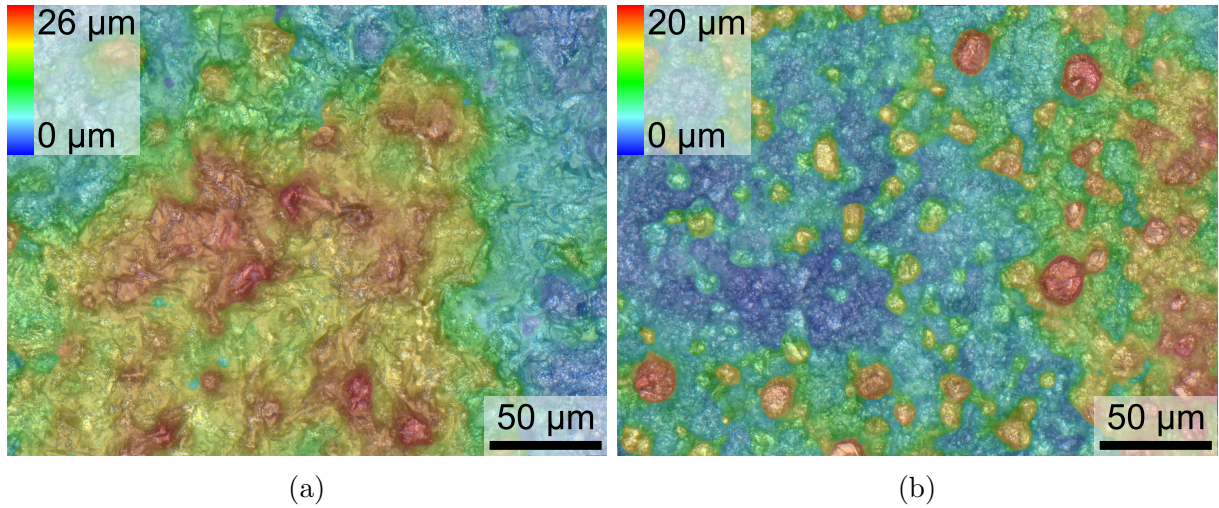


Figure 3.11: Typical micrographs in the unpressed regions of (a) AS150-coated blank heated for 6 minutes, and (b) AS80-coated blank heated for 6 minutes.

explaining that the thinner Al-Si coating allows more iron-enriched intermetallic compounds to diffuse to the surface, making it rougher. The opposing results between the two works may be a result of using different heating schedules in the furnace. While the same furnace with similar set point temperatures were used in both studies, Klassen et al. [27] studied blanks with overall areas of $38 \times 38 \text{ mm}^2$, which were much smaller than the $145 \times 145 \text{ mm}^2$ blanks used in the present study. Therefore, Klassen et al.'s [27] blanks only took two minutes to uniformly austenitize in the furnace, whereas a minimum of six minutes was required in the present study. The contrasting roughness results from changing the heating rates highlights the complexity of Al-Si coating evolution during the austenitization of 22MnB5 steel.

Chapter 4

Description of Preliminary HTC Model

The experimental results in the forgoing chapter show that the HTC depends on the magnitude and distribution of the interfacial pressure, and the roughness and mechanical properties of the blank's surface. The results also showed that the microasperities of the blank deform plastically during quenching, which causes the HTC to progressively increase as the press load output increases to the desired load over a finite period. These observations, as well as aspects that cannot easily be tested through physical experiments, can be investigated from a fundamental view using a physics-based model.

Such a model requires interconnected heat transfer and solid mechanics submodels, which are detailed in this chapter. Once the computational domain and initial imperfect contact between the blank and die are defined, the heat transfer submodel predicts the three-dimensional temperature field in the blank and die. Then, the mechanical submodel redefines the surface topography of the blank due to the progressive deformation that is driven by the evolving load or strain conditions. The two submodels are executed repeatedly in time until the evolution of the temperature field is known over a specified period. Finally, the temperature field at each time step is processed using Eq. (1.1) to infer the model-estimated HTC.

The model described in this chapter is in a preliminary state. The thermophysical and mechanical properties of the resolidified Al-Si coating is unknown at the time of writing. Consequently, substitute-properties are implemented to produce a set of interim solutions. In addition, the use of an explicit time-integration in the heat transfer submodel limited the blank surface node count below the threshold of grid independence. While incomplete, the

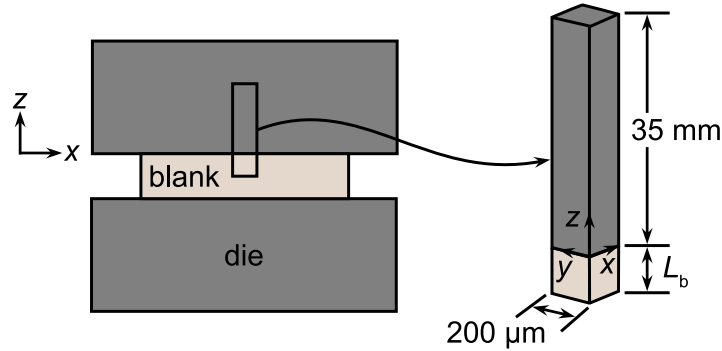


Figure 4.1: Schematic of three-dimensional computational domain.

preliminary HTC model still offers valuable insight in the physics and complex interactions of automotive hot stamping.

4.1 Computational domain

The computational domain is shown in Figure 4.1. The domain includes one of the flat dies and the half thickness of the blank to take advantage of symmetry. A $200 \times 200 \mu\text{m}^2$ column of the half-space was selected to enhance computational efficiency of the numerical solution method. This decision employs the assumption that observations in any local xy -plane are repeated globally. The thickness of the die was reduced from 65 mm in the experiment to 35 mm in the model to avoid unnecessary computations while ensuring the die thermally behaves like a semi-infinite solid.

The interfacial surface of the blank was modelled after the topography of an AS80 blank, which was measured by a Keyence VHX-5000 optical microscope. Measurements were taken from fully quenched blanks in the unpressed region as shown in Figure 2.11. Therefore, the measured surface topography is representative of the initial surface state in the forming and quenching phase.

The raw surface topography from a $200 \times 200 \mu\text{m}^2$ patch of the quenched AS80 blank is shown in Figure 4.2a. While the raw data came from an image with a resolution of approximately 2800×2800 pixels, the modelled surface topography was down-sampled to 28×28 pixels and is shown in Figure 4.2b. The down-sampled topography captures key features of the blank surface while minimizing the computational effort needed to evaluate the model. To maintain alignment with the elements representing the surface topography,

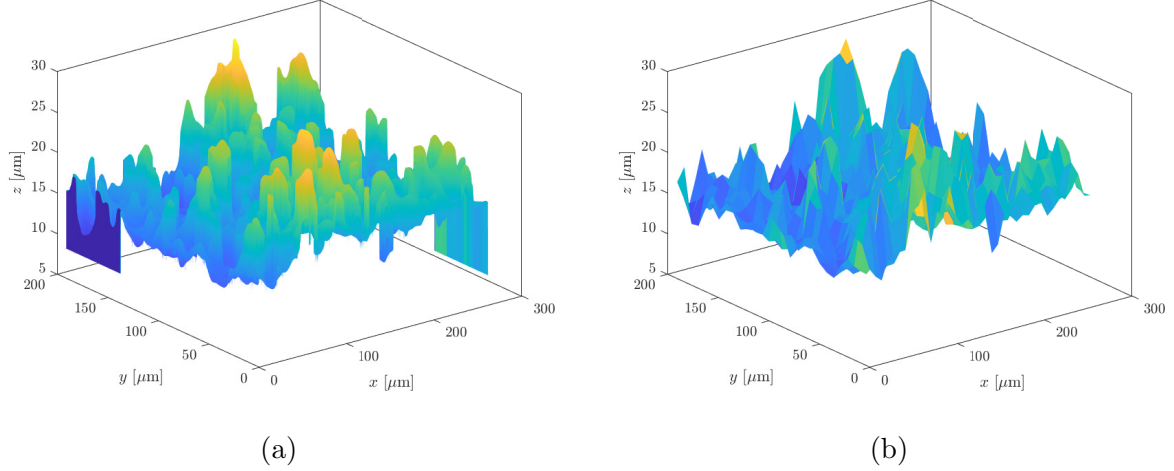


Figure 4.2: Comparison of (a) raw and (b) down-sampled blank surface topography, in which the latter is used in the model.

the computational domain was evenly divided into 28 elements in the x and y co-ordinate directions for a nominal grid spacing of $\Delta x = \Delta y = 7 \mu\text{m}$.

As mentioned in Chapter 2, the quenching surface of the dies were ground to an average arithmetic roughness (R_a) of $0.5 \mu\text{m}$, which is six times smaller than the R_a of Al-Si coated blanks just before the quenching operation. Therefore, the die surface was modelled as perfectly smooth.

In the z direction, the 35 mm thickness of the die was evenly divided into 280 elements for a grid spacing of $\Delta z_{\text{die}} = 125 \mu\text{m}$. While the initial half-thickness of the blank, L_b , was a test parameter ranging between 0.4 and 0.825 mm, the grid spacing was maintained at $\Delta z_{\text{blank}} \approx 50 \mu\text{m}$. With 28 elements in the x and y co-ordinate directions, 280 elements in the z direction of the die, and up to 16 elements in the z direction of the blank, the computational domain had up to 232,064 node-centered elements.

4.2 Heat transfer submodel

Heat transfer between the blank and die was modelled as being strictly due to conduction through asperity-to-asperity contacts since the small contributions of conduction and radiation within the interstitial air gaps are negligible compared to contact conductance. Perfect thermal contact was assumed between the intermetallic layer and 22MnB5 substrate of the

Table 4.1: Thermophysical properties of FeAl (40 at.% Al) [70] used to model Al-Fe-Si intermetallic.

Density, ρ [kg/m ³]	Thermal conductivity, k [W/(m K)]	Specific heat, c_p [J/(kg K)]
5,340	$-7.68 \times 10^{-6}T^2$ $+1.56 \times 10^{-2}T + 9.54$	$5.11 \times 10^{-7}T^3 - 6.48 \times 10^{-4}T^2$ $+4.44 \times 10^{-1}T + 555.67$

blank. Assuming constant thermophysical properties with no internal heat generation, the transient, three-dimensional conduction within the blank and die is governed by the heat diffusion equation

$$\frac{\partial^2 T}{\partial x^2} + \frac{\partial^2 T}{\partial y^2} + \frac{\partial^2 T}{\partial z^2} = \frac{1}{\alpha} \frac{\partial T}{\partial t} \quad (4.1)$$

Here, T is the temperature and α is the thermal diffusivity defined as $\alpha = k/(\rho c_p)$, where ρ is the density, k is the thermal conductivity, and c_p is the specific heat capacity. Aside from the contact interface, all boundaries of the computational domain were modelled as adiabatic. Unless otherwise specified, the initial temperatures of the blank and die were uniformly set to 750°C (as reported from the experiment in Figure 3.7a) and 22°C, respectively.

The thermophysical properties of the AISI 4140 die and 22MnB5 blank are summarized in Table 2.1 while the thermophysical properties of the resolidified Al-Fe-Si intermetallic layer on the surface of the blank are listed in Table 4.1. The properties of the die were assumed constant because the die experiences a relatively small temperature change during quenching. The Al-Fe-Si intermetallic properties were approximated by curve fitting data for solid castings of FeAl (40 at.% Al) [70]. While the thermal conductivity and specific heat capacity of the intermetallic layer and blank were specified as functions of temperature, their time and spatial derivatives in the heat diffusion equation were neglected by applying a quasi-steady assumption.

The heat diffusion equation was numerically solved using the finite difference method, in which an explicit time-integration was employed. The nodal temperature at each new time step ($i + 1$) was solved from the discretized equation

$$T_{P,Q,R}^{i+1} = T_{P,Q,R}^i + \frac{\Delta t}{\rho c_p \Delta x \Delta y \Delta z} (q_{P-1}^i + q_{P+1}^i + q_{Q-1}^i + q_{Q+1}^i + q_{R-1}^i + q_{R+1}^i) \quad (4.2)$$

where the subscripts P , Q and R indicate the x , y and z co-ordinates of the discrete nodal

points, Δx , Δy and Δz are the element side lengths, Δt is the time step size, and q indicates the rate of heat transfer into the (P, Q, R) element from one of the six neighboring elements indicated by the subscript. The value of q for a typical internal node was calculated from a discrete form of Fourier's law, for example

$$q_{P-1}^i = -k(\Delta y \Delta z) \frac{T_{P,Q,R}^i - T_{P-1,Q,R}^i}{\Delta x} \quad (4.3)$$

$$q_{Q-1}^i = -k(\Delta x \Delta z) \frac{T_{P,Q,R}^i - T_{P,Q-1,R}^i}{\Delta y} \quad (4.4)$$

$$q_{R-1}^i = -k(\Delta x \Delta y) \frac{T_{P,Q,R}^i - T_{P,Q,R-1}^i}{\Delta z} \quad (4.5)$$

The heat transfer rate between two interfacial nodes was calculated from the concept of equivalent thermal resistance networks to account for the change in thermophysical properties between two dissimilar materials [63]. This applied to heat transfer across the subinterface of the blank (i.e., 22MnB5 and intermetallic interface) and contact interface (i.e., intermetallic and die interface). For the example shown in Figure 4.3 where (P, Q, R) indicates an intermetallic node that interacts with a die node $(P, Q, R + 1)$,

$$q_{R+1}^i = \frac{T_{P,Q,R+1}^i - T_{P,Q,R}^i}{\frac{1}{2\Delta x \Delta y} \left(\frac{H_{\max}^i}{k_{\text{FeAl}}} + \frac{\Delta z_{\text{die}}}{k_{\text{die}}} \right)} \quad (4.6)$$

The result from Eq. (4.6) for all intermetallic nodes in contact with the die were added to obtain the total heat transfer rate across the modelled interface, and subsequently divided by the apparent contact area of $200 \times 200 \mu\text{m}^2$ to convert it to the surface heat flux required to solve for the HTC in Eq. (1.1). The routine executing Eqs. (4.2) to (4.6) was verified against a transient thermal FE model, which is detailed in Appendix C.

With up to 195,000 elements, and a time step size of 1.25×10^{-6} s to meet the stability criterion of explicit time-integration, computational efficiency was a critical aspect of the present work. Efficiency was improved by modelling the temperature field as one-dimensional within the die and the blank once the lateral variation of temperature fell below 1°C moving away from the contact interface. The algorithm is summarized for the blank in Figure 4.4, and is similarly repeated for the die.

Once the temperature field of the computational domain was known, the average temperature distribution in the z direction was fitted with 3rd and 2nd order polynomials in the blank and die, respectively. As seen in Figure 4.5, both polynomials were then extrapolated to the contact interface, and the difference in the extrapolated surface temperatures

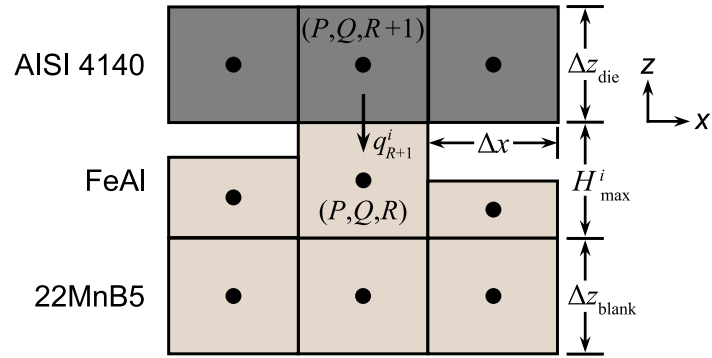


Figure 4.3: Schematic of three-dimensional computational domain.

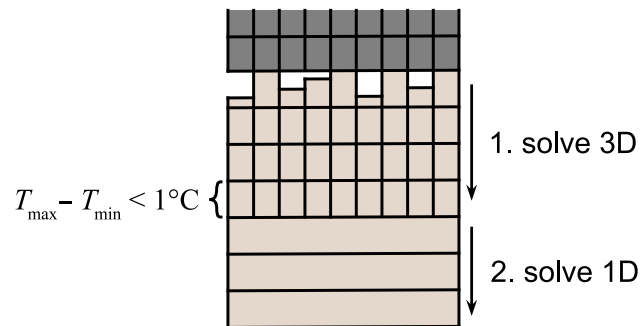


Figure 4.4: Procedure of transitioning from a three-dimensional (3D) conduction analysis to a one-dimensional (1D) conduction analysis in the blank.

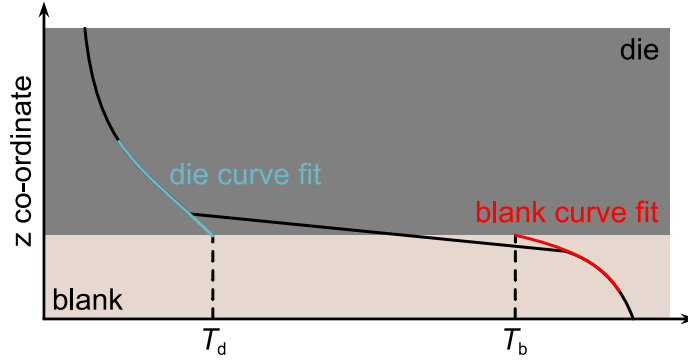


Figure 4.5: Extrapolated surface temperatures from polynomial curve fits of the predicted temperature distribution.

(i.e., $T_b - T_d$) was taken as the interfacial temperature jump, which was then substituted in the denominator of Eq. (1.1) to calculate the model-predicted HTC.

4.3 Mechanical submodel

The single layer of elements that represent the intermetallic coating were modelled to deform independently under uniaxial compression due to the load imposed by the press coupled with the thickening of the blank as its microstructure transforms from austenite to martensite. Only the tallest elements at any given time step contact the die and experience deformation. Poisson’s ratio was set to 0.5 to enforce volume conservation as the elements deformed.

The heights of each deformable element were based on the down-sampled surface topography shown in Figure 4.2b. Since deformation was assumed to occur exclusively within the resolidified intermetallic layer, the surface heights were uniformly inflated such that the tallest element had an initial height of 30 μm to match the intermetallic thickness reported in literature. While the as-received thickness of the Al-Si coating is on the order of 20 μm , the diffusion of iron from the steel substrate to the liquefied coating during austenitization increases the thickness of the resolidified Al-Fe-Si intermetallic by 10 μm [71, 72]. After uniform austenitization is achieved within the steel substrate, the coating layer primarily contains iron and aluminum, and the atomic concentration of iron increases with furnace dwell time and distance away from the surface.

Deformation of a single element representing the intermetallic layer due to an applied

Table 4.2: Statistically determined Norton-Hoff model parameters for 22MnB5 [73].

a	β	n	m
25.13 MPa s ^m	2,635.07 K	0.09042	0.05486

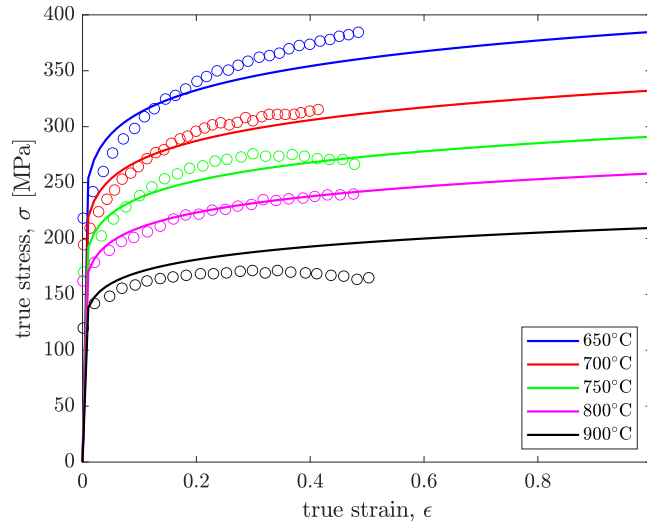


Figure 4.6: Comparison of true stress-true strain curves for a strain rate of 0.1 s^{-1} between isothermal compression tests [73] and curve fits via Norton-Hoff constitutive law.

force can be modelled by the Norton-Hoff constitutive law

$$\sigma = a \cdot \exp(\beta/T_{\text{abs}}) \cdot \epsilon^n \dot{\epsilon}^m \quad (4.7)$$

where σ is the true stress, ϵ is the true strain, $\dot{\epsilon}$ is the strain rate, and T_{abs} is the absolute temperature. The remaining terms in Eq. (4.7) are model parameters specific to 22MnB5 steel and are summarized in Table 4.2. The model parameters were determined by applying regression analysis on the plastic behavior of 22MnB5 measured from a series of uniaxial, isothermal compression tests [73]. A comparison of the measured results and model predictions is shown in Figure 4.6. Note that the measured plastic strain was approximated as the true strain because the elastic strain is small compared to the true strain anticipated for the asperities under load. The mechanical properties of 22MnB5 were used instead of the Al-Fe-Si intermetallic that makes up the coating layer due to the lack of literature available for the latter.

Calculating the deformation of multiple intermetallic layer elements from the force applied by the flat and rigid die is a nonlinear problem because each element initially has a unique height. The mechanical submodel calculates the maximum element height (H_{\max} in Figure 4.3) using the bi-section method such that the predicted force evaluated from

$$F_{\text{predict}}^{i+1} = \sum_{j=1}^N A_j^{i+1} a \exp(\beta/T_{\text{abs}}^{i+1}) \left[\ln \left(\frac{H_{\max}^{i+1}}{H_j} \right) \right]^n \left[\frac{1}{\Delta t} \left(\ln \left(\frac{H_{\max}^{i+1}}{H_j} \right) - \ln \left(\frac{H_{\max}^i}{H_j} \right) \right) \right]^m \quad (4.8)$$

equals the force applied by the press. In Eq. (4.8), A_j and H_j are the current cross-sectional area and initial height of the j^{th} element, N is the number of intermetallic elements that contact the die, and T_{abs} is the minimum absolute temperature of the intermetallic layer. Each term in the summation represents the unique reaction force of the j^{th} element against the die surface. The routine executing Eq. (4.8) was verified against a transient mechanical FE model, which is detailed in Appendix C.

As the blank cools below 400°C, its thickness increases gradually since the volume of martensite is 1.02 times greater than the austenite it replaces [16]. Assuming isotropic volume increase, a fully martensitic blank is $1.02^{1/3}$ times thicker than a fully austenitic blank. To maintain the desired interfacial pressure during the formation of martensite, the press controller actively expands the gap in which the thickening blank resides. However, the gap expansion is inherently delayed because of the finite response latency of closed-loop controllers, which causes the surface asperities to deform. As a result, the maximum element height at the $i^{\text{th}} + 1$ time step decreases to

$$H_{\max}^{i+1} = H_{\max}^i - \psi \sum_{R=1}^{N_{b,z}} \Delta z_{\text{blank}} \left[\sqrt[3]{1 + 0.02 f_{m,R}^{i+1}} - \sqrt[3]{1 + 0.02 f_{m,R}^i} \right] \quad (4.9)$$

where ψ is a heuristic press controller latency factor, Δz_{blank} is the grid spacing shown in Figure 4.3, and $f_{m,R}$ is the martensite phase fraction of the R^{th} nodal layer. Each term in the summation is the thickness increase of the R^{th} nodal layer, and the summation of all terms is the thickness increase of the blank. For ideal press controllers with zero latency ($\psi = 0$), expansion of the gap matches the thickness change such that the asperities do not deform. Conversely, if the press were to maintain a fixed gap ($\psi = 1$), the increase in blank thickness is fully translated into deforming the asperities.

Chapter 5

Discussion of Model Predictions

This chapter compares the modelled HTC values with experimental results. This is followed by an investigation on how the intermetallic coating and martensite formation affects the HTC as the blank cools below 400°C using the model. Finally, a parametric study is performed to understand how hot stamping process parameters that are typically not associated with the HTC affect its evolution during quenching.

5.1 Evaluation of model accuracy

The surface temperature and HTC history from the model and experiment are compared in Figure 5.1 for a blank of half-thickness $L_b = 0.825$ mm (i.e., the half-thickness of an AS80 blank in the experiment) quenched at a nominal pressure of 4.5 MPa. The choice of 4.5 MPa for this comparison stems from it being the lowest pressure with a finite press tonnage ramp up duration. The lower pressure helps filter out the cantilever bending effect of the die in the experiment, which can lead to non-uniform interfacial pressure. Additionally, the presence of a finite press tonnage ramp up facilitates the examination of the gradual increase in HTC during the initial period of the quenching process. Good agreement was observed in Figure 5.1a between the predicted and measured blank temperatures, highlighting the fact that the assumptions and submodels discussed in Chapter 4 are reasonable. In the HTC model, a press controller latency factor of $\psi = 0.3$ was applied in Eq. (4.9) to match the approximate two-fold increase of the experimentally measured HTC from the onset of martensite formation (see the 0.55-s mark of the blue curve in Figure 5.1b) to the measured peak HTC of ~ 13 kW/(m²K).

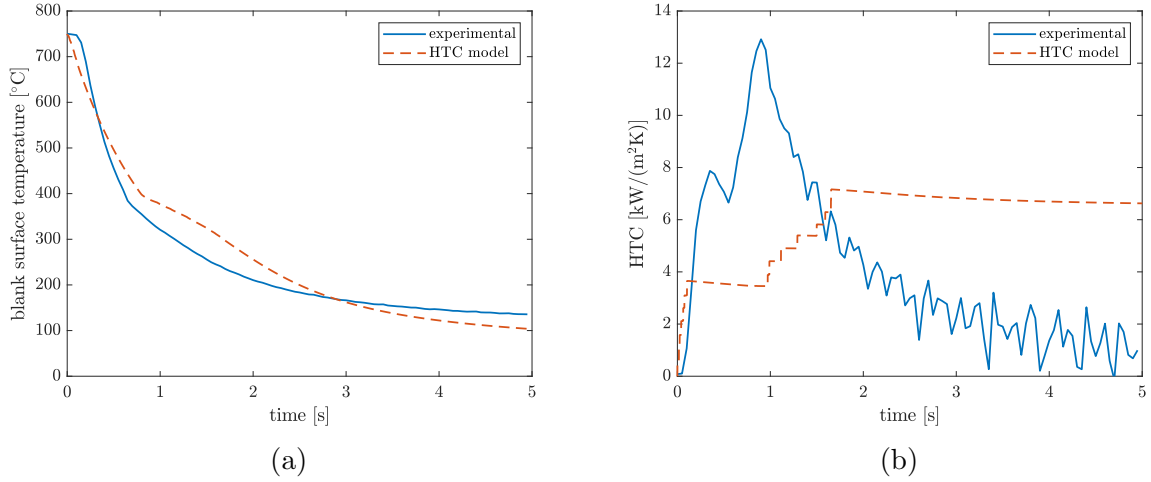


Figure 5.1: Comparison of model predicted and experimentally measured (a) blank surface temperature history and (b) HTC history for a 0.825 mm half-thick blank quenched at 4.5 MPa.

Referring to Figure 5.1b, the model (red dashed-line) predicts a gradual HTC increase near the beginning due to the press tonnage ramp up, followed by a slight decrease due to the decreasing thermal conductivity of the 22MnB5 blank and intermetallic surface coating, and finally followed by a second increase in the HTC at the 0.8-s mark due to the onset of martensite formation. These transient trends also appear in the experimentally measured HTC (blue line), where the second stage HTC increase occurs about 0.2 s earlier in comparison to the model prediction.

While Figure 5.1b demonstrates the model’s ability to fairly reproduce the two-staged HTC increase observed in the experiment in which the predicted and measured HTCs are within the same order of magnitude, there are four notable differences. First, the underprediction by the model relative to the measured HTC can be attributed to the fact that the mechanical properties of 22MnB5 were invoked for the blank surface instead of the Al-Fe-Si intermetallic coating. Second, the initial increase of the measured HTC occurred over the first 0.35 s (i.e., time taken for blue line to go from 0 directly to 8 kW/(m²K) in Figure 5.1b) compared to 0.125 s predicted by the model, even though both involve the same press tonnage ramp up duration of 0.125 s. The response time of the thermocouples is unlikely to be a contributing factor because the time constant was accounted for in the measured HTC. Instead, the discrepancy of the time period it takes the HTC to initially peak may be a product of an experimental artefact, or a physical phenomena that was

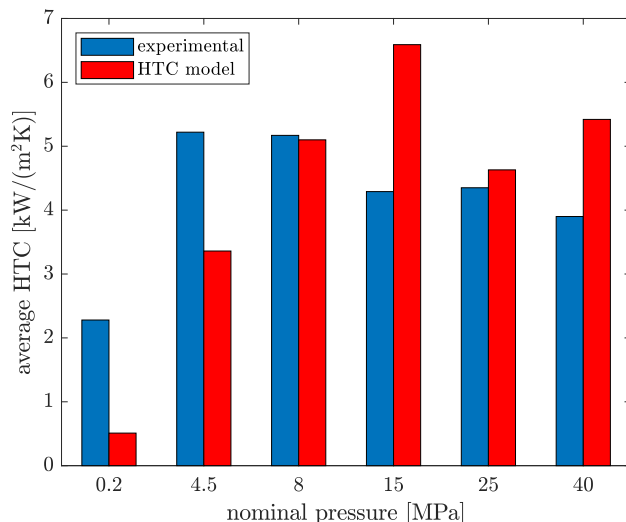


Figure 5.2: Comparison of model predicted and experimentally measured time-averaged HTCs between blank temperatures of 750°C and 400°C for AS80 blanks. Pressure ramp up durations of 0, 0.125, 0.125, 0.17, 0.7, and 0.8 s were specified in the model for the nominal pressures labelled from left to right, and the durations were based on the time it takes the press load to stabilize in Figure 3.9.

not accounted for in the model. Third, the predicted HTC remains steady after peaking whereas the measured HTC decreases. This is most likely a measurement artefact stemming from the die subsurface thermocouple probe becoming insensitive to the lower magnitude surface heat flux as the blank and die approach thermal equilibrium. The last difference is the step-wise increase of the model predicted HTC compared to the virtually smooth measurement. The prediction can be smoothened at the expense of computational time by increasing the element count in the x and y directions beyond the down-sampled selection of 28×28 elements. Smoothness may also improve with artificially rounded asperity peaks, which was discussed by Murashov and Panin [58] from the perspective of convergence and instability of the FE method.

The predicted and measured time-averaged HTCs as the blank cools from 750°C to 400°C are shown in Figure 5.2 for AS80 blanks. The initial press tonnage ramp up duration for each pressure in the model are specified in the caption. Because the ramp up duration increases significantly between the pressures of 15 and 25 MPa, the model predicted average HTC decreases. The relationship between the press tonnage ramp up duration and HTC is discussed in Section 5.4.

Figure 5.2 shows the model underpredicting the average HTC at lower pressures, and demonstrating better agreement at higher pressures. As discussed above, the underpredicted average HTC between the model and experiment is likely due to the incorrect mechanical properties being used to model the deformation behavior of the blank surface. For nominal pressures of 4.5, 8 and 15 MPa, the model predicted average HTC continually increase whereas the measured values plateau. The lack of plateauing was also observed in predictions made by the analytical CMY model (Figure 1.9). While the mechanical submodel captures work hardening through the Norton-Hoff constitutive law, and the increased reaction force of more elements as they come into contact with the die, the inability to capture HTC saturation with increasing pressure is likely related to the uniaxial compression assumption. The omitted interaction between neighboring asperities during deformation may be another source of surface hardening that imposes a maximum limit on the real area of contact and the HTC. The present numerical model can be improved by adding a boundary constraint on the asperities to limit unhindered expansion in the transverse directions and including friction at the contact interface. In the CMY model, the surface hardness parameter (HV) should be selected based on pressure such that higher pressures have diminishing return on the HTC.

5.2 Effect of intermetallic coating on HTC

Experiments have shown coated surfaces generally lead to lower HTCs. For example, Chang et al. [16] compared the HTC for blanks quenched with and without the application of an oxide preventing oil-based coating and found that the presence of the coating led to a significant reduction of HTC. In Figure 5.3a, the HTC predicted for the coated blank in Figure 5.1b is compared against the prediction for an uncoated blank. The coated and uncoated surfaces are defined by applying the thermophysical properties of FeAl and 22MnB5, respectively, on the blank surface. As concluded by Chang et al. [16], Figure 5.3a reveals that the resolidified intermetallic on the surface leads to a lower HTC throughout quenching. This is due to the lower thermal conductivity of the intermetallic throughout quenching temperatures compared to 22MnB5 as shown in Figure 5.3b. After the 0.7-s mark, the HTC for the uncoated surface (red dashed line in Figure 5.3a) exhibits sections of smooth inflation because 22MnB5 experiences a gradual increase in thermal conductivity as its microstructure transforms from austenite to martensite below 400°C. On the other hand, the HTC between the stepwise increases for the coated surface is relatively consistent, as is the thermal conductivity of FeAl.

Microscopic analysis of the sample in Figure 2.11 show the surface topography of

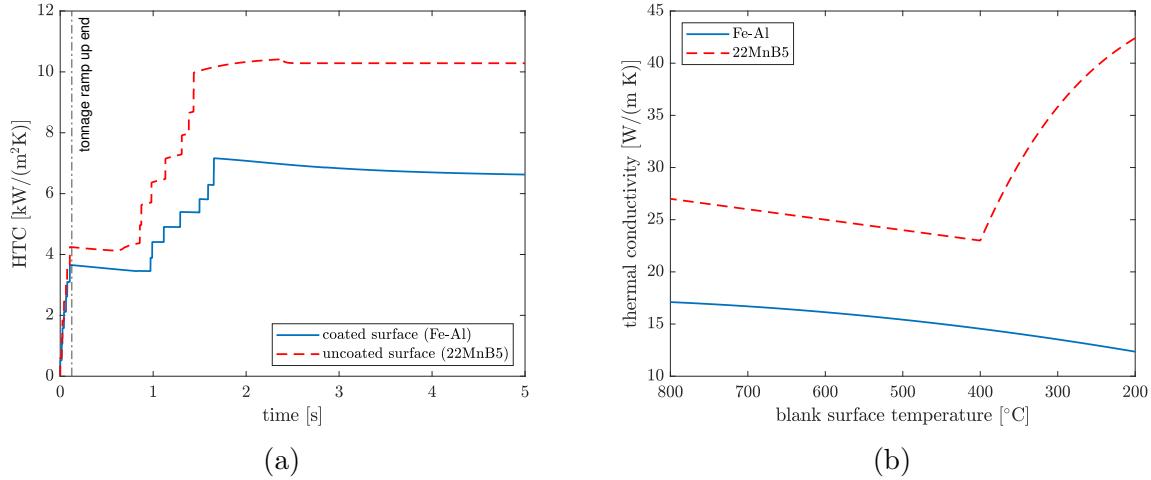


Figure 5.3: (a) Model predicted HTC histories for coated (intermetallic coating) and uncoated (bare 22MnB5) blank surfaces and (b) thermal conductivity evolution of FeAl and 22MnB5 during quenching.

the resolidified intermetallic layer is inhomogeneous, implying that the localized HTC is spatially-dependent. This is confirmed in Figure 5.4 where the predicted HTC seen in Figure 5.1b for the main surface topography is compared against the prediction from an alternate surface topography. Both main and alternative topographies are $200 \times 200 \mu\text{m}^2$ patches from the same blank that were measured by an optical microscope and down-sampled to 28×28 pixels, but taken at two different areas of the blank. Although the average deviation of the surface element heights of the alternative topography ($S_a = 3.24 \mu\text{m}$) is slightly lower in comparison to that of the main topography ($S_a = 3.67 \mu\text{m}$), the HTC for the former is unexpectedly similar at the end of the press tonnage ramp up, and lower at the end of martensite formation. This observation suggests that a single parameter like S_a representing the entire blank surface is inadequate when relating blank surface topography to the HTC because of the extent of inhomogeneity exhibited by Al-Si coated blanks. The ability to predict the HTC from inhomogeneous surfaces is thus an advantage that the present model has over analytical models requiring R_a or S_a to characterize the entire blank surface.

Based on the foregoing results, one may reason that Caron et al.'s [30] implementation of the analytical CMY model [51] led to overpredicted HTCs (see Figure 1.9) because:

1. the thermal conductivity of 22MnB5 was used instead of the intermetallic coating

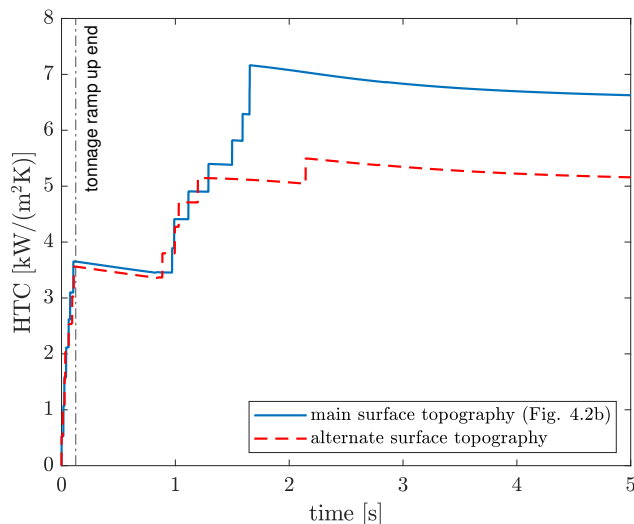


Figure 5.4: Comparison of model predicted HTC evolution for two different surface topographies measured from the same blank.

2. the roughness parameters of the as-received surface were used instead of the furnace-heated surface

The CMY model [51] parameters, along with recommended changes, are summarized in Table 5.1. Even with the five-fold increase in the mean asperity slope, using the lower thermal conductivity of FeAl and higher RMS roughness of unpressed AS150 coating leads to a $\sim 40\%$ decrease in HTC compared to Caron et al.'s [30] implementation.

In addition to the parameter values selected by Caron et al. [30], the overpredicted HTCs from the CMY model may be caused by the assumption that surface deviations from the mean plane ($z(x, y) - \bar{z}$) are Gaussian. The actual distribution for the intermetallic coating, inferred from the optical microscope, is skewed positively, as shown in Figure 5.5. This implies there are fewer asperity contacts between the coating and die than what is presumed by the CMY model, which may be one of the reasons experimentally inferred HTCs are smaller than the analytically predicted ones. However, the skewed distribution may also be a measurement artefact of the optical microscope (e.g., light trapped in deeper cavities).

Table 5.1: CMY model [51] parameters used by Caron et al. [30] along with recommended settings.

CMY model parameter	Caron et al.	Recommended
Thermal conductivity of blank surface, k_1	23 W/(m K) (22MnB5 at 400°C)	15 W/(m K) (FeAl at 400°C)
Mean asperity slope of blank, $ \tan \theta_1 $	0.054 (as-received AS150)	0.30 (furnace-heated AS150)
Std. dev. of asperity heights of blank, $R_{q,1}$	1.0 μm (as-received AS150)	3.78 μm (furnace-heated AS150)
HTC (Eq. (1.5))	See Figure 1.9	5.7% increase

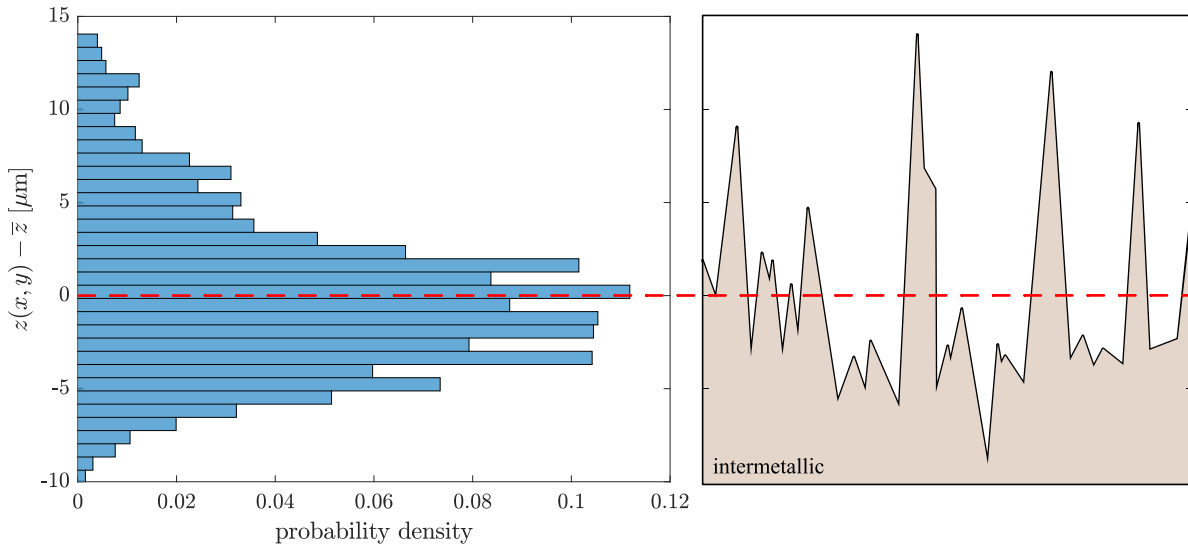


Figure 5.5: Histogram of surface deviations from the mean plane in the unpressed intermetallic coating (i.e., austenitized AS150-coated 22MnB5) and corresponding schematic of surface profile.

Table 5.2: Reference case for studying effects of martensite formation on the HTC ($T < 400^\circ\text{C}$).

Parameter	Value
Thermal conductivity of 22MnB5, k	23 W/(m K)
Specific heat capacity of 22MnB5, c_p	530 J/(kg K)
Press controller latency factor, ψ	0

5.3 Effect of martensite formation

During the austenite to martensite transformation of the 22MnB5 blank, latent heat is released, and its thermal conductivity and thickness increase. The relative effect of each listed phenomena on the HTC was investigated for a 0.825 mm half-thick blank quenched at a nominal pressure of 4.5 MPa. For comparison purposes, the reference case defined in Table 5.2 represents a hypothetical blank that does not experience any of the effects induced by the formation of martensite at temperatures below 400°C . The thermal conductivity and specific heat capacity in the table were calculated using the equations listed in Table 2.1 for austenite, and evaluated at 400°C .

Figure 5.6a compares the HTC between the reference case and a derivative case that accounts for the evolving specific heat capacity and latent heat release of 22MnB5 described by the function in Table 2.1 for martensite formation. The HTCs for the two cases are nearly identical aside from a slight discrepancy that develops after the 1-s mark when the blank temperature drops below M_s . These model predictions suggest that the latent heat release has a negligible impact on the HTC, and that the second stage of the HTC increase seen in the experimental results (e.g., Figure 3.4) cannot be attributed directly to the latent heat release as suggested by Chang et al. [16]. In fact, the direct impact of latent heat release on the HTC is smaller than it appears in Figure 5.6a because the reduced quenching rate of the blank shown in Figure 5.6b causes the thermal conductivity of the FeAl intermetallic coating to remain higher. Therefore, the latent heat indirectly increases the HTC slightly by increasing the intermetallic thermal conductivity.

The effects of increasing thermal conductivity and thickness of the transforming 22MnB5 on the HTC are shown in Figure 5.7. The near identical HTCs in Figure 5.7a suggest that the FeAl intermetallic on the surface shields the influence of the 22MnB5 thermal conductivity. On the other hand, Figure 5.7b shows that an increased press controller latency to expand the gap in which the blank resides in response to the thickening 22MnB5 substrate

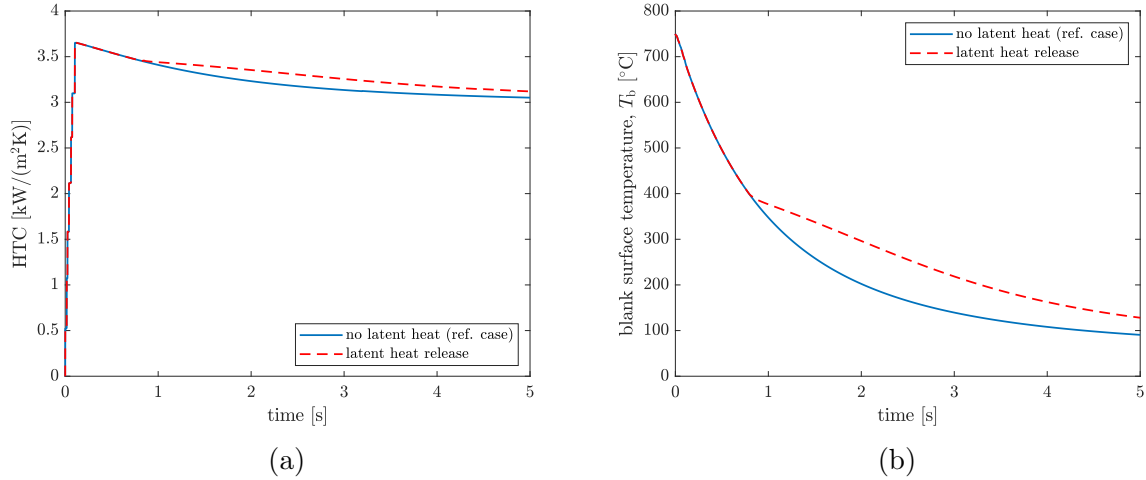


Figure 5.6: Effect of specific heat capacity and latent heat release during martensite formation on (a) the HTC and (b) blank surface temperature history ($L_b = 0.825$ mm, $p = 4.5$ MPa).

causes a significant increase in the HTC. Further investigation with control theory would be necessary to replace the simple press controller latency factor with real control system parameters.

5.4 Effect of hot stamping process parameters

A parametric study was performed using the present model to investigate the effect of press tonnage ramp up duration, blank thickness, and initial temperature of the blank and die on the HTC evolution. All cases were studied with a press controller latency factor of $\psi = 0.3$, and a target interfacial pressure of 8 MPa. The pressure is scheduled to increase linearly with time, and the target pressure is met at the end of the specified press tonnage ramp up duration. The parameters of the base case are defined in Table 5.3. All additional cases are derived from the base case, except for the one parameter that is being studied.

The HTCs for press tonnage ramp up durations of 0.125 and 2 s are shown in Figure 5.8a. The longer ramp up duration of 2 s resulted in an HTC evolution that was approximately half of the magnitude of the shorter duration. Longer ramp up durations generally lead to smaller HTCs because the desired interfacial pressure is attained when the blank is at a lower temperature and possesses a stronger surface. The blank surface temperature

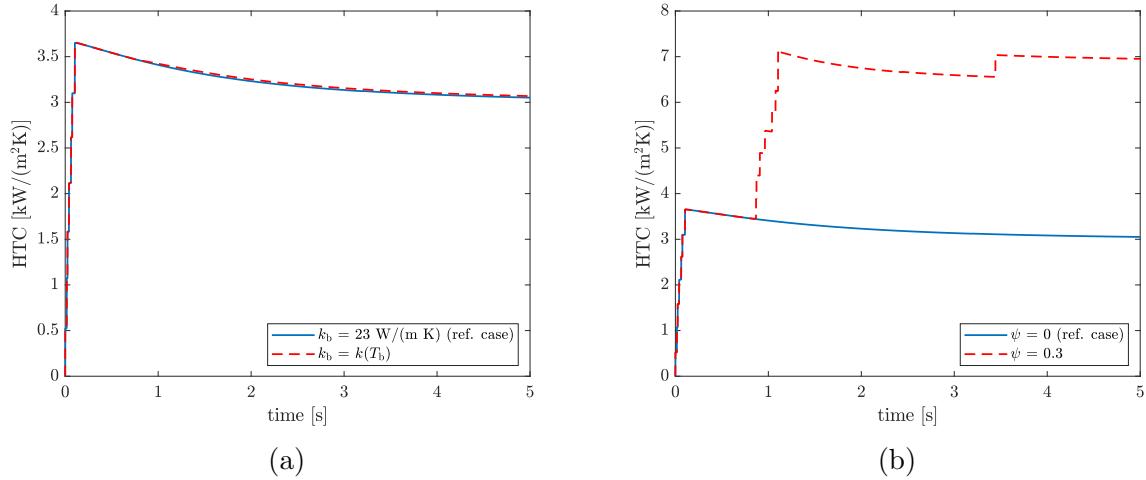


Figure 5.7: Effect of (a) increasing thermal conductivity and (b) thickness of 22MnB5 from martensite formation on the HTC ($L_b = 0.825 \text{ mm}$, $p = 4.5 \text{ MPa}$).

at the end of the two-second ramp up was 293°C , in comparison to 611°C at the end of the 0.125-s ramp up for base case. Figure 5.8b shows how 22MnB5 is significantly stronger at 293°C (red dashed line) than at 611°C (blue solid line), which explains why the longer press tonnage duration was unable to deform the asperities and increase the HTC to the same extent.

The effect of initial blank thickness on the HTC can be seen in Figure 5.9a. A two-fold increase in thickness led to a 11% increase in the HTC at the end of the 0.125-second press tonnage ramp up period. The dependence of HTC to blank thickness is caused by the higher thermal mass and lower quenching rate of the thicker 1 mm blank, allowing it to maintain higher surface temperatures and softer microasperities throughout quenching.

Table 5.3: Base case definition for the parametric study using the HTC model.

Parameter	Value
Press tonnage ramp up duration	0.125 s
Blank half-thickness (L_b)	0.5 mm
Initial blank temperature	750°C
Initial die temperature	22°C

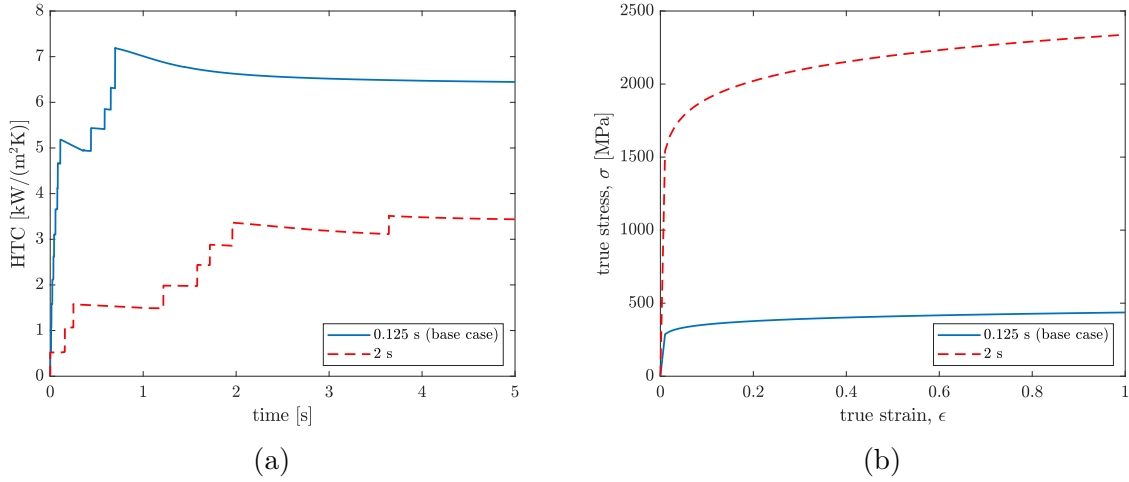


Figure 5.8: (a) Effect of press tonnage ramp up duration on predicted HTC history and (b) true stress vs true strain of uniaxially compressed 22MnB5 at the end of ramp up phase for the two compared cases.

For example, the surface temperature of the thicker blank is 39°C higher than for the thinner 0.5 mm blank at the end of the press tonnage ramp up. The increased deformation experienced by the asperities of the thicker blank is shown in Figure 5.9b. Once the press force stabilizes, the second stage of the HTC increase begins but is delayed for the thicker blank due to its lower quenching rate. This leads to a period between 0.6 and 0.9 s where the thinner blank exhibits a slightly higher HTC. Eventually the HTC of the thicker blank surpasses that of the thinner blank because the extent at which the blank thickness increases due to martensite formation depends on initial blank thickness, which indirectly appears in Eq. (4.9) via Δz_{blank} and the summation series. Finally, the longer duration of the second stage HTC increase for the thicker blank is related to the extended period of the thickness increase caused by slower quenching.

In practice, the initial blank and die temperatures are adjusted to control the quenching rate of the blank and mechanical properties of the final part. The initial temperatures also affect the HTC because the thermal and mechanical properties of the blank are coupled in hot stamping conditions. For example, one may reduce the initial temperature of the blank from 750°C to 600°C to lower the quenching rate. As shown in Figure 5.10a, a portion of the reduced quenching rate is contributed by the smaller HTC from lowering the blank temperature, which has been observed experimentally by Caron et al. [30]. The present model explains that the lower initial temperature of the blank causes it to remain cooler

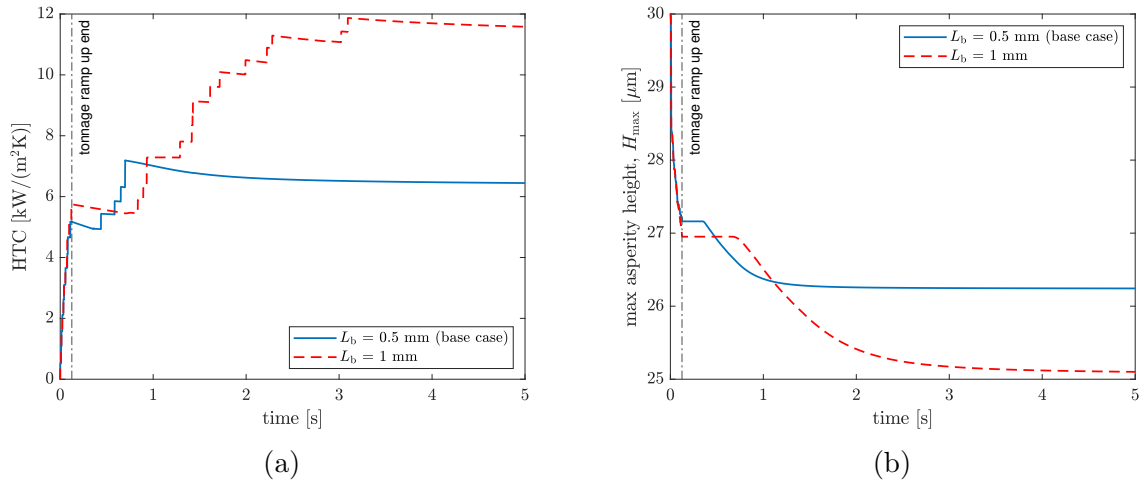
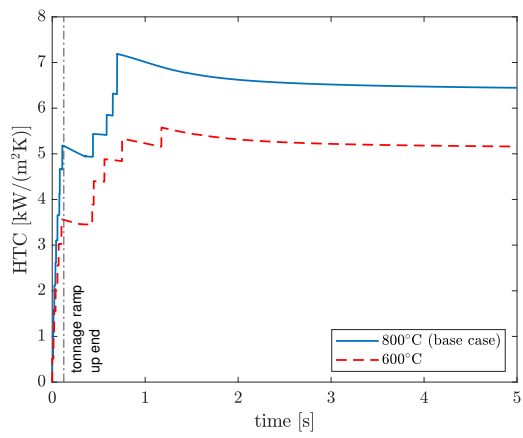
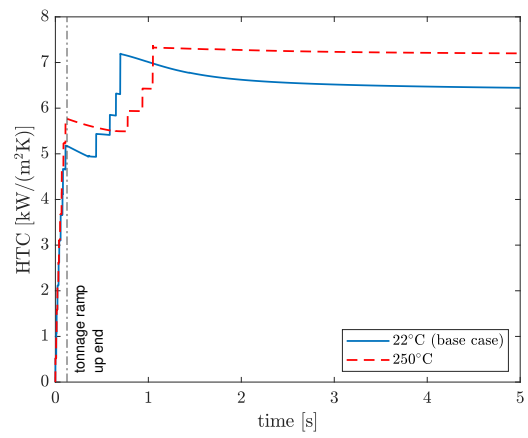


Figure 5.9: (a) Effect of blank half-thickness (L_b) on predicted HTC history and (b) deformation history of the maximum element height (H_{max}) for the two compared cases.

during most of the press tonnage ramp up, leading to harder asperities that reduce the extent of their deformation. On the other hand, one may also increase the initial die surface temperature using electric cartridge heaters to reduce the quenching rate of the blank [32]. However, as shown in Figure 5.10b, the HTC is greater during the press tonnage ramp up when the die is initially at 250°C compared to room temperature, which partially limits by how much the quenching rate may be lowered. Based on these predictions, adjusting the initial temperature of the blank has a greater impact on the HTC compared the initial temperature of the die.



(a)



(b)

Figure 5.10: Effect of (a) initial blank temperature and (b) initial die temperature on predicted HTC history.

Chapter 6

Conclusions

6.1 Summary of thesis

Hot stamping is a manufacturing process that is used to form ultra-high strength steels into lightweight, automotive body-in-white components. The quenching phase in hot stamping allows steel blanks, typically Al-Si coated 22MnB5 alloy, to be formed and hardened in a single punch-stroke. The superior mechanical properties of these parts allow for thinner cross-sections compared to high-strength low alloy (HSLA) steels, without sacrificing crash protection. This leads to improved fuel economy and reduced greenhouse emissions of fossil fuel vehicles, and extended driving range of electric vehicles.

The HTC is a critical parameter in the design and development of automotive hot stamping operations since it governs the quenching rate and therefore the final mechanical properties of the part. However, reliable estimates of this parameter are elusive since it relies on interfacial parameters that cannot be measured directly, and are instead inferred from temperature measurements made away from the interface. Most values reported in the literature are calculated assuming that: (1) the blank is thermally-lumped, (2) the die thermocouple measurement indicates the die temperature at a prescribed depth and time, (3) the instantaneous interfacial pressure corresponds to the press loading divided by the interface area, and (4) the pressure is uniform across the interface.

The present experimental work examines the veracity of these assumptions and their impact on the HTC. Accounting for the response delay of the thermocouple probe inside the die increased the time-averaged HTC prior to martensite formation by up to 31%. Using the midplane temperature of the blank as opposed to the surface temperature underestimated

the HTC by up to 16% since the validity of modelling the blank as a thermally lumped mass breaks down at higher HTCs. These results highlight the importance of correcting the temporal delay of the thermocouple probe and considering the temperature distribution within the blank to estimate the HTC accurately.

While increasing the pressure from 0.2 to 4.5 MPa increased the time-averaged HTC, the increase in HTC appeared to saturate at pressures beyond 4.5 MPa, which is considerably lower than the 10 MPa saturation pressure reported in the literature. The source of this discrepancy was attributed to higher interfacial pressures near the blank periphery due to a cantilever effect. This effect also explained the diminishing trends in the time-averaged HTCs from 4.5 to 40 MPa.

In terms of model development, the present experiment showed that the HTC increased in two distinct stages during quenching. The first stage was driven by a gradual increase in the press tonnage. The second stage of the HTC increase was attributed to the austenite to martensite phase transformation that begins when the blank cools to 400°C. Comparing the surface topography of the unpressed and pressed regions of fully-quenched blanks via an optical microscope showed the pressed regions have a permanently smoother surface, suggesting that the microaspteries of the blank experience plastic deformation during quenching. Surface topography measurements also revealed trends between the Al-Si coating thickness and HTC, but were inconclusive since the pressure distribution between the blank and die was non-uniform in the present work.

A physics-based model was developed to predict and explain the time-resolved HTC. The surface topography measured by the optical microscope in the unpressed region of a fully-quenched blank was used to capture the initial imperfect contact between the blank and die. The model was implemented using an explicit finite difference scheme to solve the heat diffusion equation, and the Norton-Hoff constitutive law to model deformation of blank surface asperities from the force applied by the die while capturing the effects of temperature on material behavior.

The model captured the two-stage increase of the HTC observed in the experiment and made predictions within the same order of magnitude as the experimentally measured time-average HTCs at higher interfacial pressures. However, the present model did not capture the “saturation” behavior of the HTC to increasing pressures; instead, the modelled HTCs continued to increase with increasing pressure, suggesting that the interfacial contact area also continue to increase with increasing pressure. This nonphysical result was attributed to the uniaxial compression assumption of asperity peaks employed in the mechanical submodel. In reality, there are bond/friction forces and interactions between neighboring asperities that may impose a maximum limit on the real area of contact, causing the HTC

to plateau at higher pressures. This may also be the reason why analytical models (e.g., CMY model) are unable to predict an upper limit on the HTC.

The present model showed that the lower thermal conductivity of the intermetallic layer relative to 22MnB5 and inhomogeneity of the blank surface can have a substantial impact on the HTC. These findings partially explained why the CMY model implemented by Caron et al. [30] overpredicted the HTC. The HTC overprediction by the CMY model was also attributed to the presumption that surface deviations about the mean plane follow a Gaussian distribution when in fact the surface height distribution of austenitized blanks generally favoured high peaks. Furthermore, the present model shows that latent heat increases the HTC slightly by increasing the thermal conductivity of the intermetallic layer, and the effect of increasing thermal conductivity of the 22MnB5 substrate is negated by the intermetallic coating. The model also shows that virtually all process parameters in hot stamping (e.g., press tonnage ramp up duration, initial blank thickness, and initial temperature of the blank and die) have a significant effect on the HTC because of the highly coupled nature of the thermal field and mechanical behavior of the blank.

6.2 Future work and recommendations

6.2.1 Improving experimental apparatus

The investigation of two modifications on the experimental method is recommended to improve the accuracy of the results and efficiency of the procedure. One modification is to match the footprint between the blank and die to eliminate the elastic cantilever bending experienced by the die, and the resulting nonuniform interfacial pressure. This will likely increase the pressure at which the HTC starts to become insensitive to further increments in pressure to a value much closer to what is often reported in the literature.

Another modification is to test the feasibility of using a high-speed IR camera to measure the cross-sectional temperature field of the blank and die normal to the quenching surface. An example of the proposed experimental apparatus is shown in Figure 6.1, which was adopted by Burghold et al. [74] to infer the HTC history between two medium carbon steel specimens. If feasible, the distribution of surface heat flux and HTC may be observable. The IR camera would also eliminate the requirement of having to mill a slot within the blank and instrumenting a K-type thermocouple via welding. This would substantially increase the number of trials that may be tested due to the simplicity of the sample preparation, and opens the possibility of using a robot to transfer the austenitized blank from

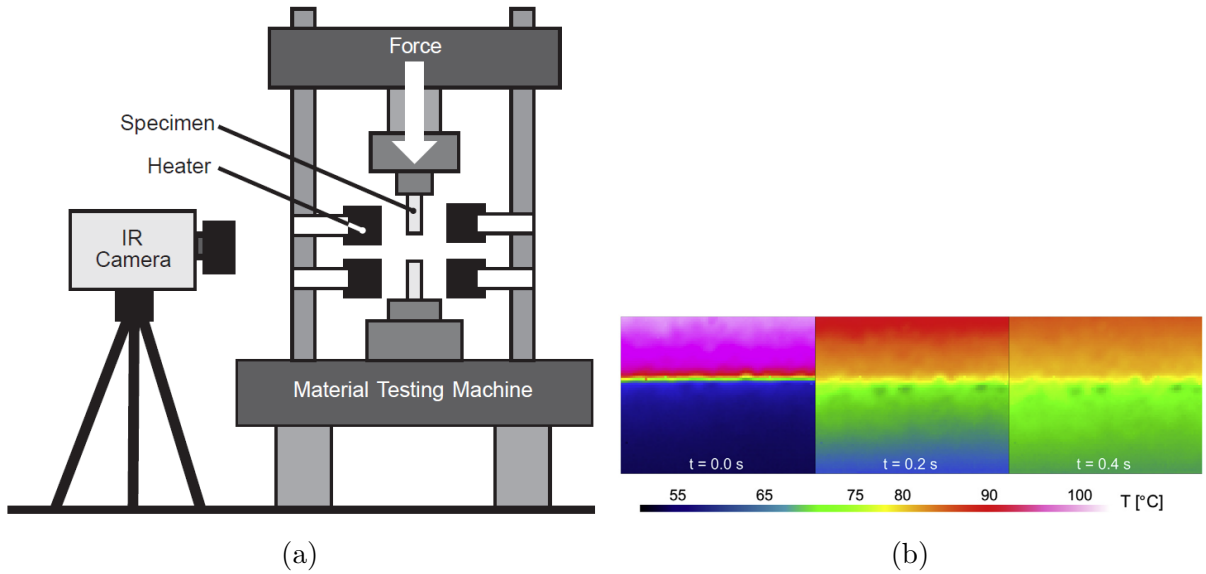


Figure 6.1: (a) Experimental apparatus for inferring transient HTC between two medium carbon steel specimens [74] and (b) temperature field at the interface measured by the IR camera [57].

the furnace to the press for more consistent and faster transfer times. This concept was attempted in the present study by using an IR thermometer to measure the blank surface temperature but did not work as intended because the access port required through the die led to overestimation of the blank surface temperature.

6.2.2 Model development

Several changes to the model may improve the agreement between the predicted and measured HTCs. One change is to use the deformation behavior of Al-Fe-Si intermetallic instead of 22MnB5, since the microasperities that deform are primarily made of the former material. However, obtaining the deformation behavior of Al-Fe-Si would likely require a novel technique because of the lack of literature involving this material and its brittle characteristics. Another modification is to model the deformation of the microasperities such that the deformation limit of the intermetallic compound is accounted for instead of assuming uniaxial compression, which may allow the model to predict the insensitivity of the HTC to higher pressures. The effects of elastic deformation and thermal contraction of the 22MnB5 substrate on the HTC should also be accounted for and investigated using

the model.

Another area for improving the HTC model is related to the press controller latency factor that was implemented to account for deformation of the asperities due to the delayed reaction of the press controller as the blank thickness increases. The model predictions may be improved by accounting for the dynamics of the control system and hydraulic actuators as opposed to using a constant factor. This change would require force output data that is measured during the quenching phase and insight regarding the control logic of the press controller from its manufacturer.

While the present study focused on building the theoretical foundation explaining the HTC evolution in flat-die hot stamping, both the experimental and modelling aspects may be expanded to account for large scale deformation in the forming of complex geometries (e.g., “ Ω ” shaped parts like the B-pillar). This would enable a detailed investigation of how the friction between the blank and die, as well as the heat released from plastic deformation, affects the HTC. The prominence of friction opens the door to detailed investigations about the effect of lubricants designed to extend the wear life of tool surfaces [28, 29]. The effect of the angle between the blank surface and the direction of the applied force on the surface state and HTC may also be studied. The present work also serves as a foundation for a unified hot stamping model that predicts everything that happens to the Al-Si coated 22MnB5 steel as it progresses from the as-received state to the as-formed part.

References

- [1] I. O. of Motor Vehicle Manufacturers, “Production statistics.” <https://www.oica.net/category/production-statistics/>. Accessed: 2022-10-13.
- [2] P. Åkerström, *Modelling and Simulation of Hot Stamping*. PhD thesis, Luleå University of Technology, Luleå, 2006.
- [3] I. Wróbel, A. Skowronek, and A. Grajcar, “A review on hot stamping of advanced high-strength steels: Technological-metallurgical aspects and numerical simulation,” *Symmetry*, vol. 14, no. 5, p. 969, 2022.
- [4] H. Karbasian and A. E. Tekkaya, “A review on hot stamping,” *J. Mater. Process. Technol.*, vol. 210, no. 15, pp. 2103–2118, 2010.
- [5] E. Billur, “PHS in vehicles: An abridged history.” <https://ahssinsights.org/blog/phs-in-automotive-applications-an-abridged-history/>. Accessed: 2022-10-13.
- [6] E. Billur, *Hot Stamping of Ultra High-Strength Steels: From a Technological and Business Perspective*. Springer International Publishing, 2019.
- [7] M. Merklein and J. Lechler, “Determination of material and process characteristics for hot stamping processes of quenchenable ultra high strength steels with respect to a FE-based process design,” *SAE Int. J. Mater. Manf.*, vol. 1, no. 1, pp. 411–426, 2009.
- [8] H. Liu, C. Lei, and Z. Xing, “Cooling system of hot stamping of quenchable steel BR1500HS: Optimization and manufacturing methods,” *The International Journal of Advanced Manufacturing Technology*, vol. 69, no. 10, p. 2103, 2013.
- [9] K. Mori, S. Maki, and Y. Tanaka, “Warm and hot stamping of ultra high tensile strength steel sheets using resistance heating,” *CIRP Annals*, vol. 54, no. 1, pp. 209–212, 2005.

- [10] M. T. Inc., “Hot stamping 101.” <https://macrodynepress.com/hot-stamping-101/>. Accessed: 2022-10-13.
- [11] “Arcelormittal, steels for hot stamping – Usibor and Ductibor.” https://automotive.arcelormittal.com/products/flat/PHS/usibor_ductibor. Accessed: 2022-06-22.
- [12] A. Tekkaya, H. Karbasian, W. Homberg, and M. Kleiner, “Thermomechanical coupled simulation of hot stamping components for process design,” *Production Engineering*, vol. 1, pp. 85–89, 08 2007.
- [13] A. Polozine and L. Schaeffer, “Influence of the inaccuracy of thermal contact conductance coefficient on the weighted-mean temperature calculated for a forged blank,” *Journal of Materials Processing Technology*, vol. 195, no. 1, pp. 260–266, 2008.
- [14] M. Naderi, *Hot Stamping of Ultra High Strength Steels*. PhD thesis, RWTH Aachen University, Templergraben 55, 52062 Aachen, Germany, 2007.
- [15] D. C. William Jr. and D. G. Rethwisch, *Materials Science and Engineering*. John Wiley and Sons, 2014.
- [16] Y. Chang, X. Tang, K. Zhao, P. Hu, and Y. Wu, “Investigation of the factors influencing the interfacial heat transfer coefficient in hot stamping,” *J. Mater. Process. Technol.*, vol. 228, pp. 25–33, 2016.
- [17] B. Abdulhay, B. Bourouga, and C. Dessain, “Thermal contact resistance estimation at the blank/tool interface: experimental approach to simulate the blank cooling during the hot stamping process,” *Int. J. Mater. Form.*, vol. 3, no. 3, pp. 147–163, 2010.
- [18] R. George, A. Bardelcik, and M. Worswick, “Localized die temperature control for tailored properties in hot forming of boron steels - numerical study,” in *International Deep Drawing Research Group*, 2009.
- [19] D. W. Fan and B. C. De Cooman, “State-of-the-knowledge on coating systems for hot stamped parts,” *steel research international*, vol. 83, no. 5, pp. 412–433, 2012.
- [20] F. Borsetto, A. Ghiotti, and S. Bruschi, “Investigation of the high strength steel Al-Si coating during hot stamping operations,” in *Sheet Metal 2009*, vol. 410 of *Key Engineering Materials*, pp. 289–296, Trans Tech Publications Ltd, 10 2009.

- [21] P. Hu, L. Ying, Y. Li, and Z. Liao, “Effect of oxide scale on temperature-dependent interfacial heat transfer in hot stamping process,” *J. Mater. Process. Technol.*, vol. 213, no. 9, pp. 1475–1483, 2013.
- [22] D. W. Fan, H. S. Kim, and B. C. De Cooman, “A review of the physical metallurgy related to the hot press forming of advanced high strength steel,” *steel research international*, vol. 80, no. 3, pp. 241–248, 2009.
- [23] K. Ji, O. E. Fakir, H. Gao, and L. Wang, “Determination of heat transfer coefficient for hot stamping process,” *Materials Today: Proceedings*, vol. 2, pp. S434–S439, 2015.
- [24] C. M. Klassen and K. J. Daun, “Investigating coating liquefaction and solidification of furnace-heated Al-Si coated 22MnB5 steel using laser reflectance,” *Surface and Coatings Technology*, vol. 393, p. 125795, 2020.
- [25] C. Shi, K. J. Daun, and M. A. Wells, “Spectral emissivity characteristics of the Usibor 1500P steel during austenitization in argon and air atmospheres,” *International Journal of Heat and Mass Transfer*, vol. 91, pp. 818–828, 2015.
- [26] C. Shi, K. Daun, and M. Wells, “Evolution of the spectral emissivity and phase transformations of the Al-Si coating on Usibor 1500P steel during austenitization,” *Metallurgical and Materials Transactions B*, vol. 47, 08 2016.
- [27] C. Klassen, J. Emmert, and K. Daun, “Effect of coating thickness on the in-situ reflectance and surface roughness of Al-Si coated 22MnB5 steel,” *Surface and Coatings Technology*, vol. 414, p. 127100, 2021.
- [28] A. Hamasaiid, M. S. Dargusch, C. J. Davidson, S. Tovar, T. Loulou, F. Rezaí-Aria, and G. Dour, “Effect of mold coating materials and thickness on heat transfer in permanent mold casting of aluminum alloys,” *Metall. Mater. Trans. A*, vol. 38, no. 6, pp. 1303–1316, 2007.
- [29] X. Liu, O. E. Fakir, M. M. Gharbi, and L. Wang, “Effect of tool coating on interfacial heat transfer coefficient in hot stamping of AA7075 aluminium alloys,” *Procedia Manufacturing*, vol. 15, pp. 1127–1133, 2018. Proceedings of the 17th International Conference on Metal Forming METAL FORMING 2018 September 16 – 19, 2018, Loisir Hotel Toyohashi, Toyohashi, Japan.
- [30] E. Caron, K. J. Daun, and M. A. Wells, “Experimental characterization of heat transfer coefficients during hot forming die quenching of boron steel,” *Metall. Mater. Trans. B*, vol. 44, no. 2, pp. 332–343, 2013.

- [31] M. Merklein, J. Lechler, and T. Stoehr, "Investigations on the thermal behavior of ultra high strength boron manganese steels within hot stamping," *Int. J. Mater. Form.*, vol. 2, no. Suppl 1, pp. 259–262, 2009.
- [32] K. Omer, C. Butcher, and M. Worswick, "Characterization of heat transfer coefficient for non-isothermal elevated temperature forming of metal alloys," *Int. J. Mater. Form.*, vol. 13, no. 2, pp. 177–201, 2020.
- [33] B. Abdulhay, B. Bourouga, and C. Dessain, "Experimental and theoretical study of thermal aspects of the hot stamping process," *Applied Thermal Engineering*, vol. 31, pp. 674–685, 04 2011.
- [34] B. Abdulhay, B. Bourouga, and C. Dessain, "Thermal contact resistance estimation: Influence of the pressure contact and the coating layer during a hot forming process," *International Journal of Material Forming*, vol. 5, pp. 1–15, 09 2011.
- [35] P. Salomonsson and M. Oldenburg, "Investigation of heat transfer in the press hardening process," in *Proceedings of Hot Sheet Metal Forming of High-Performance Steel (CHS²): 2nd International Conference*, 2009.
- [36] L. Pelcastre, E. Kurnia, J. Hardell, J. Decrozant-Triquenau, and B. Prakash, "High temperature tribological studies on hardfaced tool steels for press hardening of Al-Si coated boron steel," *Wear*, vol. 476, 2021.
- [37] G. Xiao and Z. Zan, "Determination of interfacial heat transfer coefficient of 22MnB5 boron steel in hot forming based on inverse heat transfer method," *IOP Conf. Ser.: Earth Environ. Sci.*, vol. 692, no. 2, 2021.
- [38] S. Wen, Z. Chen, S. Qu, J. J. Tang, and X. Han, "Investigations on the interfacial heat transfer coefficient during hot stamping of ultra-high strength steel with Al-Si coating," *Int. J. Heat Mass Transf.*, vol. 189, 2022.
- [39] P. Bosetti, S. Bruschi, T. Stoehr, J. Lechler, and M. Merklein, "Interlaboratory comparison for heat transfer coefficient identification in hot stamping of high strength steels," *Int. J. Mater. Form.*, vol. 3, no. Suppl 1, pp. 817–820, 2010.
- [40] Z.-W. Gu, M.-M. Lv, G.-H. Lu, H. Xu, and X. Li, "Heat transfer coefficient evolution of boron steel during hot forming die quenching," *Mater. Sci. Technol.*, vol. 32, no. 2, pp. 173–180, 2016.

- [41] T.-H. Hung, P.-W. Tsai, F.-K. Chen, T.-B. Huang, and W.-L. Liu, "Measurement of heat transfer coefficient of boron steel in hot stamping," *Procedia Engineering*, vol. 81, pp. 1750–1755, 2014. 11th International Conference on Technology of Plasticity, ICTP 2014, 19-24 October 2014, Nagoya Congress Center, Nagoya, Japan.
- [42] M. Wang, C. Zhang, H. Xiao, and B. Li, "Inverse evaluation of equivalent contact heat transfer coefficient in hot stamping of boron steel," *Int. J. Adv. Manuf. Technol.*, vol. 87, no. 9-12, pp. 2925–2932, 2016.
- [43] X. Liu, O. El Fakir, Z. Cai, B. Dalkaya, K. Wang, M. M. Gharbi, and L. Wang, "Development of an interfacial heat transfer coefficient model for the hot and warm aluminium stamping processes under different initial blank temperature conditions," *Journal of Materials Processing Technology*, vol. 273, p. 116245, 2019.
- [44] Z. Zhang, P. Gao, C. Liu, and X. Li, "Experimental and simulation study for heat transfer coefficient in hot stamping of high-strength boron steel," *Metallurgical and Materials Transactions B*, vol. 46, 09 2015.
- [45] K. Zhao, B. Wang, Y. Chang, X. Tang, and J. Yan, "Comparison of the methods for calculating the interfacial heat transfer coefficient in hot stamping," *Appl. Therm. Eng.*, vol. 79, pp. 17–26, 2015.
- [46] Y. Li, S. Li, J. He, Y. Chen, and L. Yue, "Identification methods on blank-die interfacial heat transfer coefficient in press hardening," *Appl. Therm. Eng.*, vol. 152, pp. 865–877, 2019.
- [47] G. A. Franco, E. Caron, and M. A. Wells, "Quantification of the surface temperature discrepancy caused by subsurface thermocouples and methods for compensation," *Metall. Mater. Trans. B*, vol. 38B, pp. 949–956, 2007.
- [48] A. R. Singh, A. S. Bhattacharya, C. Butcher, and K. J. Daun, "Experimental artefacts affecting characterization of the evolving interfacial heat transfer coefficient in hot stamping of Al-Si coated 22MnB5 steel," *Applied Thermal Engineering*, 2023.
- [49] M. M. Yovanovich, "Four decades of research on thermal contact, gap, and joint resistance in microelectronics," *IEEE Transactions on Components and Packaging Technologies*, vol. 28, no. 2, pp. 182–206, 2005.
- [50] C. V. Madhusudana, *Thermal Contact Conductance*. Springer, 2013.

- [51] M. G. Cooper, B. B. Mikic, and M. M. Yovanovich, “Thermal contact conductance,” *International Journal of Heat and Mass Transfer*, vol. 12, pp. 279–300, 03 1969.
- [52] B. B. Mikić, “Thermal contact conductance; theoretical considerations,” *International Journal of Heat and Mass Transfer*, vol. 17, no. 2, pp. 205–214, 1974.
- [53] M. Yovanovich, “Thermal contact correlations,” in *Proceedings of the Seventh Conference on Thermal Conductivity*, 1981.
- [54] C. L. Tien, “Correlation for thermal contact conductance of nominally-flat surfaces in a vacuum,” in *Proceedings of the Seventh Conference on Thermal Conductivity*, 1967.
- [55] B. Snaith, S. D. Probert, and P. W. O’Callaghan, “Thermal resistances of pressed contacts,” *Applied energy*, vol. 22, no. 1, pp. 31–84, 1986.
- [56] Y. P. Shlykov and E. A. Ganin, “Thermal contact resistance,” *The Soviet Journal of Atomic Energy*, vol. 9, p. 1041–1043, 1961.
- [57] Y. Frekers, T. Helmig, E. M. Burghold, and R. Kneer, “A numerical approach for investigating thermal contact conductance,” *International Journal of Thermal Sciences*, vol. 121, pp. 45–54, 11 2017.
- [58] M. V. Murashov and S. D. Panin, “Numerical modelling of contact heat transfer problem with work hardened rough surfaces,” *International Journal of Heat and Mass Transfer*, vol. 90, pp. 72–80, 2015.
- [59] A. T. Vu, T. Helmig, A. N. Vu, Y. Frekers, T. Grunwald, R. Kneer, and T. Bergs, “Numerical and experimental determinations of contact heat transfer coefficients in nonisothermal glass molding,” *Journal of the American Ceramic Society*, vol. 103, no. 2, pp. 1258–1269, 2020.
- [60] A. R. Singh, C. Butcher, and K. J. Daun, “Characterizing the heat transfer coefficient in the hot stamping of Al-Si coated 22MnB5 steel,” in *CHS²*, 2022.
- [61] A. R. Singh, C. Butcher, and K. J. Daun, “Improving the accuracy of experimentally inferred heat transfer coefficients for hot stamping,” in *Summer Heat Transfer Conference by ASME*, 2023.
- [62] R. George, “Details about how the Macrodyne press works,” June 2022. Interview.
- [63] T. L. Bergman, A. S. Lavine, F. P. Incropera, and D. P. DeWitt, *Fundamentals of Heat and Mass Transfer*. Hoboken, NJ: Wiley, 2007.

- [64] J. V. Beck, B. Blackwell, and C. R. St Clair Jr., *Inverse Heat Conduction: Ill-Posed Problems*. New York, NY: Wiley-Interscience, 1985.
- [65] D. P. Koistinen and R. E. Marburger, “A general equation prescribing the extent of the austenite-martensite transformation in pure iron-carbon alloys and plain carbon steels,” *Acta Metall.*, vol. 7, no. 1, pp. 59–60, 1959.
- [66] Veeco, “Wyko NT1100 optical profiling system.” <https://anff-q.org.au/wp-content/uploads/2016/07/3D-optical-profiler-Veeco-Wyko-NT1100.pdf>. Accessed: 2022-10-09.
- [67] P. Pavliček and O. Hýbl, “White-light interferometry on rough surfaces – measurement uncertainty caused by noise,” *Appl. Opt.*, vol. 51, pp. 465–473, Feb 2012.
- [68] Keyence, “Digital microscope VHX-5000.” <https://www.simac.com/uploads/media/57b18417dea69/keyence-vhx5000.pdf>. Accessed: 2022-10-09.
- [69] D. J. Whitehouse, *Surfaces and their Measurement*. London: HPS, 2002.
- [70] B. V. Reddy and S. C. Deevi, “Thermophysical properties of FeAl (Fe-40 at.% Al),” *Intermetallics*, vol. 8, no. 12, pp. 1369–1376, 2000.
- [71] L. Cho, L. Golem, E. J. Seo, D. Bhattacharya, J. G. Speer, and K. O. Findley, “Microstructural characteristics and mechanical properties of the Al-Si coating on press hardened 22MnB5 steel,” *Journal of Alloys and Compounds*, vol. 846, p. 156349, 2020.
- [72] C. P. Couto, R. I. Revilla, M. A. Colosio, I. Costa, Z. Panossian, I. De Graeve, H. Terryn, and J. L. Rossi, “Electrochemical behaviour of 22MnB5 steel coated with hot-dip Al-Si before and after hot-stamping process investigated by means of scanning kelvin probe microscopy,” *Corrosion Science*, vol. 174, p. 108811, 2020.
- [73] M. Naderi, L. Durrenberger, A. Molinari, and W. Bleck, “Constitutive relationships for 22MnB5 boron steel deformed isothermally at high temperatures,” *Materials Science and Engineering: A*, vol. 478, no. 1, pp. 130–139, 2008.
- [74] E. Burghold, Y. Frekers, and R. Kneer, “Determination of time-dependent thermal contact conductance through IR-thermography,” *International Journal of Thermal Sciences*, vol. 98, pp. 148–155, 12 2015.

- [75] TENAQUIP, “Lifting swivel hoist rings, M16, 35 mm thread length, alloy steel.” <https://www.tenaquip.com/product/vanguard-steel-lifting-swivel-hoist-rings-m16-35-mm-thread-length-alloy-steel-2978-21635-lu823>. Accessed: 2022-10-12.
- [76] D. Day, *The GD&T Hierarchy Y14.5-2009*. Tec-Ease Inc., 01 2009.

APPENDICES

Appendix A

Design of Experimental Apparatus

The design criteria for the upper and lower dies are listed as follows:

1. Dies must have features that allow it to easily mount to the large Macrodyne press.
2. Dies must be thick enough such that the surface temperature opposite of quench surface does not increase change significantly during a 20 s quenching period.
3. Dies must be safe to handle and maneuver by two people.
4. Dies must have holes that allow subsurface thermocouples to be accurately positioned.
5. Upper die must have a mounting solution for the infrared (IR) thermometer's tip.

A.1 Die Features for Fastening on Large Macrodyne Press

The upper and lower dies were made of AISI 4140 steel with a 304.8 mm \times 304.8 mm (1 ft \times 1 ft) footprint. Figure [A.1a](#) shows the upper die from the point of view of the blank and through it are 10 untapped holes near the periphery, which are also present in the lower die. Six of the holes are counter-bored to allow socket head cap screws, as shown in Figure [A.1b](#), to secure the die to the aluminum cooling plate. Making the dies any smaller would undercutting the holes for the screws while making the die any larger would make them unnecessarily heavy.

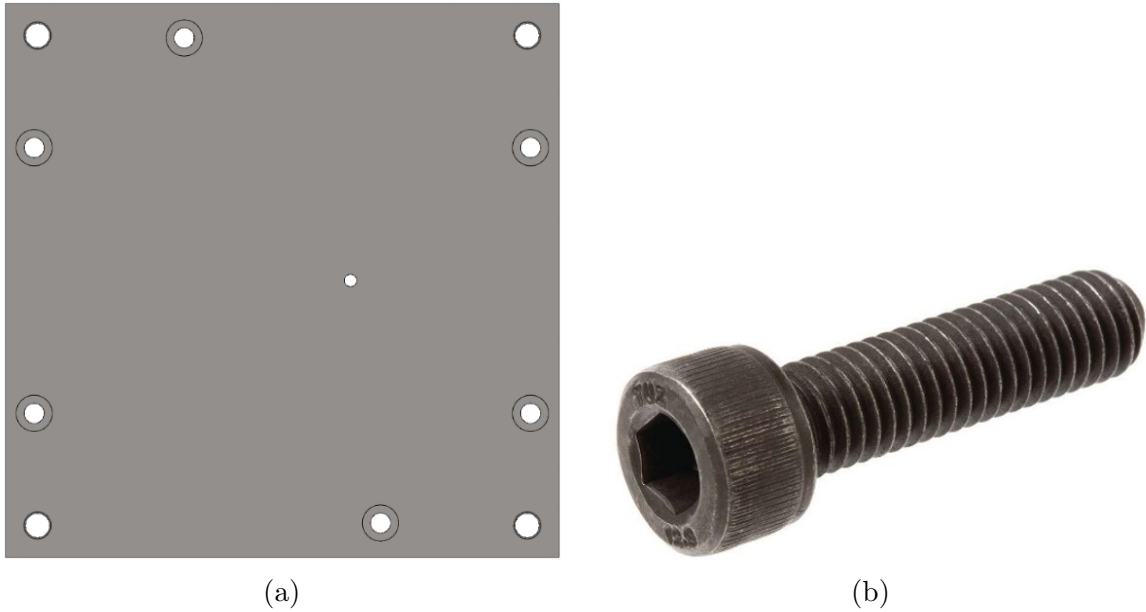


Figure A.1: (a) View of upper die from perspective of blank and (b) shoulder screw (McMaster-Carr M10×1.5×90 91290A546) used to secure dies to aluminum cooling plate.

The four holes at the corners of the dies are for the guide pins that protrude from the aluminum cooling plate. The guide pins are essential for deep drawing experiments to ensure the punch remains aligned even after distortions caused by thermal expansion. For the flat-die hot stamping experiment, the guide pins are not required. However, the holes were added anyways so that the guide pins do not need to be removed nor added repeatedly. The hole near the middle of the upper die in Figure A.1a is an access port for the IR thermometer.

A.2 Spring Lifter Slots on Lower Die

Figure A.2a shows the lower die from the perspective of the blank and highlighted in blue are the four slots for the spring lifters. The spring lifter shown in Figure A.2b is an existing design that is available off the shelf in the Forming and Crash Laboratory. The spring lifters help locate the austenitized blank on to the lower die and prevent the blank from touching the lower die to avoid premature quenching during the approach phase of the upper die. The slots are compatible with blank sizes between 150 mm × 150 mm and 170 mm × 170 mm. Note that the blank need not have equal side lengths.

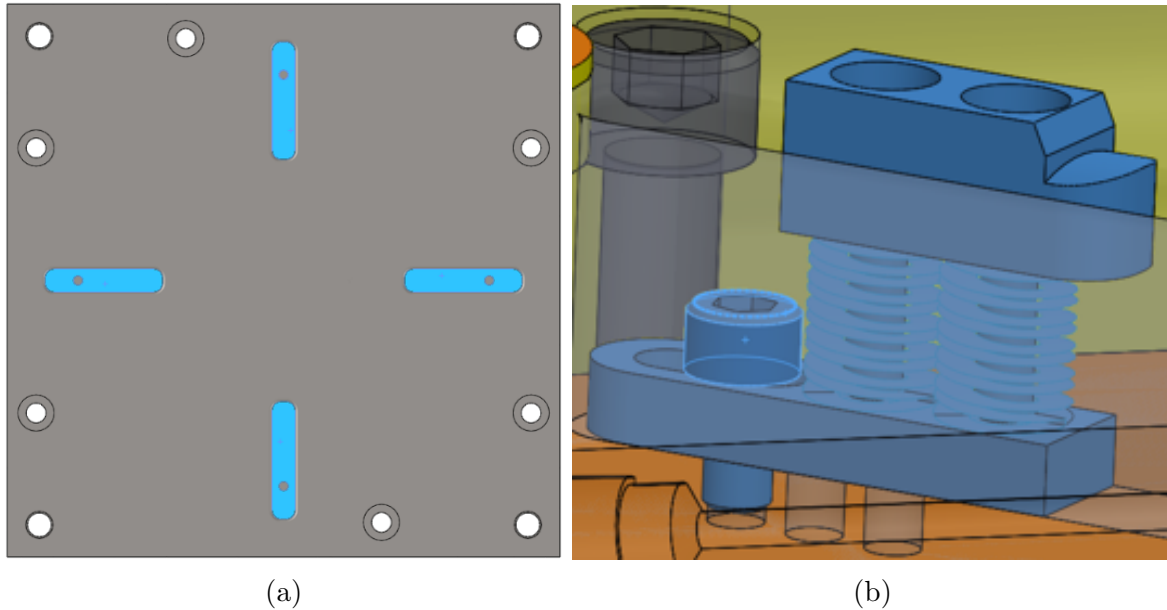


Figure A.2: (a) View of lower die from perspective of blank and (b) spring lifter assembly.

A.3 Determining Die Thickness via Finite Element Simulations

Transient, 3D FE simulations were conducted on ANSYS Mechanical to optimize the thickness of the dies. On one hand, the die must be sufficiently thick so that an adiabatic boundary condition holds true opposite of the quenching surface. This is necessary in order to infer the surface heat flux from subsurface temperature measurements using inverse heat conduction analysis, which assumes the die is a semi-infinite solid. On the other hand, the die must not be excessively thick or else it will be too heavy and unsafe for two people to lift and maneuver it. The results of the FE simulations led to a die thickness of 65 mm. The remainder of this section discusses the setup and results of the FE simulations.

DesignModeller was used to generate the geometry of the domain. Heat transfer was assumed to be symmetric at all three midplanes; hence, only $1/8^{\text{th}}$ of the total domain was modelled as shown in Figure A.3. A 0.1 mm gap exists between the blank and the die. Although the expected blank size will likely be $150 \text{ mm} \times 150 \text{ mm} \times 1.5 \text{ mm}$, the blank dimensions in the FE model were set to $170 \text{ mm} \times 170 \text{ mm} \times 2.4 \text{ mm}$ to be conservative. The thermophysical properties of the AISI 4140 die and 22MnB5 blank are summarized in Table 2.1.

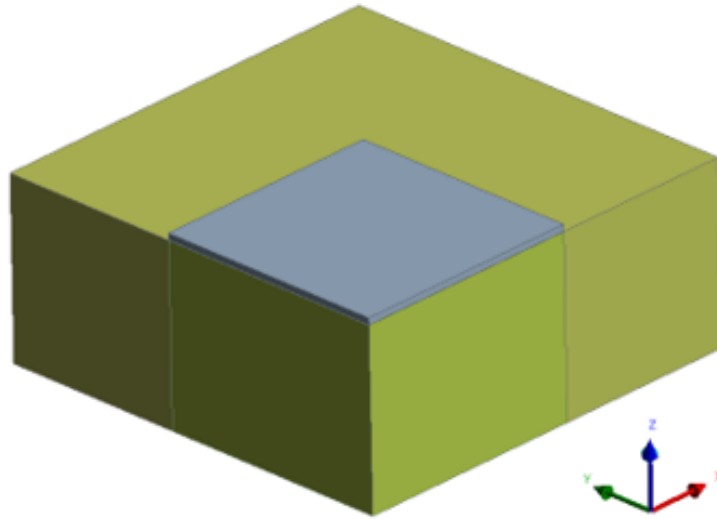


Figure A.3: Domain of blank (grey) and die (green).

The simplified domain (e.g., holes and slots omitted) enabled the use of a relatively coarse, hexahedral mesh, making the analysis computationally inexpensive. Referring to Figure A.4, the main features of the mesh are:

1. The z direction element size starts out small at the quenching surface and expands linearly away from the quenching surface.
2. The thickness of the blank is divided into three evenly sized elements.
3. The elements in the die and blank are aligned on planes parallel to the xy -plane.
4. RMS differences in temperature profiles across the die thickness decreased as the element count increased (13,218, 27,378 and 38,610 elements), signifying mesh independent results. The following discussion is based on the mesh with 27,378 elements.

The physical duration of the transient analysis was set to 20 s. While this is longer than typical quenching times, it is anticipated that a 20-s hold time will be employed to ensure the quenched blank is safe to handle by hand. There may be noteworthy observations in the HTC evolution at the later stages, which is why it is desirable to maintain semi-infinite conditions for the entire 20 s. The time step size is program controlled between 1×10^{-3} and 0.1 s. The surfaces exposed to ambient air, as well as the surface opposite to the quenching surface are modelled as a perfectly insulated. A separate analysis revealed the effects of

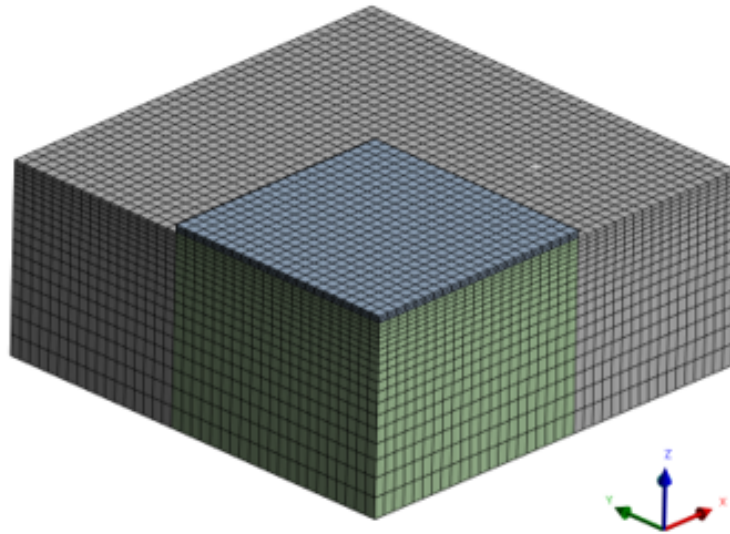


Figure A.4: Mesh used for thermal FE simulations.

convection and radiation on the temperature field are negligible. The HTC between the blank and die was set to $8 \text{ kW}/(\text{m}^2\text{K})$, which is a high-end estimate for interfacial pressures of 40 MPa as per models and experimental measurements [32, 41]. Additional details about the contact modelling between the blank and die are shown Figure A.5.

ANSYS Mechanical by default does not offer an option to set unique initial temperatures for each subdomain. An ANSYS Parametric Design Language (APDL) command had to be entered to set the initial condition of the blank to 930°C and the die to 22°C . The APDL command is

```
IC, Blank, TEMP, 930  
IC, Die, TEMP, 22
```

where **Blank** and **Die** are named selections assigned to their respective subdomains. For sample results, contour plots for temperature are shown in Figure A.6.

Several die thicknesses were tested at 5 mm increments. The die with a 65 mm thickness behaved like a near-perfect semi-infinite solid for the entire 20 s analysis. At the 20-s mark, the surface temperature opposite of the quenching surface had risen by 1.2°C only, which is a negligible change. The weight of a 65 mm thick die is approximately 100 lbs. While this is an acceptable load for two people to carry, the shape of the die makes it an unsafe task. To solve this issue, four $\text{M}12 \times 1.75$ threaded holes were included in the side walls of

Details of "Contact Region 2"	
Scope	
Scoping Method	Geometry Selection
Contact	1 Face
Target	1 Face
Contact Bodies	Solid
Target Bodies	Solid
Protected	No
Definition	
Type	Bonded
Scope Mode	Automatic
Behavior	Asymmetric
Trim Contact	Program Controlled
Trim Tolerance	5.6462e-004 m
Suppressed	No
Display	
Element Normals	No
Advanced	
Formulation	Pure Penalty
Small Sliding	Program Controlled
Detection Method	Program Controlled
Elastic Slip Tolerance	Program Controlled
Thermal Conductance	Manual
Thermal Conductance Value	8000. W/m ² ·°C
Pinball Region	Program Controlled
Geometric Modification	
Contact Geometry Correction	None
Target Geometry Correction	None

Figure A.5: Contact modelling between the blank and die.

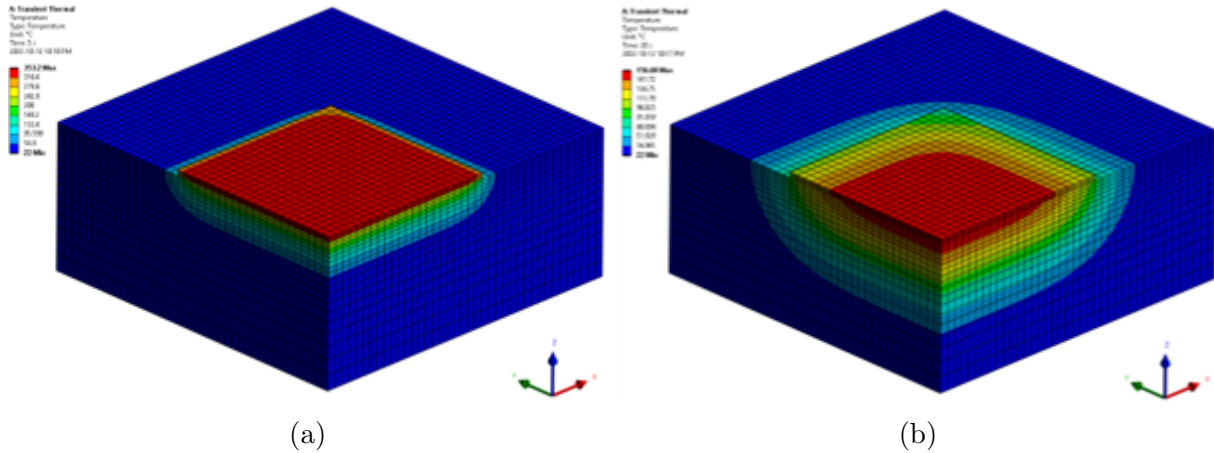


Figure A.6: Temperature field of die at (a) $t = 0$ s and (b) $t = 20$ s.

each die (i.e., surfaces orthogonal to the quenching surface) to accommodate lifting rings as shown in Figure A.7.

A.4 Finite Element Verification

To verify the FE simulations, experiments from past research were modelled into ANSYS Mechanical. The domain, initial condition, and HTC resulting from applied pressure were consistent with the source, but all other set up parameters are identical to the description in the previous section. The heat flux is compared against Caron et al.'s [30] measurements in Figure A.8a while surface temperatures are compared against Hung et al.'s [41] measurements in Figure A.8b. Despite the assumption of a constant HTC throughout the transient analysis, the FE results compare very well with experimental measurements.

A.5 Thermocouple Probe

The upper and lower dies each accommodate two K-type thermocouple probes that are inserted from the side that mates against the aluminum cooling plate. The two thermocouple probes measure the subsurface and far-field temperature histories 1.5 mm and 20 mm below the quenching surface, respectively. The subsurface temperature history is used for inverse heat conduction analysis while the far-field temperature is used for verification



Figure A.7: Lifting ring for manually handling dies [75].

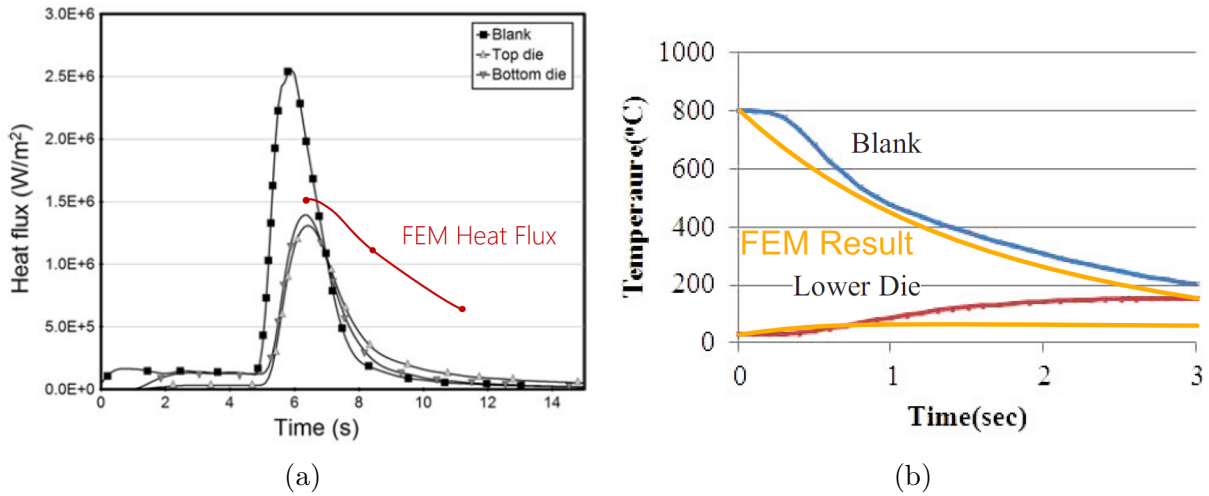


Figure A.8: (a) FE predicted surface heat flux compared to measurements by Caron et al. [30] and (b) FE predicted surface temperatures compared to measurements by Hu et al. [21].

purposes. Figure A.9 shows a section view of the thermocouple configuration in the lower die while Table A.1 provides the specifications of the thermocouple probe.

Compression fittings were used to mount the thermocouple probe to the dies with good thermal contact. The advantage with compression fittings is that they can be fixed at any point along the length of the thermocouple probe. The disadvantage is that once they are fixed, they cannot be moved.¹ Once the compression fitting is installed on the thermocouple, the thermocouple/compression fitting assembly is hand tightened into the die. Specifications of the compression fitting are provided in Table A.2.

The diameter of the holes in the dies for the thermocouple probes are 2.2 mm. It was assumed that the drill bit would have a standard 118°-point angle. To ensure the compression fittings are compatible with the dies, the initial 9 mm depth of the 2.2 mm-diameter holes will be a 1/8" national pipe thread (NPT) tapped hole. This NPT thread is tapered and is what leads to good thermal contact between the thermocouple probe end and measurement site.

¹Although the ferrule is pressed onto the thermocouple probe when the compression fitting is tightened, it can be cut off so that a new compression fitting can be installed.

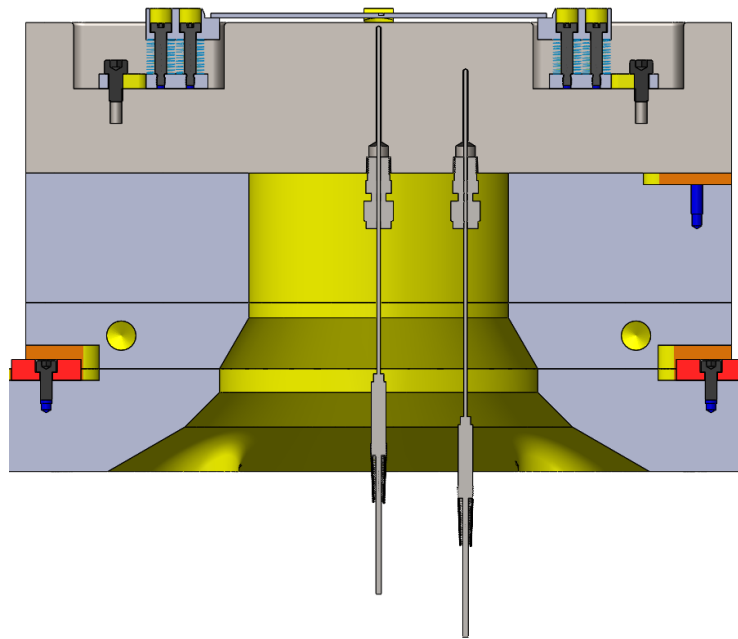


Figure A.9: Section view of lower die showing arrangement and mounting of thermcouple probe via compression fittings (arrangement mirrored in the upper die).

Table A.1: Thermocouple probe specifications.


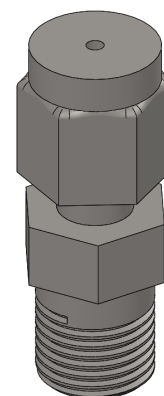
Supplier	OMEGA™	
Name	Thermocouple Probes with Molded Miniature Connectors	
Item #	KMQSS-062E-12	
Type	K	
Probe Length	12 in	
Probe Diameter	0.062 in	
Temperature Range	0 to 920°C	
Sheath Material	304 Stainless Steel	
Price	C\$ 69.57 each	
URL	https://www.omega.ca/en/temperature-measurement/temperature-probes/probes-with-integral-connectors/jmqss/p/KMQSS-062E-12	

Table A.2: Compression fitting specifications.

Supplier	OMEGA™
Name	OMEGALOK™ Adaptors, Fittings & Bushings
Item #	SSLK-116-18
Inner Diameter	1/16 in
Thread	1/8 in NPT
Length	~31 mm
Material	316 Stainless Steel
Price	C\$ 48.83 each
URL	https://www.omega.ca/en/pressure-measurement/pressure-measurement-accessories/pipe-and-tube-fittings/mta-brlk-sslk-ra-rb-series/p/SSLK-116-18




A.6 Infrared Thermometer

The use of an infrared (IR) thermometer was proposed early into the project to measure the surface temperature of the blank. The IR thermometer comprises two main components: an IR transmitter, and a ceramic encased tip assembly. The specifications of the two components are provided in Table A.3.

The upper die was designated to be compatible with the ceramic tip since there is more space in the back side of the upper die in comparison to the lower die. As shown in Figure A.10, a 6.7 mm access port was milled through the upper die to accommodate the 5-mm-diameter ceramic tip, along with a $M20 \times 2.5$ tapped hole for the tip adaptor. The tip adaptor (AISI 4140 steel) secures the IR thermometer's tip to the upper die in the same way the compression fittings secure the thermocouple probe. An $M20 \times 2.5$ locking nut secures the tip adaptor to the upper die, while two set screws thread into the tip adaptor to secure the ceramic tip.

The lower die, upper die, and tip adaptor were machined and manufactured by XL Tool Inc. in Kitchener, Ontario. Machining was based on information from the provided STEP files and engineering drawings. The engineering drawings follow the ASME Y14.5-2009

Table A.3: IR thermometer and ceramic tip specifications.

Supplier	OMEGA™	
Name	High Speed Fiber Optic Infrared Transmitter	
Item #	OS4001-V2	
Emissivity Range	0.05 to 0.99	
Temperature Range	150 to 1,600°C (tip assembly dependent)	
Input Power	15 to 24 VDC	
Output Signal	0 to 10 VDC	
Price	C\$ 2,220.00 each	
URL	https://www.omega.ca/en/temperature-measurement/noncontact-temperature-measurement/fixed-infrared-temperature-sensors/os4000-series/p/OS4001-V2	
Supplier	OMEGA™	
Name	Ceramic Encased Tip Assembly	
Item #	2610-Q-3-2650-3	
Temperature Range	250 to 1,000°C	
Price	C\$ 1,010.00 each	
URL	https://www.omega.ca/en/wire-and-cable/multiconductor-cable/p/2610-Q-3-2650-3	

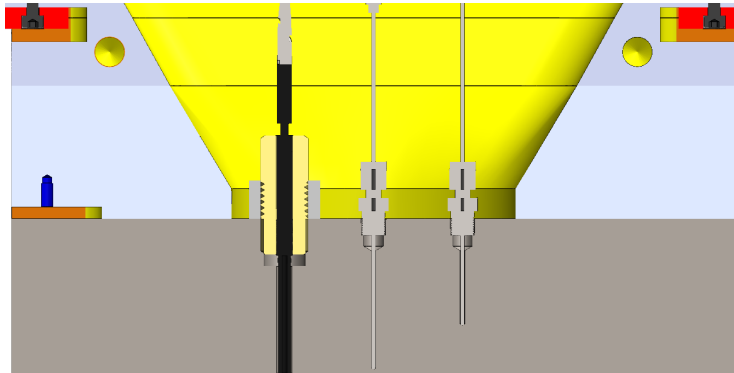
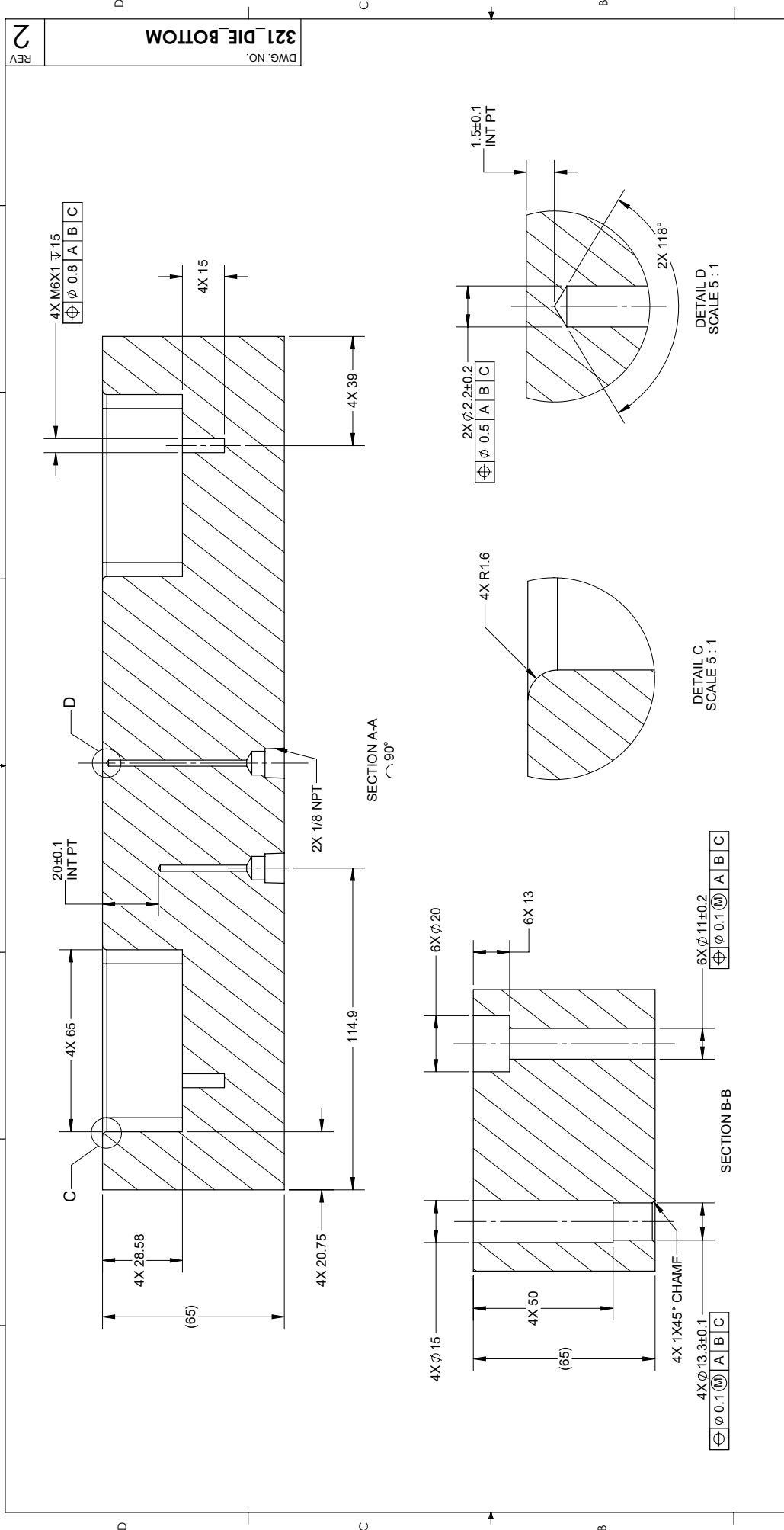


Figure A.10: Section view of upper die showing mounting of IR thermometer tip.

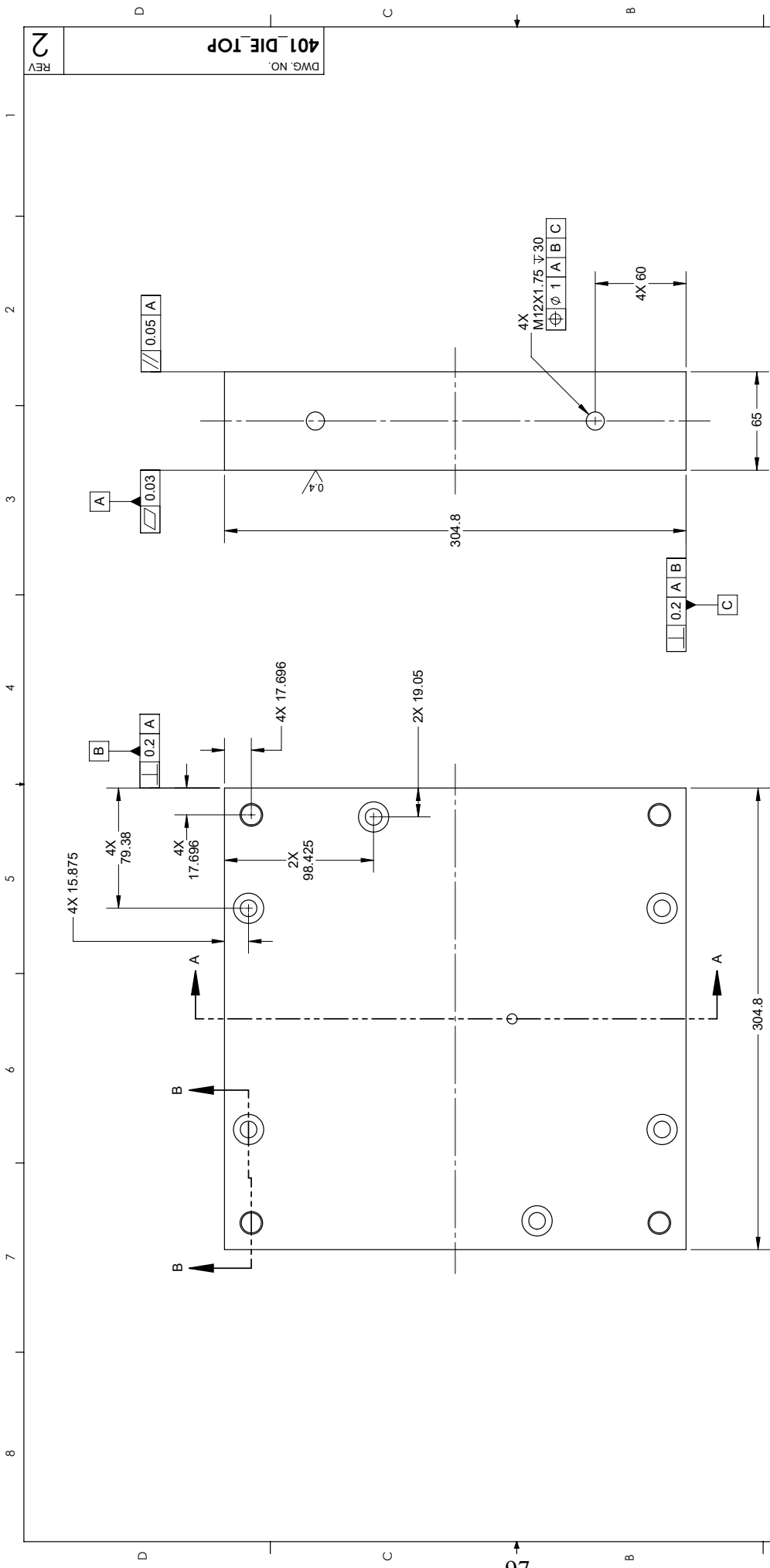
[76] standard for geometric dimensioning and tolerancing (GD&T), which unambiguously specify the nominal dimensions of features (e.g., size and location) along with their allowable variation with respect to a set of datum features. The engineering drawings are included in the following pages.



UNLESS OTHERWISE SPECIFIED GD&T PER ASME Y14.5-2009 NONTOLERANCED DIMENSIONS ARE BASIC NONTOLERANCED GEOMETRIES PER CAD MODEL	DIMENSIONAL UNIT: MILLIMETER	N/A = NOT APPLICABLE	CHAMFERS	1±0.1 X 45°±2°
			FILLETS	R1.6±0.1
GENERAL TOLERANCE	0.4 A B C	BREAK SHARP	R0.03±0.01	OR 0.25±0.1 X 45°±2°
TOLERANCE AND MATERIAL		SHARP	N/A	
TYPE OF 4140 SPECIFIED		THREADED FEATURES	EXTERNAL THREADS AT Ø/MAJOR	
RELEASED			INTERNAL THREADS AT Ø/MINOR	
DATE				
Y/M/D				
DESCRIPTION				

DWG NO.	321_DIE_BOTTOM
REV	2

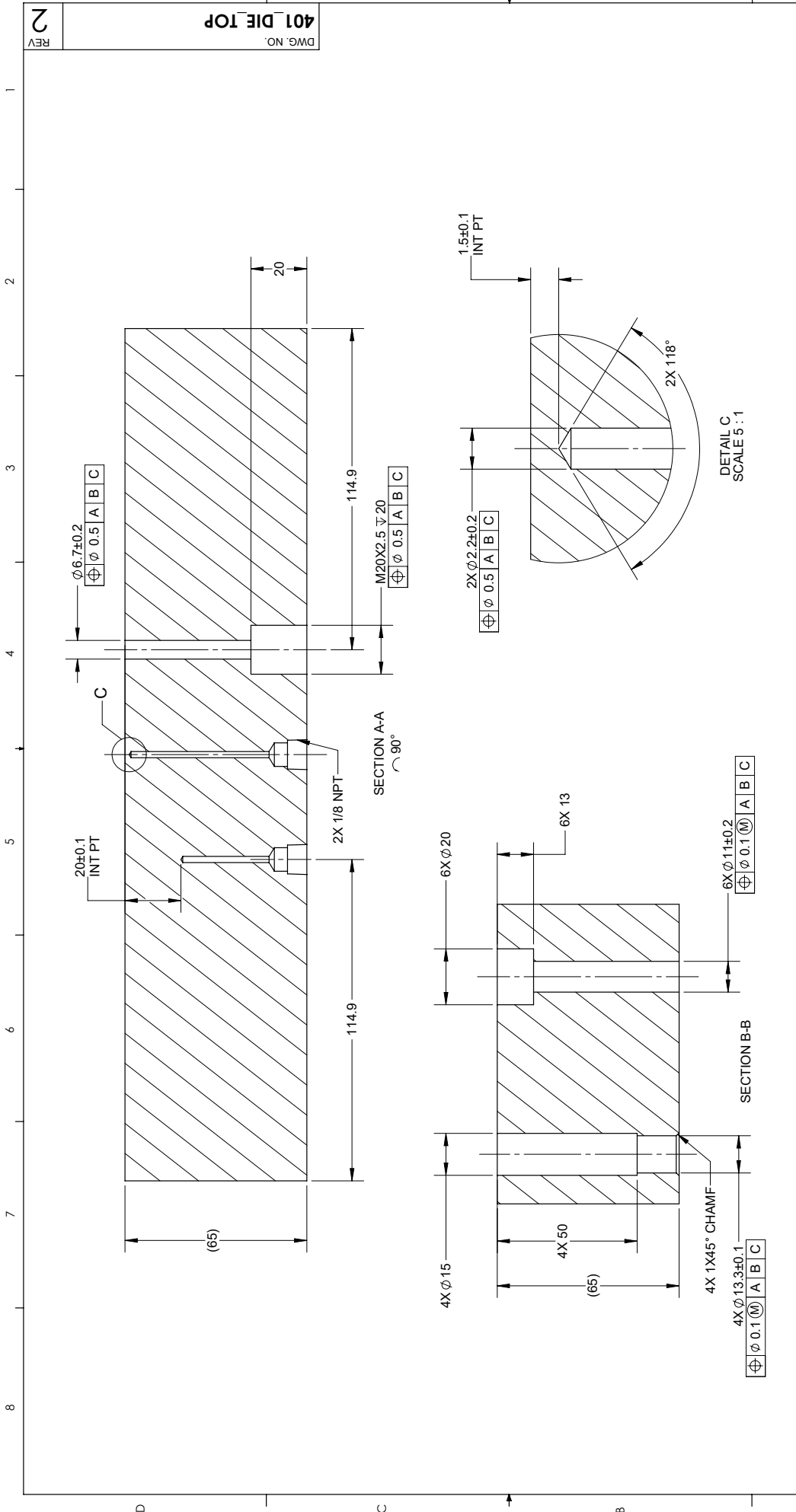
UNIVERSITY	Waterloo Laboratory for Inverse Analysis & Thermal Sciences
of WATERLOO	
TITLE:	BOTTOM DIE
	FLAT HOT FORMING DIE QUENCHING
SIZE	DWG. NO. 321_DIE_BOTTOM
REV	2
DO NOT SCALE DRAWING	SCALE: 3:4
WEIGHT: N/A	SHEET 2 OF 2



DWG NO. 401_DIE_TOP
REV 2

UNIVERSITY OF WATERLOO Waterloo Laboratory for Inverse Analysis & Thermal Sciences		UNIVERSITY OF WATERLOO Waterloo Laboratory for Inverse Analysis & Thermal Sciences	
TITLE: TOP DIE		TITLE: TOP DIE	
MATERIAL 4140HT (28-32 HRC)		MATERIAL 4140HT (28-32 HRC)	
FINISH 3.2		FINISH 3.2	
DO NOT SCALE DRAWING		DO NOT SCALE DRAWING	
SCALE: 2:5		SCALE: 2:5	
WEIGHT: N/A		WEIGHT: N/A	
SHEET 1 OF 2		SHEET 1 OF 2	
PROPERTY: THE INFORMATION CONTAINED IN THIS DRAWING IS THE SOLE PROPERTY OF UNIVERSITY OF WATERLOO. ANY REPRODUCTION IN PART OR AS A WHOLE WITHOUT THE WRITTEN PERMISSION OF UNIVERSITY OF WATERLOO IS PROHIBITED.		PROPERTY: THE INFORMATION CONTAINED IN THIS DRAWING IS THE SOLE PROPERTY OF UNIVERSITY OF WATERLOO. ANY REPRODUCTION IN PART OR AS A WHOLE WITHOUT THE WRITTEN PERMISSION OF UNIVERSITY OF WATERLOO IS PROHIBITED.	
DIMENSIONAL UNIT: MILLIMETER		DIMENSIONAL UNIT: MILLIMETER	
N/A = NOT APPLICABLE		N/A = NOT APPLICABLE	
CHAMFERS 1:0.1 X 45° ± 2°		CHAMFERS 1:0.1 X 45° ± 2°	
FILLETS N/A		FILLETS N/A	
BREAK SHARP OR 0.25 ± 0.1 X 45° ± 2°		BREAK SHARP OR 0.25 ± 0.1 X 45° ± 2°	
SHARP N/A		SHARP N/A	
UNLESS OTHERWISE SPECIFIED GD&T PER ASME Y14.5-2009 NONTOLERANCED DIMENSIONS ARE BASIC NONTOLERANCED GEOMETRIES PER CAD MODEL		UNLESS OTHERWISE SPECIFIED GD&T PER ASME Y14.5-2009 NONTOLERANCED DIMENSIONS ARE BASIC NONTOLERANCED GEOMETRIES PER CAD MODEL	
GENERAL TOLERANCE 0.4 A B C		GENERAL TOLERANCE 0.4 A B C	
THREADED FEATURES EXTERNAL THREADS AT Ø MAJOR INTERNAL THREADS AT Ø MINOR		THREADED FEATURES EXTERNAL THREADS AT Ø MAJOR INTERNAL THREADS AT Ø MINOR	
N/A		N/A	
DWG #	CKD #	DWG #	CKD #
2		2	
TOLERANCE AND MATERIAL	A. SINGH	TOLERANCE AND MATERIAL	A. SINGH
OMITTED DIMENSION ADDED	A. SINGH	OMITTED DIMENSION ADDED	A. SINGH
RELEASED	A. SINGH	RELEASED	A. SINGH
DATE	DESCRIPTION	DATE	DESCRIPTION
21/02/25		21/02/12	
21/02/02		21/02/02	

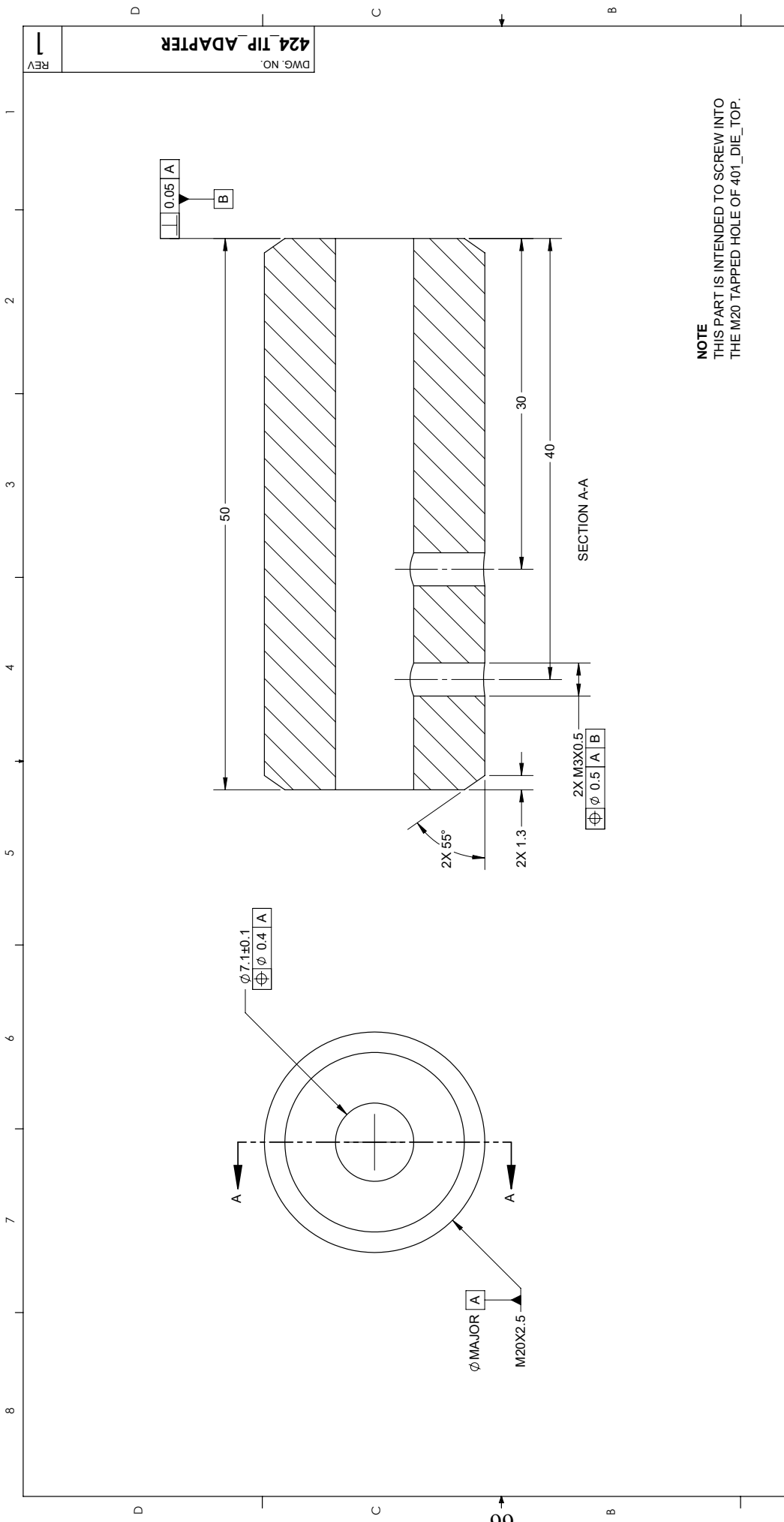
SOLIDWORKS Educational Product. For Instructional Use Only.



UNIVERSITY WATERLOO WATERLOO LABORATORY FOR INVERSE ANALYSIS & THERMAL SCIENCES	PROPRIETARY PROPERTY THE INFORMATION CONTAINED IN THIS DRAWING IS THE SOLE PROPERTY OF UNIVERSITY OF WATERLOO. ANY REPRODUCTION IN PART OR AS A WHOLE WITHOUT THE WRITTEN PERMISSION OF UNIVERSITY OF WATERLOO IS PROHIBITED.		TITLE: TOP DIE FLAT HOT FORMING DIE QUENCHING	
	MATERIAL 4140HT (28-32 HRC)		SIZE B	DWG. NO. 401_DIE_TOP
	FINISH 3.2		SCALE: 3:4 WEIGHT: N/A	
DIMENSIONAL UNIT: MILLIMETER N/A = NOT APPLICABLE		CHAMFERS 1±0.1 X 45°±2°		UNLESS OTHERWISE SPECIFIED GD&T PER ASME Y14.5-2009 NONTOLERANCED DIMENSIONS ARE BASIC NONTOLERANCED GEOMETRIES PER CAD MODEL GENERAL TOLERANCE 0.4 A B C THREADED FEATURES N/A EXTERNAL THREADS AT ØMAJOR INTERNAL THREADS AT ØMINOR
DIMENSIONAL UNIT: MILLIMETER N/A = NOT APPLICABLE		FILLETS N/A BREAK SHARP OR 0.25±0.1 X 45°±2°		
DIMENSIONAL UNIT: MILLIMETER N/A = NOT APPLICABLE		SHARP N/A		
2 21/02/25 TOLERANCE AND MATERIAL	DWN # CKD # DWN # CKD #	A. SINGH A. SINGH	2 21/02/25 TOLERANCE AND MATERIAL	
1 21/02/12 OMITTED DIMENSION ADDED	DWN # CKD # DWN # CKD #	A. SINGH A. SINGH	1 21/02/12 OMITTED DIMENSION ADDED	
0 21/02/02 RELEASED	DWN # CKD # DWN # CKD #	A. SINGH A. SINGH	0 21/02/02 RELEASED	
REV DATE Y/M/D	DESCRIPTION		DO NOT SCALE DRAWING SCALE: 3:4 WEIGHT: N/A	
SOLIDWORKS Educational Product. For Instructional Use Only.			SHEET 2 OF 2	

DWG NO. 401_DIE_TOP

REV 2



NOTE
THIS PART IS INTENDED TO SCREW INTO
THE M20 TAPPED HOLE OF 401_DIE_TOP.

UNIVERSITY of WATERLOO		Waterloo Laboratory for Inverse Analysis & Thermal Sciences	
TITLE: TIP ADAPTER			
UNLESS OTHERWISE SPECIFIED GD&T PER ASME Y14.5-2009 NONTOLERANCED DIMENSIONS ARE BASIC NONTOLERANCED GEOMETRIES PER CAD MODEL		DIMENSIONAL UNIT: MILLIMETER N/A = NOT APPLICABLE CHAMFERS: 1.3±0.1 X 55°±2° FILLETS: N/A BREAK SHARP: R0.03±0.01 OR 0.25±0.1 X 45°±2° SHARP: N/A	
GENERAL TOLERANCE 0.4 A B		MATERIAL 4140 ANNEALED	
THREADED FEATURES EXTERNAL THREADS AT ØMAJOR INTERNAL THREADS AT ØMINOR N/A		FINISH 3.2	
DO NOT SCALE DRAWING		DO NOT SCALE DRAWING	
SCALE: 3:1		SCALE: 3:1	
WEIGHT: N/A		WEIGHT: N/A	
SHEET 1 OF 1		SHEET 1 OF 1	

REV	DATE	DESCRIPTION
1	21/02/25	MATERIAL UPDATED
0	21/02/12	RELEASED

SOLIDWORKS Educational Product. For Instructional Use Only.

Appendix B

Derivation and Verification of Experimental Analyses

B.1 Deriving the Volterra Integral Equation of the First-Kind

The time-resolved surface heat flux entering the die, $q_d''(t)$, was found by deconvolving the Volterra integral equation of the first-kind using an inverse heat conduction algorithm. Deriving this equation starts with the transient, one-dimensional heat conduction equation for a semi-infinite solid

$$\frac{\partial^2 T}{\partial z^2} = \frac{1}{\alpha_d} \frac{\partial T}{\partial t} \quad (\text{B.1})$$

where T is the temperature, z is the coordinate direction normal to the quenching surface, α_d is the thermal diffusivity of the die material, and t is the time. If the die is initially at a uniform temperature of T_i , and a constant heat flux of q_d'' is suddenly imposed on the die surface, then the solution to Eq. (B.1) that determines the die temperature $T_D(t)$ is

$$T_D(t) - T_i = \frac{2q_d''}{k_d} \sqrt{\frac{\alpha_d t}{\pi}} \exp\left(\frac{-D^2}{4\alpha_d t}\right) - \frac{q_d'' D}{k_d} \operatorname{erfc}\left(\frac{D}{2\sqrt{\alpha_d t}}\right) \quad (\text{B.2})$$

where D is the depth from the quenching surface, and k_d is the thermal conductivity of the die material. Eq. (B.2) can be rewritten in terms of the sensitivity (ϕ) of the measured temperature to the imposed heat flux

$$T_D(t) - T_i = q_d'' \cdot \phi(t) \quad (\text{B.3})$$

$$\phi(t) = \frac{2}{k_d} \sqrt{\frac{\alpha_d t}{\pi}} \exp\left(\frac{-D^2}{4\alpha_d t}\right) - \frac{D}{k_d} \operatorname{erfc}\left(\frac{D}{2\sqrt{\alpha_d t}}\right) \quad (\text{B.4})$$

Since the surface heat flux is expected to evolve over time, it is modelled as the superposition of unit step functions. If q''_{d1} is the heat flux between the time interval t_0 and t_1 , q''_{d2} is the heat flux between the subsequent time interval t_1 and t_2 , and so on, then Eq. (B.3) is rewritten as

$$T_D(t) - T_i = \sum_{j=1}^n q''_{dj} \cdot \{\phi(t - t_{j-1}) - \phi(t - t_j)\} \quad (\text{B.5})$$

where n is the total number of time steps. Eq. (B.5) can be written using a relative time scale instead of an absolute time scale. The relative time scale is defined as

$$\tau_j^* = t - t_j \quad (\text{B.6})$$

$$\Delta\tau_j^* = t_j - t_{j-1} \quad (\text{B.7})$$

Substituting Eqs. (B.6) and (B.7) into Eq. (B.5),

$$T_D(t) - T_i = \sum_{j=1}^n q''_{dj} \cdot \frac{\phi(\tau_j^* + \Delta\tau_j^*) - \phi(\tau_j^*)}{\Delta\tau_j^*} \Delta\tau_j^* \quad (\text{B.8})$$

By letting $\Delta\tau_j^* \rightarrow 0$,

$$\lim_{\Delta\tau \rightarrow 0} \frac{\phi(\tau_j^* + \Delta\tau_j^*) - \phi(\tau_j^*)}{\Delta\tau_j^*} = \frac{d\phi}{d\tau_j^*} \quad (\text{B.9})$$

Combining Eqs. (B.8) and (B.9),

$$T_D(t) - T_i = \int_0^t q''_d(t^*) \cdot \frac{d\phi}{dt}(t - t^*) dt^* \quad (\text{B.10})$$

which is the Volterra integral equation of the first-kind that governs the inverse heat conduction analysis for inferring the die surface heat flux.

B.2 Verifying Inverse Heat Conduction Analysis on the Die

The inverse heat conduction analysis was verified using a nonlinear, transient, three-dimensional finite element (FE) model of the experiment. In the FE model, the domain is

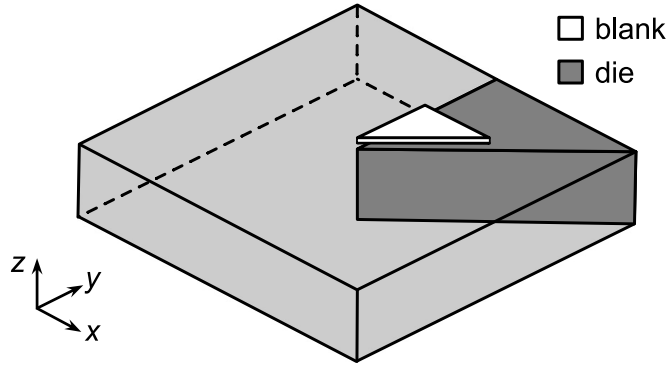


Figure B.1: FE domain of blank and die in contact with each other.

a one-eighth half-space of the blank and die as shown in Figure B.1. The thermophysical properties of the blank [17] and die [30] are that of 22MnB5 and AISI 4140 tool steel, with initial temperatures of 800°C and 22°C, respectively. The contact surface pair between the blank and die was modelled with a constant interfacial heat transfer coefficient (HTC) of 5 kW/(m²K). All remaining surfaces were modelled as adiabatic.

The temperature 1.5 mm below the die surface predicted by the FE model is shown in Figure B.2. To simulate measurement noise, the temperature at each time step was contaminated with random numbers sampled from an unbiased Gaussian distribution having a standard deviation of 2°C. The simulated data, also shown in Figure B.2, was used as the input for the inverse heat conduction algorithm.

The inverse heat conduction algorithm uses the contaminated subsurface die temperature to infer the surface heat flux. Noise amplification in the inferred heat flux is regularized via Beck’s future time step method. In addition to the surface heat flux, solving for HTC requires the interfacial temperatures of the blank and die. The inverse algorithm uses the blank surface temperature directly from the FE analysis, while the die surface temperature is obtained from solving the forward heat conduction problem of the semi-infinite die using the inferred surface heat flux as a boundary condition (i.e., solving for T_D from Eq. (B.10), where $D = 0$ m). Using three future time steps for regularization, the estimated HTC history from the inverse algorithm is plotted in Figure B.3a, along with the FE model input of 5 kW/(m²K). The strong agreement verifies the inverse heat conduction analysis and validates the one-dimensional, semi-infinite modelling of the die that was used to construct the algorithm. The recovered die surface temperature also closely matches the FE modelled values, as shown in Figure B.3b. The latter comparison verifies the forward, well-posed heat conduction solution used to calculate the die surface temperature.

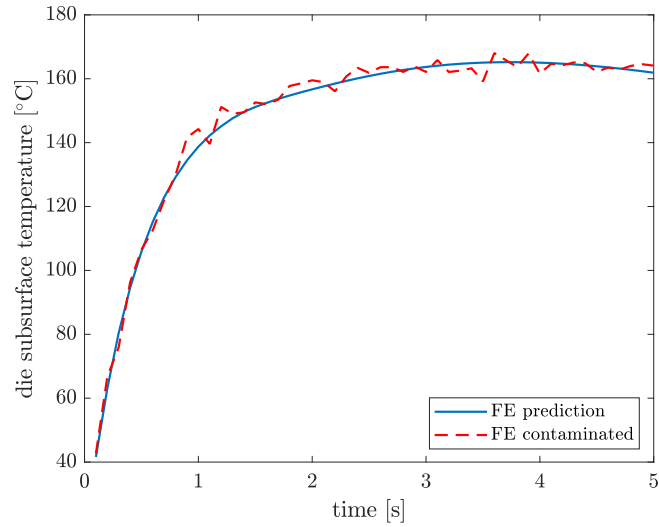


Figure B.2: Die subsurface temperature ($D = 1.5$ mm below quenching surface) predicted by FE analysis, in addition to the contaminated dataset.

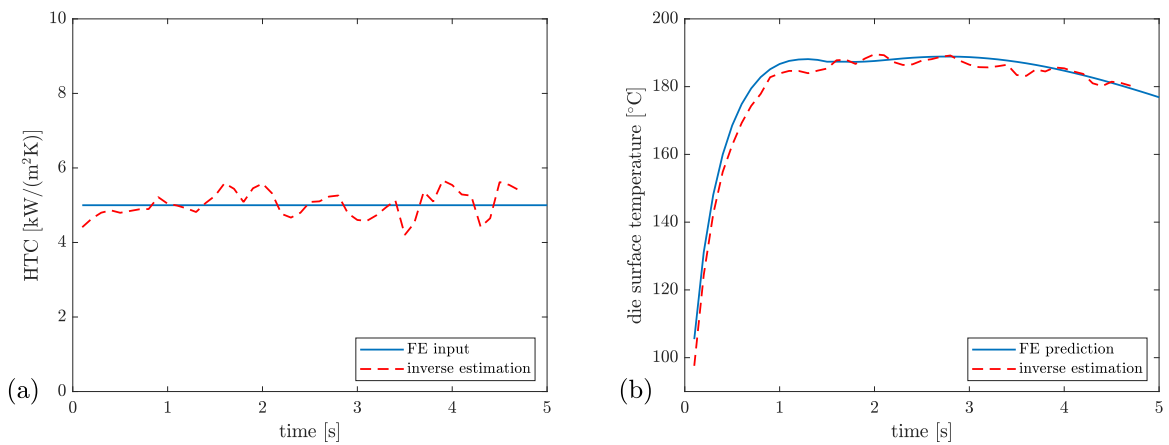


Figure B.3: Comparison between FE and inverse heat conduction analysis of (a) HTC and (b) die surface temperature.

B.3 Deriving Heat Flux Equation for a Thermally Lumped Blank

The time-resolved surface heat flux leaving the blank was calculated from an energy balance analysis. The heat flux at the upper and lower surfaces were assumed to be equivalent, making the analysis symmetric about the midplane. Since the rate of energy leaving the blank, \dot{E}_{out} , must equal the rate of change of energy stored within the blank, \dot{E}_{st} , the heat flux leaving one surface of the blank with an area of A can be written as

$$q_b''(t) = \frac{\dot{E}_{\text{out}}}{A} = -\frac{\dot{E}_{\text{st}}}{A} \quad (\text{B.11})$$

Since \dot{E}_{st} is the sum of the rate of change of sensible energy, \dot{E}_{sens} , and rate of change of latent heat released, \dot{E}_{latent} ,

$$q_b''(t) = -\frac{\dot{E}_{\text{sens}} + \dot{E}_{\text{latent}}}{A} \quad (\text{B.12})$$

The specific heat capacity of the blank, c_b , is defined in terms of the specific internal energy, u_{sens} , as

$$c_b(T) = \frac{\partial u_{\text{sens}}}{\partial T} = \frac{\partial u_{\text{sens}}}{\partial t} \frac{\partial t}{\partial T} \quad (\text{B.13})$$

Accounting for the mass, Eq. (B.13) becomes

$$\rho_b V c_b(T) = \frac{\partial U_{\text{sens}}}{\partial t} \frac{\partial t}{\partial T} = \dot{E}_{\text{sens}} \frac{\partial t}{\partial T} \quad (\text{B.14})$$

where ρ_b and V are the density and half-volume of the blank, and U_{sens} is its total internal energy. Rearranging Eq. (B.14),

$$\dot{E}_{\text{sens}} = \rho_b V c_b(T) \frac{\partial T}{\partial t} \quad (\text{B.15})$$

Prior to martensite formation (i.e., $T > M_s = 400^\circ\text{C}$), $\dot{E}_{\text{latent}} = 0$ W, and therefore Eq. (B.12), combined with Eq. (B.15) leads to

$$q_b''(t) = -\frac{\rho_b V c_b(T)}{A} \frac{\partial T}{\partial t} = -\rho_b L_b c_b(T) \frac{\partial T}{\partial t} \quad (\text{B.16})$$

where L_b is the half-thickness of the blank (i.e., $V/A = L_b$). During martensite formation (i.e., $T \leq M_s = 400^\circ\text{C}$),

$$\dot{E}_{\text{latent}} = \frac{\partial}{\partial t}(\rho_b V \Delta h_m f_m) = \rho_b V \Delta h_m \frac{\partial f_m}{\partial t} \quad (\text{B.17})$$

where Δh_m is the latent heat release of complete austenite-to-martensite transformation, and f_m is the martensite phase fraction. Therefore, Eq. (B.12) combined with Eqs. (B.15) and (B.17) leads to

$$q_b''(t) = -\frac{1}{A} \left(\rho_b V c_b(T) \frac{\partial T}{\partial t} + \rho_b V \Delta h_m \frac{\partial f_m}{\partial t} \right) \quad (\text{B.18})$$

$$q_b''(t) = -\rho_b L_b \left(c_b(T) \frac{\partial T}{\partial t} + \Delta h_m \frac{\partial f_m}{\partial T} \frac{\partial T}{\partial t} \right) \quad (\text{B.19})$$

$$q_b''(t) = -\rho_b L_b \left(c_b(T) + \Delta h_m \frac{\partial f_m}{\partial T} \right) \frac{\partial T}{\partial t} \quad (\text{B.20})$$

Combining Eqs. (B.16) and (B.20), the energy balance equation for calculating the surface heat flux of a thermally lumped blank is

$$q_b''(t) = \begin{cases} -\rho_b L_b c_b(T) \frac{\partial T}{\partial t} & \text{if } T > M_s \\ -\rho_b L_b \left(c_b(T) + \Delta h_m \frac{\partial f_m}{\partial T} \right) \frac{\partial T}{\partial t} & \text{if } T \leq M_s \end{cases} \quad (\text{B.21})$$

B.4 Verifying Energy Balance Analysis on the Blank

The energy balance analysis performed on the blank to calculate the heat flux leaving it was verified using a nonlinear, transient, one-dimensional FE model, in which the blank was modelled as a cube with side lengths of 0.825 mm (same dimension as the half-thickness of the blank). In the FE model, a constant heat flux of 0.5 MW/m² was set to leave one surface of the blank, while the opposing surface representing the blank's symmetry plane was modelled as adiabatic. The four remaining surfaces were also modelled as adiabatic to enforce one-dimensional heat transfer. The thermophysical properties of the blank [17] are that of 22MnB5, and the initial temperature was set to 800°C. The average temperature history of the blank predicted by the FE model is shown in Figure B.4.

The average temperature history predicted by the FE model in Figure B.4 was used as an input in the energy balance analysis (i.e., Eq. (B.21)) to estimate the surface heat flux leaving the blank. The resulting heat flux is shown in Figure B.5, along with the constant FE model input of 0.5 MW/m². Noise was briefly observed in the energy balance estimate at the 2.9-s mark, the same moment the martensite formation starts at $M_s = 400^\circ\text{C}$ as shown in Figure B.4. The noise stems from the assumption that the blank is thermally

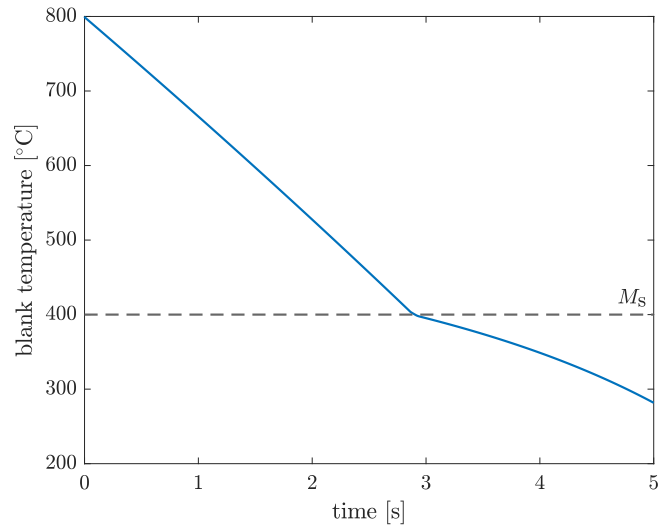


Figure B.4: Average blank temperature predicted by the FE model when the surface heat flux is a constant value of 0.5 MW/m^2 .

lumped, which incorrectly assumes the onset of martensite formation occurs all at once across the thickness of the blank. Outside the 2.9-s mark, good agreement was observed between the energy balance estimate and FE model input, verifying Eq. (B.21) and its numerical implementation for estimating the heat flux leaving the blank from discrete temperature measurements.

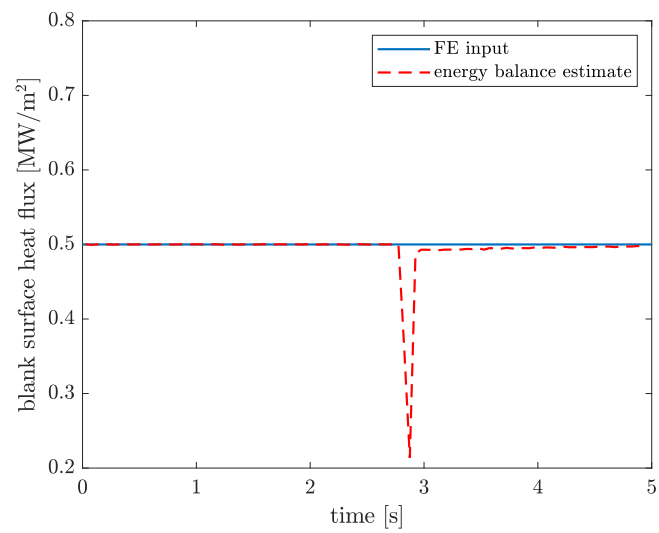


Figure B.5: Comparison between FE input and energy balance estimate (Eq. (B.21)) of heat flux leaving one surface of the blank.

Appendix C

Verification of HTC Model

The HTC model described in Chapter 4 is comprised of a heat transfer and mechanical submodel. The MATLAB functions computing these submodels were verified by comparing their outputs against the results predicted by ANSYS Mechanical.

C.1 Verification of heat transfer submodel

The heat transfer submodel was verified using a transient thermal FE model. Perfect thermal contact was employed at the 22MnB5-intermetallic and intermetallic-die interfaces for the comparison (i.e., asperity heights were unified), and the interfacial pressure was set to zero. The maximum blank temperature histories predicted by the present and FE models in Figure C.1 show good agreement. A slight discrepancy emerges at the one-second mark when martensite formation begins because the spatial and time derivatives of the temperature dependent properties were accounted for in the nonlinear FE model but were assumed to be zero in the present model.

C.2 Verification of mechanical submodel

The mechanical submodel was verified using a transient mechanical FE model. The two elements in Figure C.2a were uniaxially compressed by a rigid die applying a 3.2 N force that increased over a one second period. Plastic behavior of the elements is that of 22MnB5

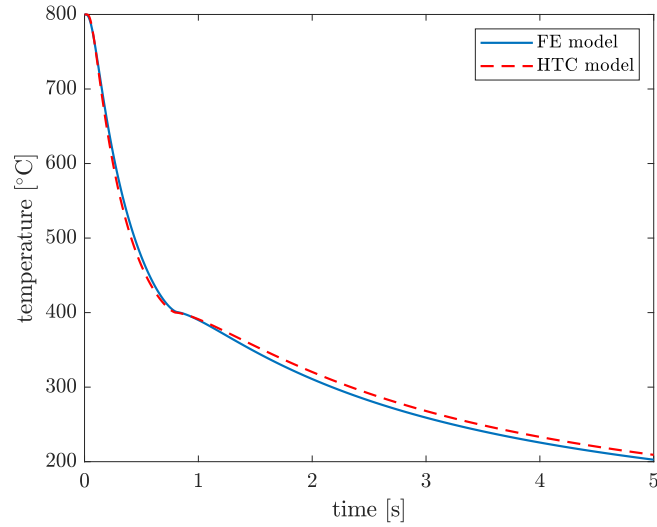


Figure C.1: Comparison of maximum blank temperature predicted by the present and FE model for perfect contact.

at a strain rate of 0.1 s^{-1} and temperature of 650°C . As seen in Figure C.2b, the deformation histories predicted by the present and FE models are in excellent agreement. Both models predict a momentary pause in deformation starting at the 0.25-s mark due to the added strength supplied by the initially shorter element. Once the compressive stress within the shorter element exceeds its flow stress at the 0.4-s mark, both elements deform synchronously from that point onward.

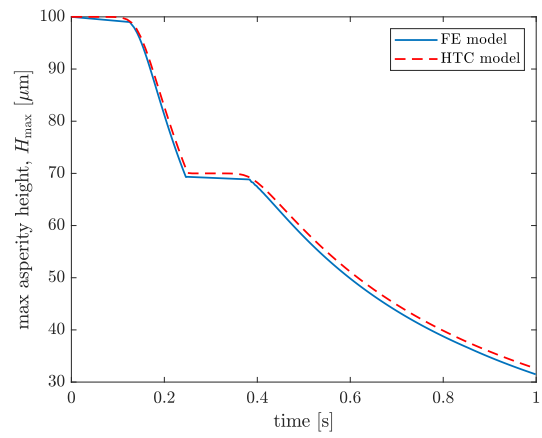
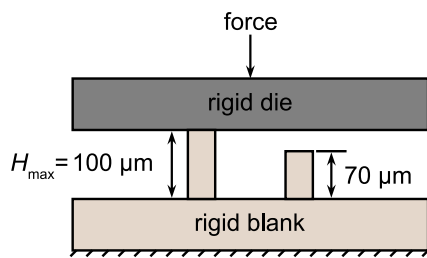


Figure C.2: (a) Initial condition of mechanical verification problem, and (b) comparison of predicted deformation history from present and FE model.